



University of
BRISTOL

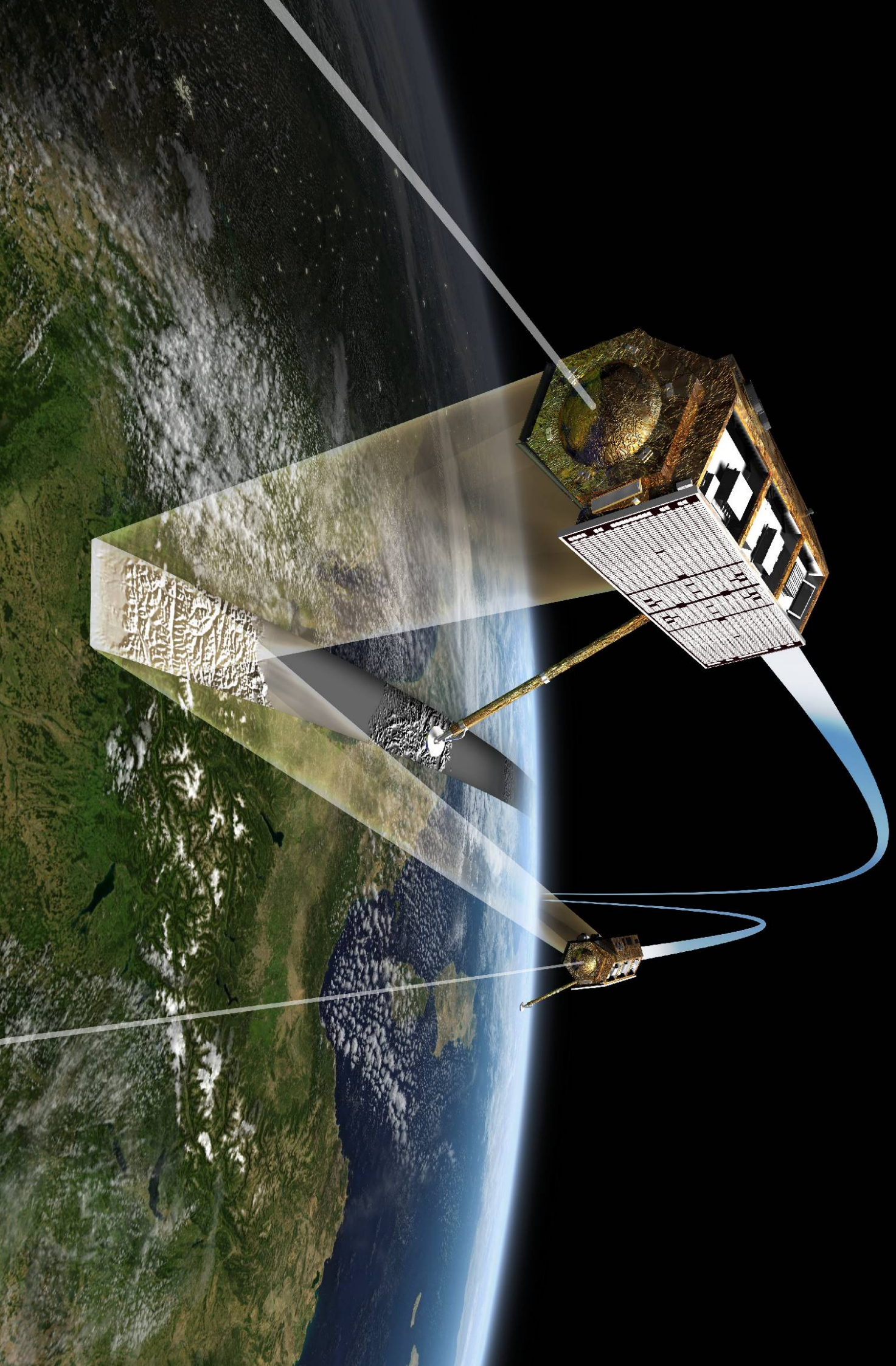
**Statistical Modelling
of
Sea Surface Wind Generated Waves**

Samuel James Taylor

May 2021

**Final year project thesis submitted in support of the degree of
Master of Engineering in Electrical & Electronic Engineering**

**Department of Electrical & Electronic Engineering
University of Bristol**



Samuel James Taylor

Statistical Modelling of Sea Surface Wind Generated Waves

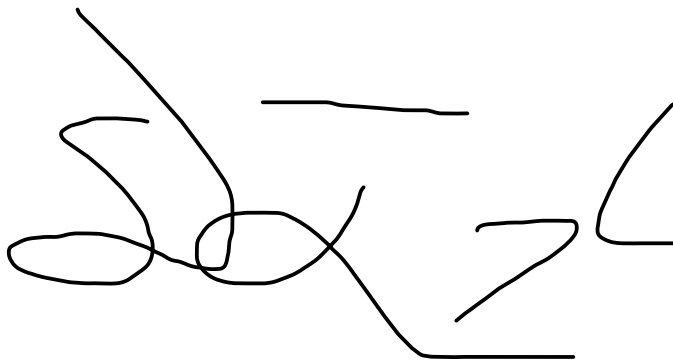
Declaration and Disclaimer

Unless otherwise acknowledged, the content of this thesis is the original work of the author. None of the work in this thesis has been submitted by the author in support of an application for another degree or qualification at this or any other university or institute of learning.

The views in this document are those of the author and do not in any way represent those of the University.

The author confirms that the printed copy and electronic version of this thesis are identical.

Signed:

A handwritten signature in black ink, appearing to read "Samuel James Taylor". The signature is fluid and cursive, with a large loop on the left and a more structured end on the right.

Samuel James Taylor

Dated: 9 May 2021

Abstract

Synthetic Aperture Radar (SAR) is a special form of radar imagery utilizing a moving platform and to achieve a higher spatial resolution.

Given their relatively high resolution and wide area of coverage, SAR imaging systems are well-suited to observe the various oceanic features. SAR images require the use of special techniques for analysis by conventional operations and software due to the nature of SAR images involving multipath radar signals. Special integration techniques which incorporate sea wave information and simulations are used to enable the detection of ships, fishing vessels and other vessels of interest. For these tools to be effective, better statistical models of wind and wave behaviour need to be developed.

The goal of this thesis is to investigate the statistical models which best represent wind generated sea waves within SAR images and to perform iterative testing with the AssenSAR Research Group to assess and improve the accuracy of their simulator's ability to generate realistic wave patterns. The AssenSAR simulator's ultimate goal is to be able to detect ship generated Kelvin wake patterns within SAR images but without an effective model of the wind generated sea waves and how these waves interact with ship wakes, the ship wake detection algorithms will not be statistically accurate.

From the initial investigation, K distribution was found to be the best statistical model for representing the peak portion of the data, up to the tail portion of the data. Beyond this point K distribution was prone to errors. Across the tail of the data, lognormal distribution consistently achieved the best results. These results suggest that a combination of the K and Lognormal distributions will achieve the best outcomes when generating simulations.

Over the course of this investigation, significant improvement was made through three iterations of simulations as lessons learned were applied and adjustments were made to parameters of the simulator. The data model that produced the best results consistently throughout the tests utilized Normalized Radar Cross Section (NRCS), which was clearly better than velocity bunching model. These improvements can easily be seen through the decrease in the values of Euclidean distance of the best case of each of the iterative steps.

From the initial simulations through multiple iterations performed throughout this research the AssenSAR simulator is improving the quality of its results, producing simulations with increasing levels of accuracy. Though some further testing will be needed before the final release, the testing performed in support of this project has been useful in the further development of the software which is expected to be ready and available from the AssenSAR Research Group by 2022.

Contents

Declaration and Disclaimer	ii
Abstract.....	iii
Contents.....	iv
1. Introduction	1
1.1. How SAR functions.....	1
1.2. TerraSAR-X specifications	3
1.3. Bragg scattering	3
1.4. Data Available	4
1.5. Applications of SAR imagery	5
1.5.1. Reasons for SAR imagery	5
1.5.2. SAR image interpretation.....	6
1.6. Statistical modelling.....	6
1.6.1. Gamma distribution [14].....	6
1.6.2. K distribution [18][21][22]	7
1.6.3. Weibull distribution [15].....	7
1.6.4. Rayleigh distribution [16][17]	7
1.6.5. Lognormal distribution [19]	7
1.6.6. Nakagami distribution [20]	7
2. Data Processing.....	8
2.1. Data Set Information.....	8
2.2. Prepossessing.....	9
2.3. Denoising	12
2.4. Processing of Subset Images.....	15
2.5. Concerns over some images	19
3. Dataset Statistical Analysis	20
3.1. Usage of statistical models	20
3.2. Statistical modelling of real images	25
3.2.1. Strait of Gibraltar – GEC SE subset 1.....	25
3.2.2. Strait of Gibraltar – GEC SE subset 2.....	25

3.2.3.	Gulf of Mexico, USA – subset 1	26
3.2.4.	Gulf of Mexico, USA – subset 2	26
3.2.5.	Bay of Plenty, New Zealand – subset 1	27
3.2.6.	Bay of Plenty, New Zealand – subset 2	27
3.2.7.	Barcelona, Spain – dataset 1 subset 1	28
3.2.8.	Barcelona, Spain – dataset 1 subset 2	28
3.2.9.	Barcelona, Spain – dataset 5 subset 1	29
3.2.10.	Barcelona, Spain – dataset 5 subset 2	29
3.2.11.	Barcelona, Spain – dataset 8 subset 1	30
3.2.12.	Barcelona, Spain – dataset 8 subset 2	30
3.2.13.	Barcelona, Spain – dataset 12 subset 1	31
3.2.14.	Barcelona, Spain – dataset 12 subset 2	31
3.2.15.	Barcelona, Spain – dataset 17 subset 1	32
3.2.16.	Barcelona, Spain – dataset 17 subset 2	32
3.2.17.	Barcelona, Spain – dataset 20 subset 1	33
3.2.18.	Barcelona, Spain – dataset 20 subset 2	33
3.2.19.	Barcelona, Spain – dataset 21 subset 1	34
3.2.20.	Barcelona, Spain – dataset 21 subset 2	34
3.2.21.	Barcelona, Spain – dataset 24 subset 1	35
3.2.22.	Barcelona, Spain – dataset 24 subset 2	35
3.3.	Analysis of results from normal images.....	36
4.	Simulations.....	37
4.1.	Data models for simulation.....	37
4.2.	1 st iteration test results for simulated 400 x 400 images.....	39
4.2.1.	Simulated I image.....	39
4.2.2.	Simulated S image.....	40
4.2.3.	Simulated SR image.....	41
4.2.4.	Simulated S0 image.....	42
4.3.	Review of results of 1 st iteration simulated images.....	43
4.4.	2 nd iteration test results for simulated 800 x 800 images.....	44

4.4.1.	Simulated I image.....	44
4.4.2.	Simulated I2 image.....	45
4.4.3.	Simulated S image.....	46
4.4.4.	Simulated S2 image.....	47
4.5.	Review of results of 2 nd iteration simulated images.....	47
5.	3 rd iteration simulations.....	49
5.1.	3 rd iteration simulations datasets	49
5.2.	3 rd iteration simulated image test results.....	51
5.2.1.	Simulated S image –Strait of Gibraltar – subset 2	51
5.2.2.	Simulated S0 image –Strait of Gibraltar – subset 2	52
5.2.3.	Simulated S image –New Zealand – subset 2	53
5.2.4.	Simulated S0 image –New Zealand – subset 2	54
5.2.5.	Simulated S image – Barcelona – dataset 1 subset 2.....	55
5.2.6.	Simulated S0 image – Barcelona – dataset 1 subset 2	56
5.2.7.	Simulated S image – Barcelona – dataset 12 subset 1.....	57
5.2.8.	Simulated S0 image – Barcelona – dataset 12 subset 1	58
5.2.9.	Simulated S image – Barcelona – dataset 20 subset 1.....	59
5.2.10.	Simulated S0 image – Barcelona – dataset 20 subset 1	60
5.3.	Review of results of 3 rd iteration simulated images	60
5.4.	Items out of scope	63
6.	Conclusion.....	63
	Appendix 1 - Bibliography	65
	Appendix 2 - Access to files utilised.....	69
	Appendix 3 - Programs utilised	70

1. Introduction

Remote imaging of the ocean environment offers new tools which support a range of applications including environmental issues like monitoring oil spills and law enforcement issues like tracking illegal vessels. For these tools to be effective, better statistical models of wind and wave behaviour need to be developed. Given the size of the ocean environment, the varying weather conditions and the need for both daytime and night-time monitoring, remote imaging solutions need to have a high enough resolution covering as wide an area as possible. Within the past two decades spaceborne remote sensing techniques have become the most cost-effective tools for ocean observation and surveillance.

Conventional imaging systems use the spectral reflectance of visible sunlight of the specific object of observation, this is different from the backscattering response of the same object's surface to illumination caused by microwave energy, often referred to as "backscattering signal" [1]. Synthetic Aperture Radar (SAR) is a remote sensing technique that utilises an active micro-sensor on-board a spaceborne asset, either a satellite or an aircraft, illuminating the target in question with a focused directional beam of energy. This technique generates a unique scattering effect depending on the orientation of the observed objects [2].

Given their relatively high resolution and wide area of coverage, SAR imaging systems are well-suited to observe the various oceanic features [3]. SAR images provide two-dimensional information with respect to the field in question. A high-resolution SAR image relies on a smooth variation in the phase history over a data gathering interval. Taking advantage of the long-range propagation characteristics of radar signals and computational capabilities of modern digital electronic systems, SAR images are able to achieve relatively higher resolutions [4]. SAR images require the use of special techniques for analysis by conventional operations and software due to the nature of SAR images involving multipath radar signals. Special integration techniques which incorporate sea wave information and simulations are used to enable the detection of ships, fishing vessels and other vessels of interest. [5,6]

1.1. *How SAR functions*

Towards a basic understanding of how SAR imagery works, the following is a detailed explanation given by Stimson [7].

A SAR system consists of an "end-to-end" system that includes key building blocks. Conventional radar building blocks such as antenna, transmitter, receiver, and a data collection system which provides a coherent doppler phase histories as well as an advancing processor able to produce an image from the phase histories.

A SAR system is considered "end to end" as it requires all the processes said above to be considered when changing one aspect, as even one change can alter the final product's quality. Some

of the elements that must be considered are the moving platform, typically a satellite, the transmitter signal, the propagation effects, complex target interactions (including motion), the received signal, data recovery and on-board or ground-based signal processing. A visual of this process can be seen in figure 1. SAR images are able achieve a high azimuth resolution (the direction of travel of the satellite) by restoring and constructing return signals in the “synthesised aperture”. For normal radar system to survey or image a swath of 30 km to 50 km wide, (the area used in most of data sets to be examined in this thesis) the antenna would have to be 47 football fields long [8]. With this relatively high resolution and wide swath area SAR images are supremely useful for the previously stated tasks.

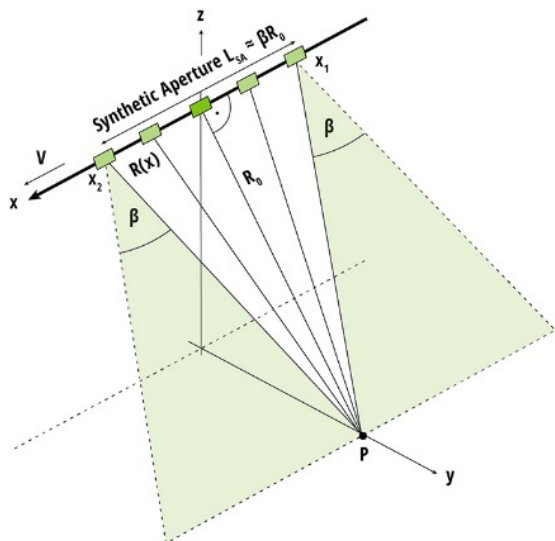


Fig. 1 Geometry of observations used to form the synthetic aperture for target P along track position $x = 0$.
Credit: NASA SAR Handbook.[8]

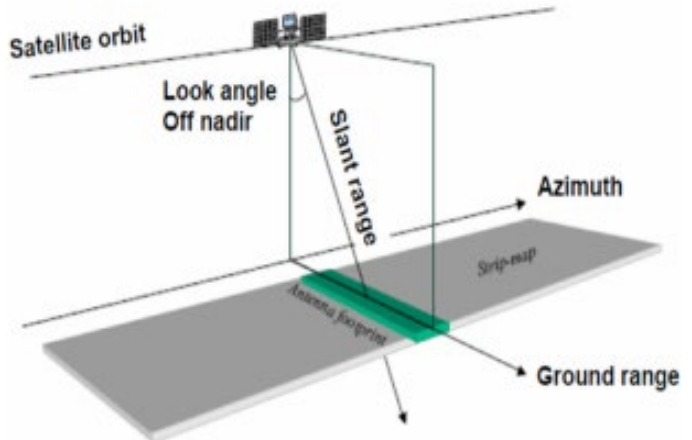


Fig.2 side looking SAR geometry and flightpath [1]

There are few differences from a typical optical imaging solution relative to a SAR imaging framework. A SAR imaging solution will have a radar antenna pointing perpendicular to the flightpath, the azimuth direction, as can be seen in figure 2.

Most SAR satellites operate within a particular region of the micro-spectrum, ranging from 1 mm to 1 m in wavelength. The following specific wavelengths, X band (3 cm), C band (6 cm), S band (10 cm) and L band (24 cm) are commonly associated with SAR images. Each of these specific bands, the ranges of their frequencies and wavelengths along with their related use cases are detailed below in table 1.

Band	Frequency	Wavelength	Typical application
Ka	27-40 GHz	1.1-0.8 cm	Rarely used for SAR (airport surveillance)
K	18-27 GHz	1.7-1.1 cm	rarely used (H ₂ O absorption)
Ku	12-18 GHz	2.4-1.7 cm	rarely used for SAR (satellite altimetry)
X	8-12 GHz	3.8-2.4 cm	High resolution SAR (urban monitoring, ice and snow, little penetration into vegetation cover; fast coherence decay in vegetated areas)
C	4-8 GHz	7.5-3.8 cm	SAR Workhorse (global mapping; change detection; monitoring of areas with low to moderate penetration; higher coherence); ice, ocean maritime navigation
S	2-4 GHz	15-7.5 cm	Little but increasing use for SAR-based Earth observation; agriculture monitoring (NISAR will carry an S-band channel; expands C-band applications to higher vegetation density)
L	1-2 GHz	30-15 cm	Medium resolution SAR (geophysical monitoring; biomass and vegetation mapping; high penetration, InSAR)
P	0.3-1 GHz	100-30 cm	Biomass. First p-band spaceborne SAR will be launched ~2020; vegetation mapping and assessment. Experimental SAR.

Table. 1 typical application usage for differing SAR frequency values [8]

For the purposes of this thesis, statistical analysis will be carried out on SAR imagery from the TerraSAR-X satellite which operates in the X band. The reason the X band is effective for imaging wind generated waves, and for ship detection will become clear through this investigation.

1.2. *TerraSAR-X specifications*

The TerraSAR-X satellite, launched in 2007, is capable of imaging anywhere on the planet as it orbits the Earth from pole to pole at an altitude of 514 km. TerraSAR-X operates on a specific frequency of 9.65 GHz wavelength of 3.11 cm with a resolution of approximately 1 m to 18 m depending on operating mode. The potential swath, the width of area imaged, can range from 5 km to 100 km. The look angle of the satellite ranges from 20 to 55 degrees, as displayed in figure 2.

1.3. *Bragg scattering*

The physics principle of Bragg Scattering causes some unique interactions with electromagnetic pulse generated by the SAR satellite. When the wavelength of the generated signal is close to that of the object it is interacting with, such as a wind generated wave, the electromagnetic pulse will be reflected back to the point of origin. Effects of this can be seen in figure 3 where multiple scenarios are given. In the top left corner, a sea surface that is entirely common, unrealistic but entirely flat. This causes a normal reflection of the signal and therefore no return to be picked up by the radar antenna on this SAR satellite. In the top right the signal generated and the wave have a similar wavelength thus the

signal is reflected back towards the SAR satellite. In the middle left image this shows waves less than the electronic pulse some of the signal is still reflected but at a reduced intensity thus ridding the grey and point. The rest of the images are a variation on choppy waves and variable returned intensity of the signal.

With the TerraSAR-X, operating within the X-band and with a resolution 1 m to -18 m, delivers the best possible results for observing the statistical properties of wind generated waves. The TerraSAR-X imagery is also useful in testing the **AssenSAR** Research Group's SAR simulator which has been designed to create close to reality images with similar statistical distribution.

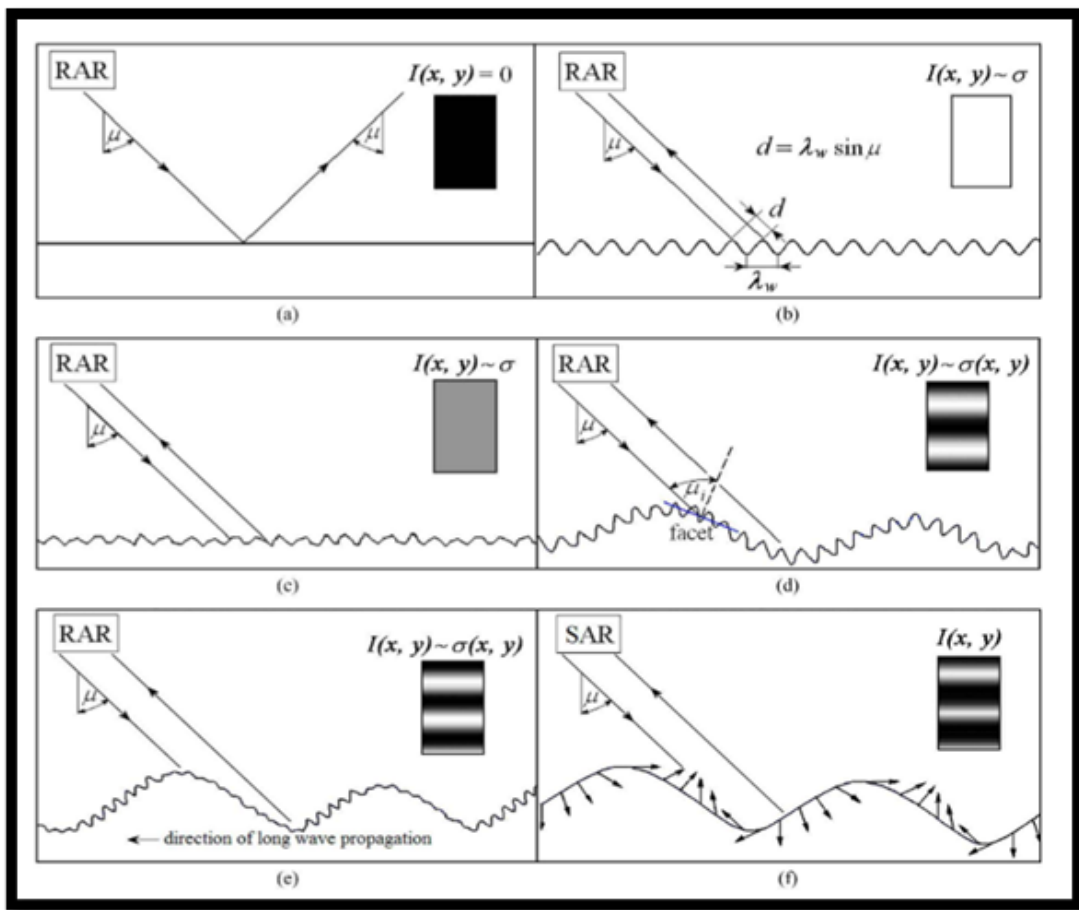


Fig. 3. Sketch of RAR/SAR imaging of illuminating surfaces. The filled rectangles in the upper right corners display schematic gradations of white and black RAR/SAR images. (a) Specular reflection. (b) First-order Bragg scattering. (c) Bragg scattering from an irregular sea surface (d) Tilt modulation with μ as the local incidence angle. (e) Hydrodynamic modulation. (f) Fluid particle orbital velocity modulation (“velocity bunching”). [9]

1.4. Data Available

The European Space Agency provided 12 datasets from the TerraSAR-X satellite for use in this research project. Each dataset had two subsets where the influence of wind on the waves is unaffected by ship traffic. The availability of datasets free of ship traffic was important as the purpose of this thesis is to identify the statistical properties of wind generated waves, for the purpose of validating the wind and

wave properties and assumptions within the AssenSAR simulator. [10] For the simulator's generation of ship wake images to be statistically accurate, the background wind generated waves required more validation. The SAR images utilized in the study can be seen in section 2.1.

For a detailed understanding of the generation of SAR images Chaturvedi's "Study of synthetic aperture radar and automatic identification systems for ship target detection" [11] and Moreira et al "Tutorial on Synthetic Aperture Radar" [12] are both helpful resources. Chaturvedi's work mostly details the effects of Doppler shift caused by the motion of the platform, satellite, or aircraft, on star image generation and the related mathematical formulae [11]. Moreira's paper is a comprehensive history of SAR technology over the past 20 years aptly named editorial and synthetic aperture radar [12].

1.5. Applications of SAR imagery

SAR imagery has many applications for the scientific community as well as law enforcement, Coast Guard, and military use, including vessel monitoring in all weather conditions, as SAR imagery is not degraded by conditions that impact normal radar reflections [13]. SAR imagery is also used in scientific monitoring of ice movements around the sea, due to the large area SAR imagery can cover, generating large quantities of data which can be very useful to scientists. These tools can also be used to detect oil spills and monitor their spread, despite wind and wave action, as the reflective properties of oil are different than that of water. Using SAR imagery to monitor offshore oil rigs provides an extra layer of safety for rig operations. SAR imagery can also be utilized in geological surveys and the classification of earth terrain, using the Doppler shift of the returning signals to determine the size and geological factors of the observed terrain.

1.5.1. Reasons for SAR imagery

SAR imagery is capable of all-weather data collection because of its utilization of the microwave section of the electromagnetic spectrum. SAR can image effectively even when normal optical observation would be obstructed, such as in the midst of heavy clouds or rain. In similar manner, SAR imagery does not rely on the sun's radiation as do like optical, therefore allowing both day and night operations for recording. An added benefit of being in the microwave spectrum, is the image is affected by dielectric properties of water, biomes, or ice. The imagery can be sensitive to rough surfaces, see figure 3 for the effects of Bragg scattering on rough surface of the sea. These are only some of the advantages provided.

On the other hand, disadvantages of this technology include its complex interaction with surface, which can potentially alter how an image looks or make it harder to determine where the signal is coming from, which adds extra complexity in the decoding and processing of SAR images. Being an image reconstructed from returning radar signals, SAR images can fall victim to 'speckle noise' which is caused by either deconstructive or constructive interference of the electromagnetic

signals returning from the observed field. Likewise, radar returns off rough surfaces can result in irregular image recreation.

1.5.2. SAR image interpretation

General rules to follow when interpreting SAR images are as follows:

- a) Regions of calm water and other smooth surfaces appear black, because the incident radar reflects away from the spacecraft. See figure 3 (a), top left.
- b) Surface variations near the size of the radar's wavelength cause strong backscattering. See figure 3 (b), top right.
- c) A rough surface backscatters more strongly See figure 3 (c), middle left.
- d) Stronger wave action will present a white and black striped return image due to the complexities of the sea surface state. See figure 3 (d,e,f).

There are more techniques for interpreting SAR images that are particular to imaging land or buildings which are not needed for the purposes of this thesis, though the reference literature [13] has more examples and uses of the technique.

1.6. Statistical modelling

In the past five years, several scholarly publications have presented statistical models which describe SAR imagery of the sea surface and can be used to categorise the intensity of the SAR images. [22][23][24] The last two papers were presented by the AssenSAR Research Group of Bristol, who are collaborators in this analysis. The goal of the statistical analysis performed for this thesis is to identify a close-fitting statistical model for wind generated sea waves to validate the background modelling of the AssenSAR Research Group's simulator of SAR images. The particular purpose of the simulator is to model ship wakes, and for this modelling to represent a high fidelity of accuracy, the background data for wind generated waves should statistically equivalent to various sea states observed in real SAR images.

The following six statistical models will be utilized in the statistical modeling of the real-world datasets provided by the European Space Agency specifically the TerraSAR X satellite.

1.6.1. Gamma distribution [14]

Gamma distribution is a two-parameter probability distribution, using the shape parameter K and the scale parameter Θ to determine the shape of the probability density function.

The equation for representing a probability density function (PDF) is as follows for random variable input X:

$$X \sim \Gamma(k, \theta) \stackrel{\text{def}}{=} \text{Gamma}(k, \theta)$$

$$f(x; k, \theta) = \frac{x^{k-1} e^{-\frac{x}{\theta}}}{\theta^k \Gamma(k)} \quad (1)$$

For more information on how to obtain parameter estimation of values of K and θ, inspect [14] or other literature in this field.

1.6.2. *K distribution [18][21][22]*

K distribution is a special case of the gamma distribution, utilizing the combination of two gamma distributions with re-parametrization of each of normal form used. Like a gamma distribution, it has both a scale and shape parameter, with an additional Mean distribution factor utilized in its calculation. The PDF of the function equation is below. This formula is a simplified two parameter form of the K-Distribution for random variable X [38]:

$$f_X(x; b, v) = \frac{2b}{\Gamma(v)} \left(\frac{bx}{2} \right)^v K_{v-1}(bx) \quad (2)$$

Where v is the shape parameter and b is the scale factor, with K being the modified Bessel function of second kind.

1.6.3. *Weibull distribution [15]*

The Weibull distribution is a continuous probability distribution with this equation defining the parameters for the PDF for random variable X:

$$f(x; \lambda, k) = \begin{cases} \frac{k}{\lambda} \left(\frac{x}{\lambda} \right)^{k-1} e^{-\left(\frac{x}{\lambda} \right)^k} & x \geq 0, \\ 0 & x < 0 \end{cases} \quad (3)$$

Where $\lambda > 0$ Scale parameter and $k > 0$ is the shape parameter for the distribution

1.6.4. *Rayleigh distribution [16][17]*

The Rayleigh distribution is defined as a PDF function for a random variable X that is greater than 0, with σ being the scale parameter:

$$f(x; \sigma) = \frac{x}{\sigma^2} e^{-x^2/(2\sigma^2)}, \quad x \geq 0 \quad (4)$$

1.6.5. *Lognormal distribution [19]*

Lognormal distribution is a particular case for representing data that is normally distributed within the logarithm in case. The mathematical formula below is the PDF for lognormal where μ is the mean and σ² is the variance:

$$f_X(x) = \frac{1}{x\sigma\sqrt{2\pi}} \exp\left(-\frac{(\ln(x)-\mu)^2}{\sigma^2}\right) \quad (5)$$

1.6.6. *Nakagami distribution [20]*

The Nakagami distribution is a special case of the previously mentioned Gamma distribution, but having different regulations on its shape parameter of $M \geq 1/2$ with the addition of a parameter controlling spread $\Omega > 0$ with this PDF equation:

$$f(x; m, \Omega) = \frac{2m^m}{\Gamma(m)\Omega^m} x^{2m-1} \exp\left(-\frac{m}{\Omega}x^2\right), \forall x \geq 0 \quad (6)$$

All the models listed above were used in the statistical analysis of the SAR images that will follow in the coming pages. This analysis will be performed by code running through MATLAB, as is common in SAR statistical modeling.

2. Data Processing

The following four sets of SAR images were selected for study from the TerraSAR-X satellite archive available from the European Space Agency. These four image sets are the underlying data which will be observed, tested and simulated during this investigation.

2.1. Data Set Information

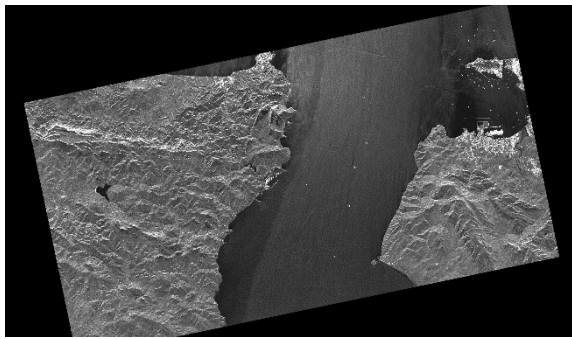


Fig. 4 Strait of Gibraltar - GEC, SE [25]

Satellite: TerraSAR-X

Location: Strait of Gibraltar

Acquisition mode: Strip Map

Antenna Pointing: Right

Orbit: Descending

Date Taken: 12-MAY-2008 06:29:51

Incidence near: 31.791828155517578 deg

Incidence far: 34.62184524536133 deg

Polarisation: HH

Radar frequency: 9650.0 MHz (X-band)

Range sample spacing: 1.25 m

Azimuth sample spacing: 1.25 m

Range samples: 37600 samples

Azimuth samples: 55600 samples

Range distance: 47000 m



Fig. 5 Gulf of Mexico, USA [26]

Satellite: TerraSAR-X

Location: Gulf of Mexico, USA

Acquisition mode: Strip Map

Antenna Pointing: Right

Orbit: Descending

Date Taken: 10-JUL-2010 12:07:25.000000

Incidence near: 19.70811015000925 deg

Incidence far: 23.17932455018235 deg

Polarisation: VV

Radar frequency: 9650.0 MHz (X-band)

Range sample spacing: 3.25 m

Azimuth sample spacing: 3.25 m

Range samples: 9921 samples

Azimuth samples: 17479 samples

Range distance: 332243.25 m

Azimuth distance: 69500 m

Pixel resolution : 1.25 m x 1.25 m

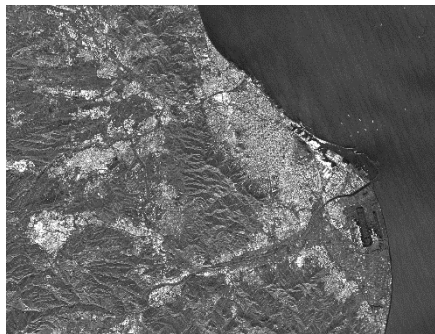


Fig. 6 Barcelona, Spain [27]

Location: Barcelona

Acquisition mode: Strip Map

Antenna Pointing: Right

Orbit: Ascending

Date Taken: (there are 8 separate images)

Incidence near: 33.997894287109375 deg

Incidence far: 36.657615661621094 deg

Polarisation: VV

Radar frequency: 9650.0 MHz

Range sample spacing: 0.909403472071926 m

4 sf (0.9094m)

Azimuth sample spacing: 1.89048629381474 m

4 sf (1.8905m)

Range samples: 20494 samples

Azimuth samples: 31832 samples

Range distance: 18637.24 m

Azimuth distance: 60178.4

Pixel resolution : ~ 0.91 m x 1.89 m

Images used: Dataset 1,5,8,12,17,20,21 & 24

Azimuth distance: 56806.75 m

Pixel resolution : 3.25 m x 3.25 m

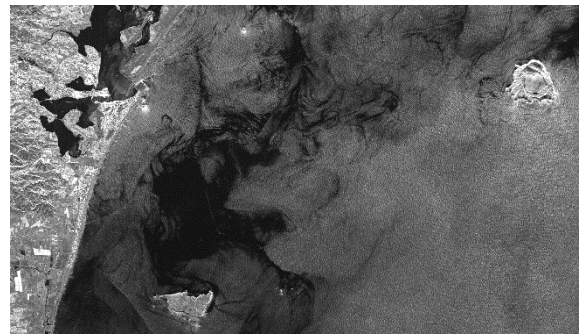


Fig. 7 Bay of Plenty, New Zealand [28]

Location: New Zealand

Acquisition mode: Strip Map

Antenna Pointing: Left

Orbit: Descending

Date Taken: 12-OCT-2011 18:01:15.0000

Incidence near: 22.3542 deg

Incidence far: 25.6463 deg

Polarisation: VV

Radar frequency: 9650.0 MHz

Range sample spacing: 3.00 m

Azimuth sample spacing: 3.00 m

Range samples: 10855 samples

Azimuth samples: 18854 samples

Range distance: 32565.0 m

Azimuth distance: 56562 m

Pixel resolution : 3.00 m x 3.00 m

2.2. Prepossessing

Before the SAR data's raw points can be used for statistical analysis, the image itself must be calibrated, using the Sentinel Application Platform (SNAP) software tool, originally developed in support of the Central One satellite, one of the original satellites used in SAR imagery. The software is

maintained and updated by the European Space Agency (ESA).[29] SNAP was used to perform the initial calibration of the datasets shown above.

When importing datasets into the SNAP application, it is extremely important to select the target satellite used in the creation of the image, as there are varying frequency bands used on differing satellites resulting in varying time for signal returns which will cause errors to occur when calibrating the data if incorrect parameters are used.

The size of images used in the statistical comparison was 800 x 800 pixels, representing a subset of the larger real images. The reason for using this smaller data subset is to allow for a reasonable simulation time. The higher the pixel resolution greater the complexity of the simulation. In order to generate a simulation comparable to the raw SAR images compared, the simulator would need multiple days to produce a simulated image for comparison, hence the decision to perform analysis on the 800 x 800 pixel subset.

After an image is imported into the SNAP tool via the satellite selection import option, the image needs to be calibrated. The setting selected to conduct this routine can be found on the tools bar: Radar -> Radiometric -> Calibrate.

This import and calibration process can take up to one hour per raw SAR image, depending on its resolution and the number of data points per image. For example, the Straits of Gibraltar subset were selected as the resolution is high and the images are particularly well defined.

After the raw SAR image is imported, see figures 8-10, the images are more “speckled” than seen in figure 4. which was an overview of the image and not the SAR image itself. The speckles present are granular in pattern, noise caused by random interference between the coherent returns issued from the scatterers off the earth’s surface, on the scale of a wavelength of the incident radar wave. In general, speckle noise is the grainy salt-and-pepper pattern present in radar imagery [30]. In order to minimize this speckle noise, more treatments to the image must be made before statistical models can be tested on the images.

Figure 9 is the final SNAP calibrated image, combining information from the previous two images. This product can now be extracted from the SNAP application in a GeoTIFF file format which will contain the intensity values of each pixel. This file format is easily accessible by programs like MATLAB and Python for performing numerical analyses.

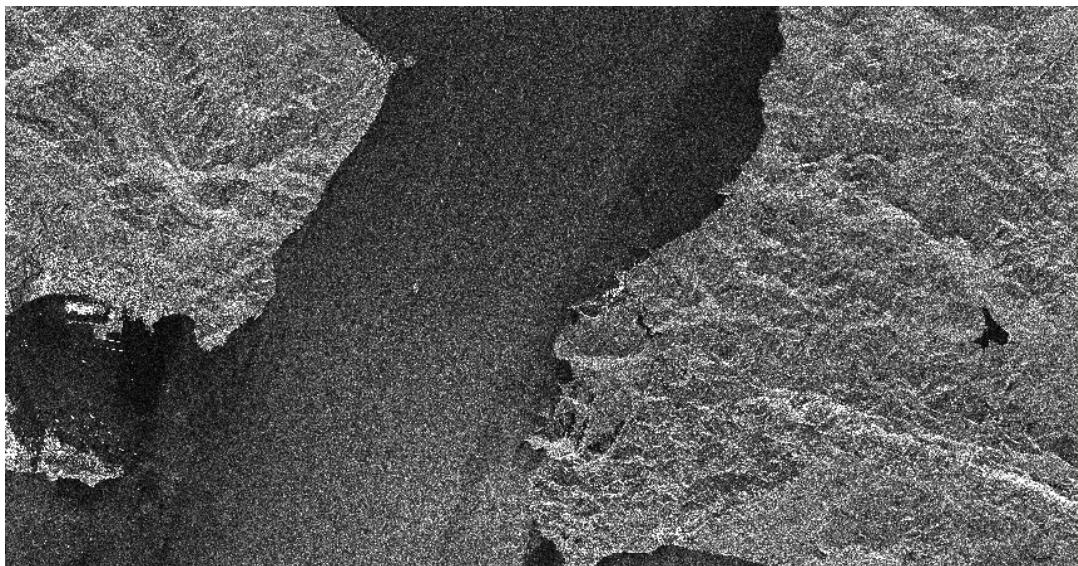


Fig.8 Amplitude HH Straits of Gibraltar (pre calibration)

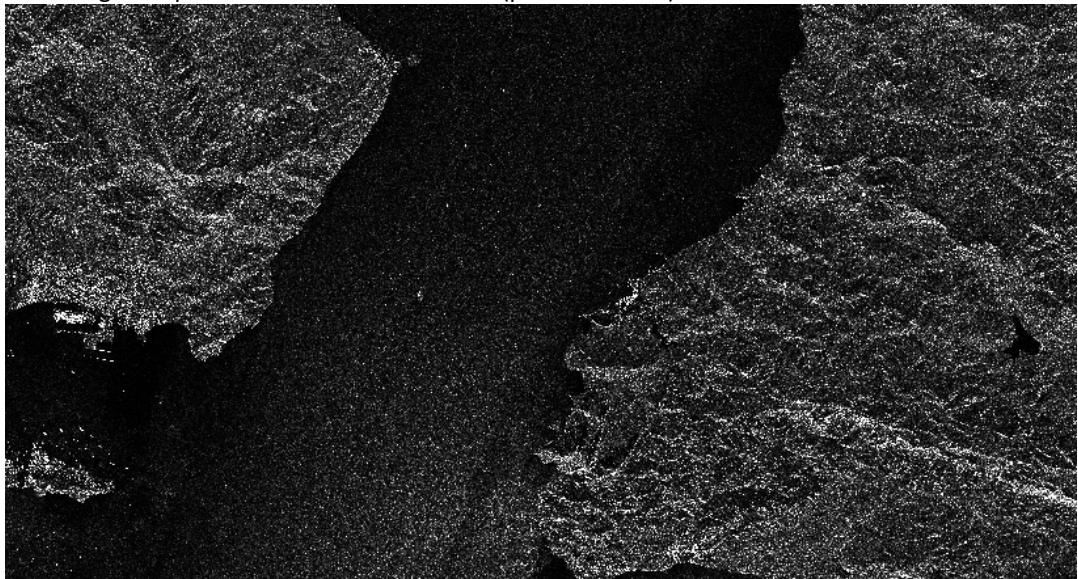


Fig.9 Intensity HH Straits of Gibraltar (pre calibration)

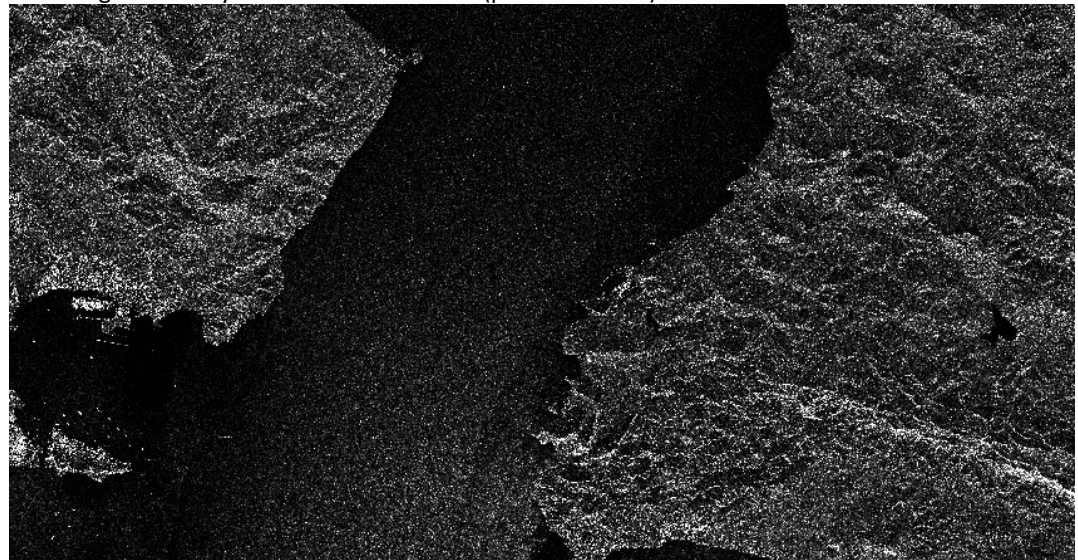


Fig.10 Sigma_0 HH Straits of Gibraltar (post calibration)

From this point, the newly formed GeoTIFF file will need to be denoised. Based on the advice of the AssenSAR group and form [30], a multiplicative denoiser should be used to deal with the speckle noise of the image.

2.3. Denoising

For denoising multiplicatively, the Multi-channel Logarithm with Gaussian (MuLoG) denoiser was utilised [31], a MATLAB program specifically designed for the purpose of denoising SAR imagery. The denoiser has an L parameter which affects the number of looks in the denoising process. A large L value removes fine grain noise, while smaller values of L are used for larger “speckle” noise. To find an appropriate value for the parameter, different L values were tested against each other and ultimately the values for L used in the test images were 2 and 2.7.

```

4 - for i = 1:11
5 - addpathrec('.');
6 - deterministic('on');
7 - load(['TerraSAR_XStripMapStraitOfGibraltar_GEC_SESubSet1']);
8 -
9 - C = TerraSAR_XStripMapStraitOfGibraltar_GEC_SESubSet1;
10 -

```

Fig.10 code extract from the MuLoG denoiser loading files of subset 1

```

17 %% Gaussian noise simulation setting
18 x = C;
19 Ls = [1,2,3,5,7,10,15,20,25,35,50]
20 L = Ls(i); % level of denoising
21 denoiser = @bm3d;
22
23
24
25 %% Run MuLoG with embedded BM3D Gaussian denoiser
26 disp('Run MuLoG with embedded BM3D Gaussian denoiser');
27 tic;
28 h = robustwaitbar(0);
29 xhat = mulog(C, L, denoiser, ...
30 'waitbar', @(p) robustwaitbar(p, h));
31 close(h);

```

Fig.11 code extract from the MuLoG denoiser values used in the test for the denoiser

At the finalization of the iterative tests an L value of 1 was selected with some guidance from AssenSAR and the results of this test can be seen in figure 12.

Samuel James Taylor

Statistical Modelling of Sea Surface Wind Generated Waves

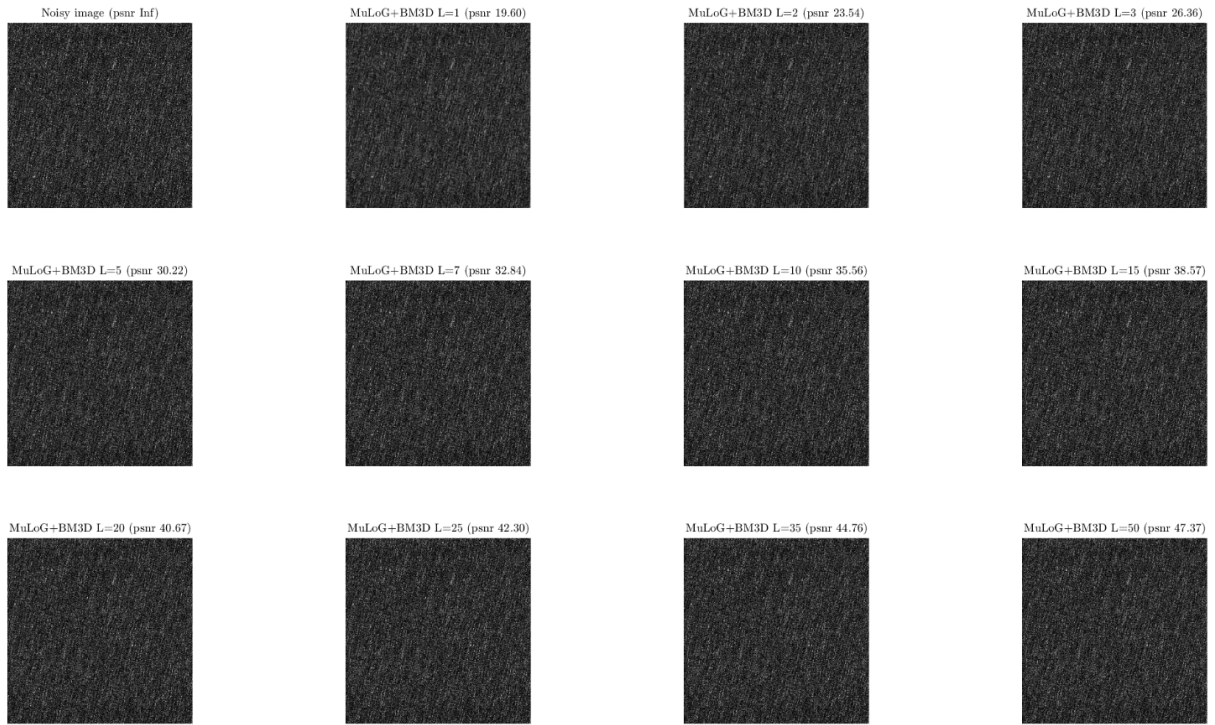


Fig. 12 fully denoised looks with differing values of L

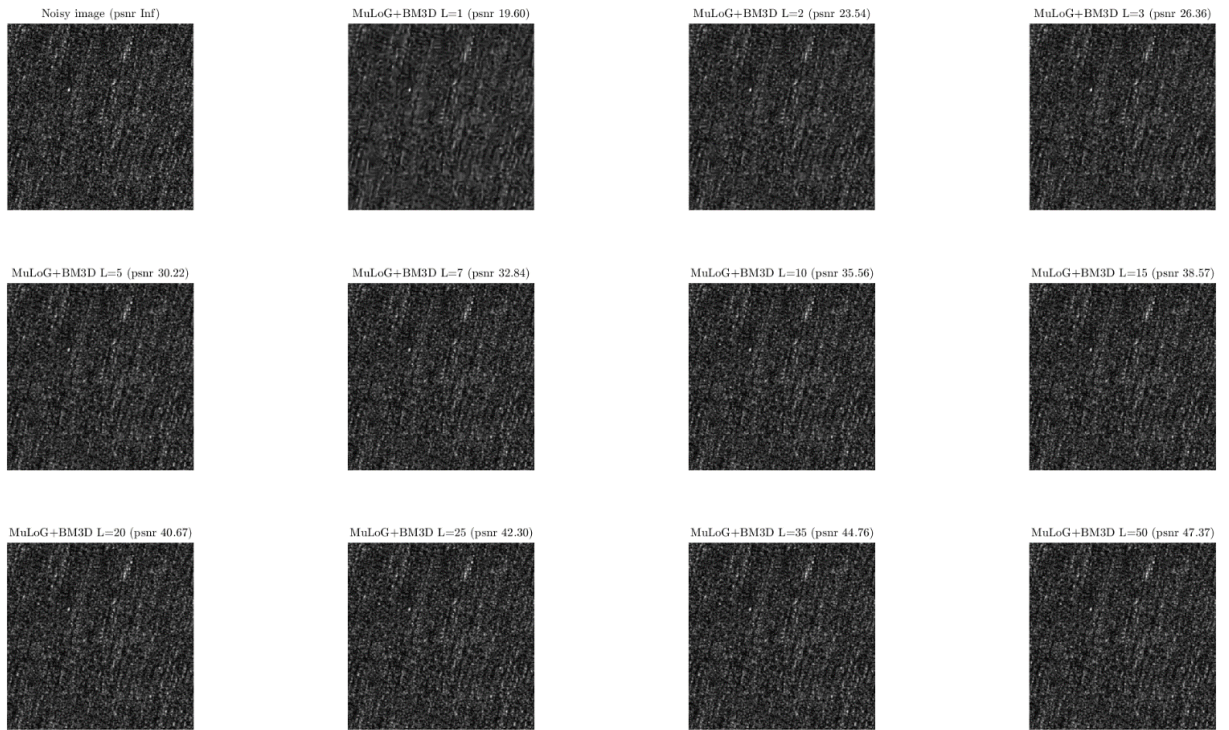
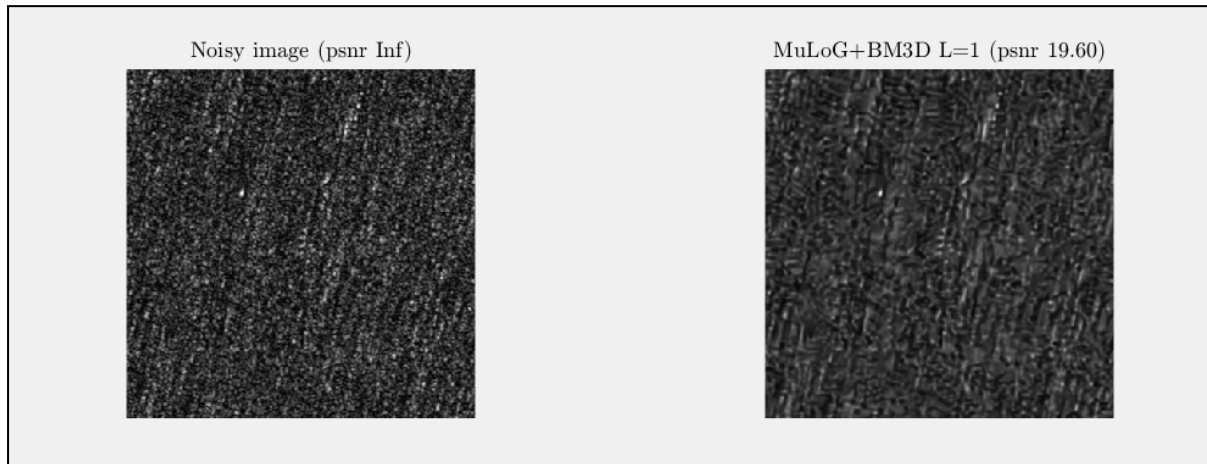


Fig. 13 zoomed denoised looks with differing values of L

Fig. 14 comparison between original image and $L = 1$

The $L = 1$ for the denoiser as can be seen in figures 13-14 which smothered the speckle elements of the image. These tests confirmed the most appropriate value for L .

The later goal of comparing statistical properties of real images to the simulated images drove attempts to remove noise from the images, as the current simulator is not programmed to reproduce the multiplicative noise present in SAR images. As such, steps taken in removing noise from the real images were recorded for later analysis and improvement of the simulator.

```
176 - | noise = C./xhat;
```

Fig.15 extracting noise from the image

'Xhat' is the denoised product of the denoiser and C was the original image in an 800×800 matrix. The (./) is the division element wise for each pixel. This formula enables the extraction of the noise from the image, which, unlike gaussian noise, is generally located around 0, at the center of the bell curve, as displayed in figure 16.

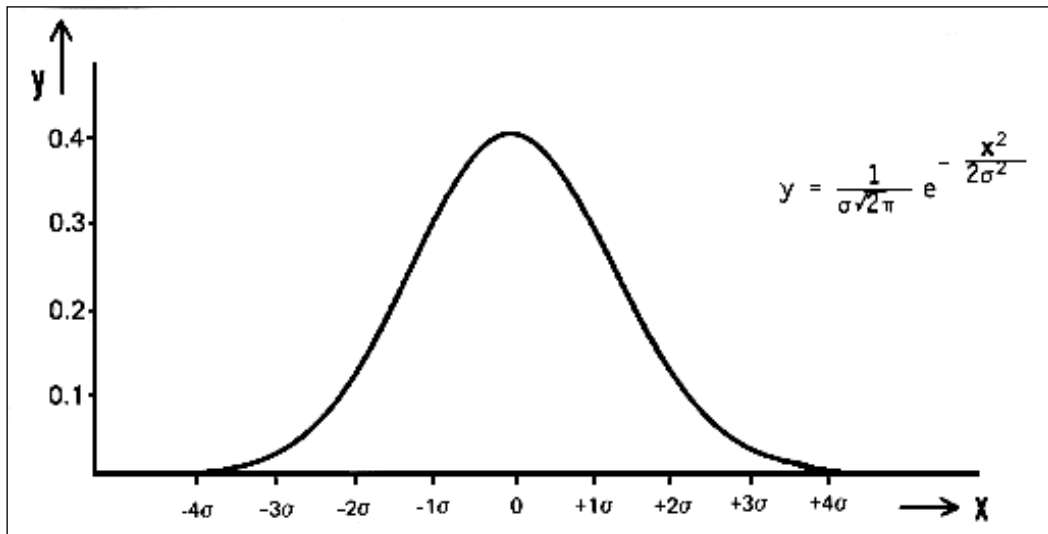


Fig.16 gaussian distribution with baseline of 0 [32]

The multiplicative noise's baseline is around 1, displayed in figure 17, meaning that due to the multiplicative nature, where noise = 1 effectively there is no noise present. Any deviation from 1 will experience increasing elements of noise.

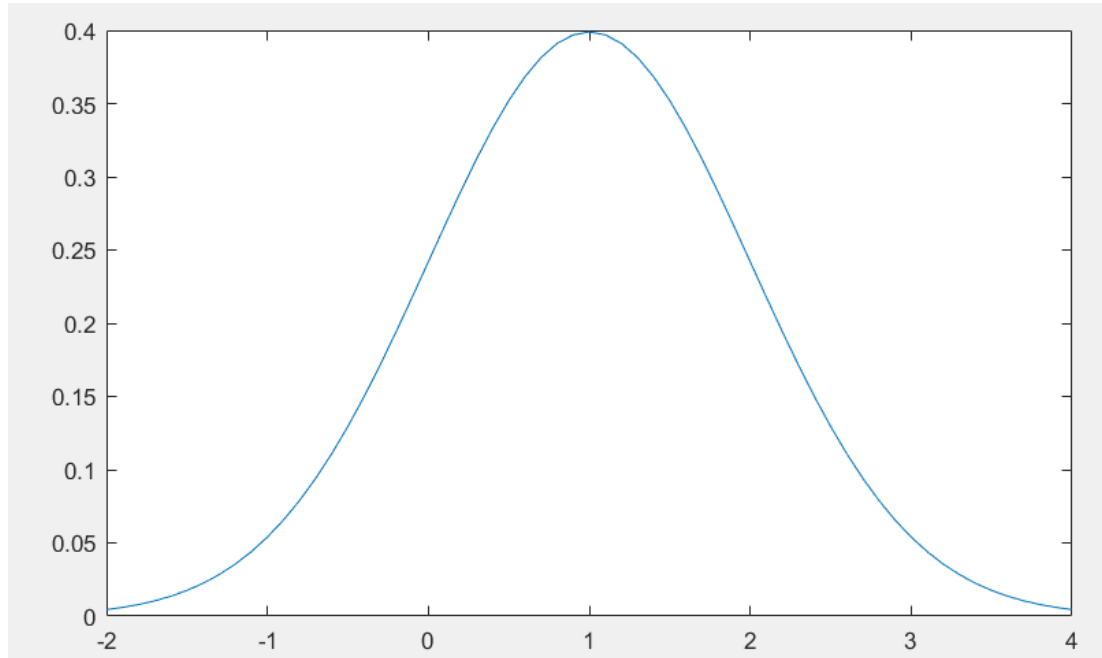


Fig. 17 Gaussian distribution with baseline of 1

2.4. Processing of Subset Images

For each of the four real SAR images, presented as figures 4-7, two subsets were extracted for the analysis of the wind generated waves. Additionally, there are eight images from the Barcelona set that were each taken at separate times. The images from each sample subset of the original real SAR image are detailed below in figures 18 to 39. The extra metadata that is not shown in the section below can be found above in section 2.1. The location of each subset in relation to the original image is listed in X and Y coordinates. The images shown below are in the format pre denoised versions:

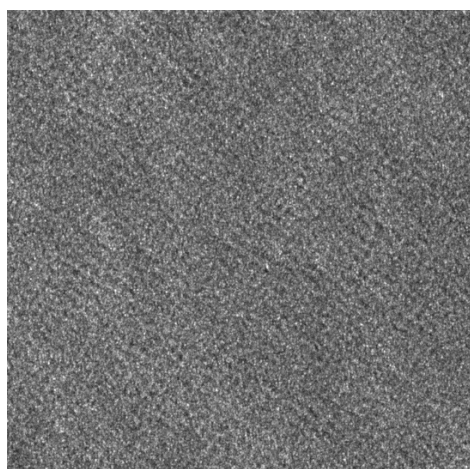


Fig. 18 USA Gulf of Mexico subset 1 location:
X 4,000 - > 48,000 | Y 15,000 -> 15,800 Pixels

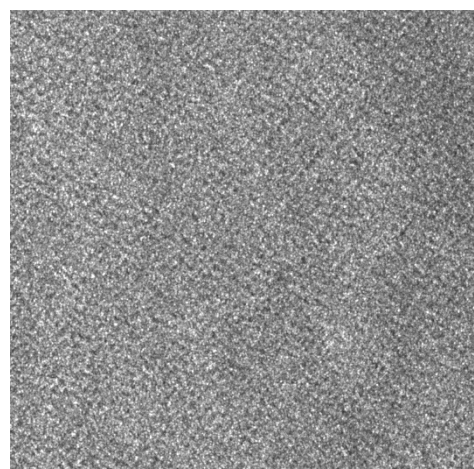


Fig. 19 USA Gulf of Mexico subset 2 location:
X 100 - > 900 | Y 8600 -> 9,400 Pixels

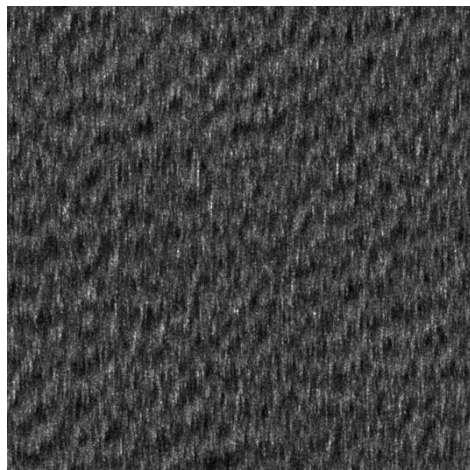


Fig. 20 Bay of Plenty, New Zealand subset 1 location:
X 400 - > 1,200 | Y 400 -> 1,200 Pixels

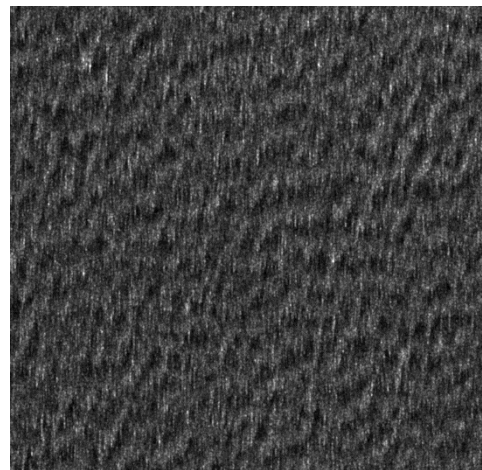


Fig. 21 Bay of Plenty, New Zealand subset 2 location:
X 400 - > 1,200 | Y 400 -> 1,200 Pixels

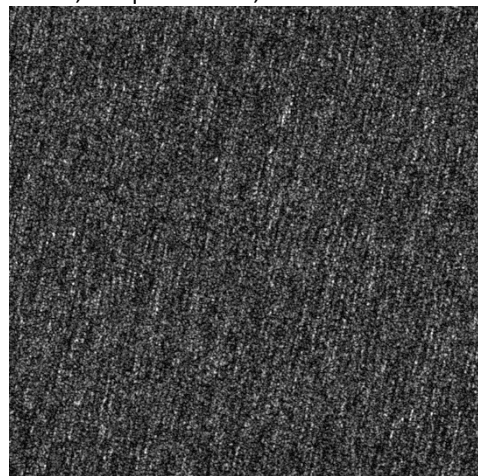


Fig. 22 Strait of Gibraltar - GEC, SE subset 1 location:
X 24,000 - > 24,800 | Y 22,400 -> 23,200 Pixels

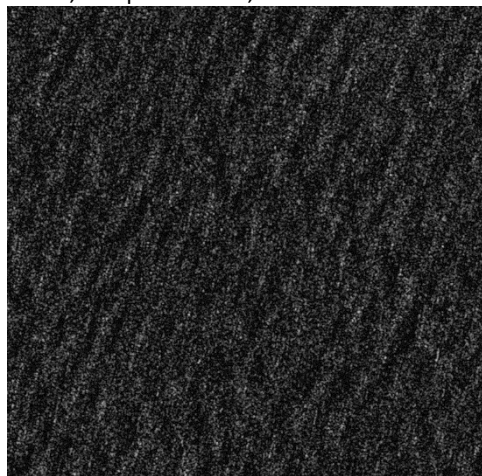


Fig. 23 Strait of Gibraltar - GEC, SE subset 2 location:
X 10,200 - > 11,000 | Y 27,600 -> 28,400 Pixels



Fig. 24 Barcelona dataset 1 subset 1 location:
X 6,300 - > 7,100 | Y 6,300 -> 7,200 Pixels



Fig. 25 Barcelona dataset 1 subset 2 location:
X 16,700 - > 17,500 | Y 5,000 -> 5,800 Pixels



Fig. 26 Barcelona dataset 5 subset 1 location:
X 6,800 - > 7,600 | Y 850 -> 1,650 Pixels



Fig. 27 Barcelona dataset 5 subset 2 location:
X 11,100 - > 11,900 | Y 1,300 -> 2,100 Pixels

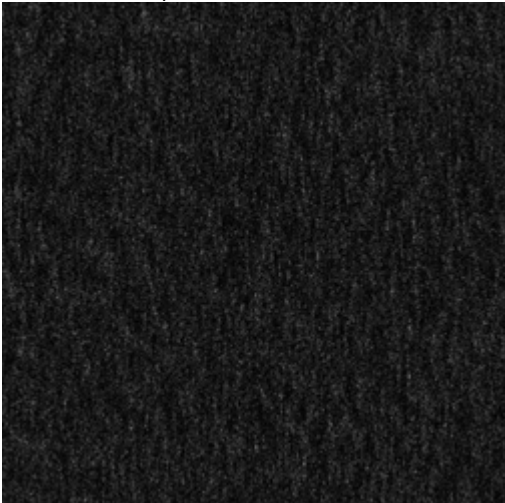


Fig. 28 Barcelona dataset 8 subset 1 location
5,100 - > 5,900 | Y 630 -> 1,430 Pixels



Fig. 29 Barcelona dataset 8 subset 2 location:
X 15,000 - > 15,800 | Y 1,800 -> 2,600 Pixels

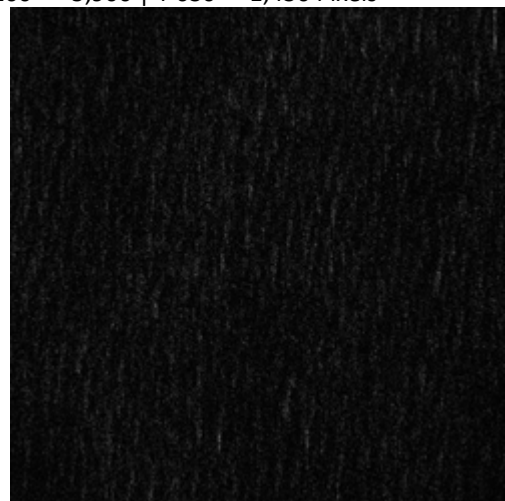


Fig. 30 Barcelona dataset 12 subset 1 location:
X 5,100 - > 5,900 | Y 630 -> 1,430 Pixels



Fig. 31 Barcelona dataset 12 subset 2 location:
X 5,100 - > 5,900 | Y 630 -> 1,430 Pixels



Fig. 32 Barcelona dataset 17 subset 1 location:
X 5,100 - > 5,900 | Y 630 -> 1,430 Pixels

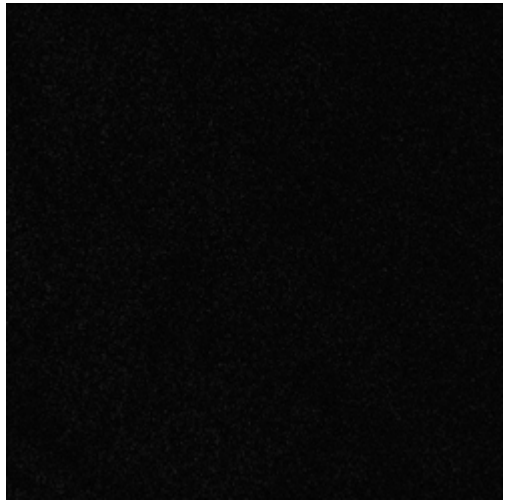


Fig. 33 Barcelona dataset 17 subset 2 location:
X 5,100 - > 5,900 | Y 630 -> 1,430 Pixels



Fig. 34 Barcelona dataset 20 subset 1 location:
X 5,100 - > 5,900 | Y 630 -> 1,430 Pixels



Fig. 35 Barcelona dataset 20 subset 2 location:
X 5,100 - > 5,900 | Y 630 -> 1,430 Pixels

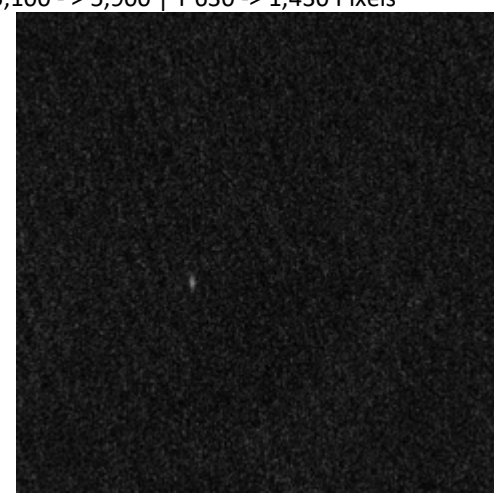


Fig. 36 Barcelona dataset 21 subset 1 location:
X 5,100 - > 5,900 | Y 630 -> 1,430 Pixels

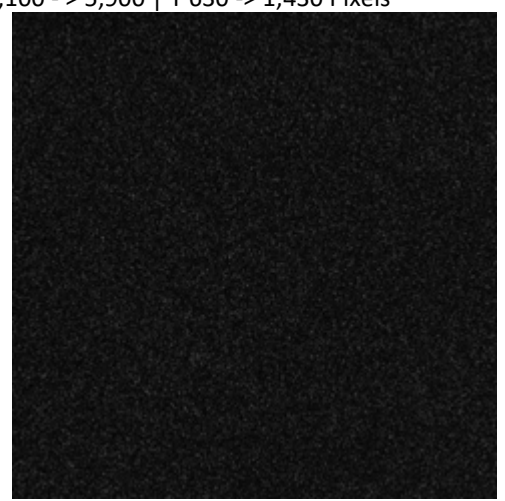


Fig. 37 Barcelona dataset 21 subset 2 location:
X 5,100 - > 5,900 | Y 630 -> 1,430 Pixels



Fig. 38 Barcelona dataset 24 subset 1 location:
X 5,100 -> 5,900 | Y 630 -> 1,430 Pixels

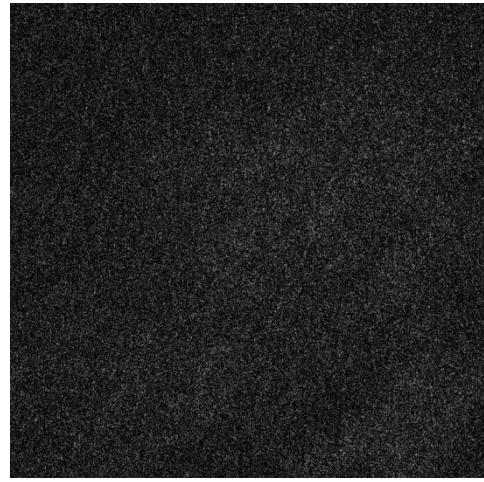


Fig. 39 Barcelona dataset 24 subset 2 location:
X 5,100 -> 5,900 | Y 630 -> 1,430 Pixels

2.5. *Concerns over some images*

In figure 36, there is a bright spot in the middle that might indicate the presence of a ship, which could adversely affect the statistical distribution, therefore this anomaly is noted and logged. The waves in the remainder of the subsets appear to be free from the direct influence of other ships. An example of ship interference can be seen in figures 40 and 41. In figure 40, the wake generated by the ship can be clearly seen. These ship wakes, known as Kelvin wake patterns, disrupt the measurement of the background wind generated waves. The recognition of the unique Kelvin wake patterns in the ocean is a key method that ships can be identified within SAR images. As detailed by Zilmon et al [9] there are strict physics-based parameters present in these Kelvin wake patterns. Some the leading work on detection of ships within SAR images has been carried out by the AssenSAR Research Group and their paper [10] goes further into the parameters of extracting and finding the Kelvin wake patterns in SAR images.

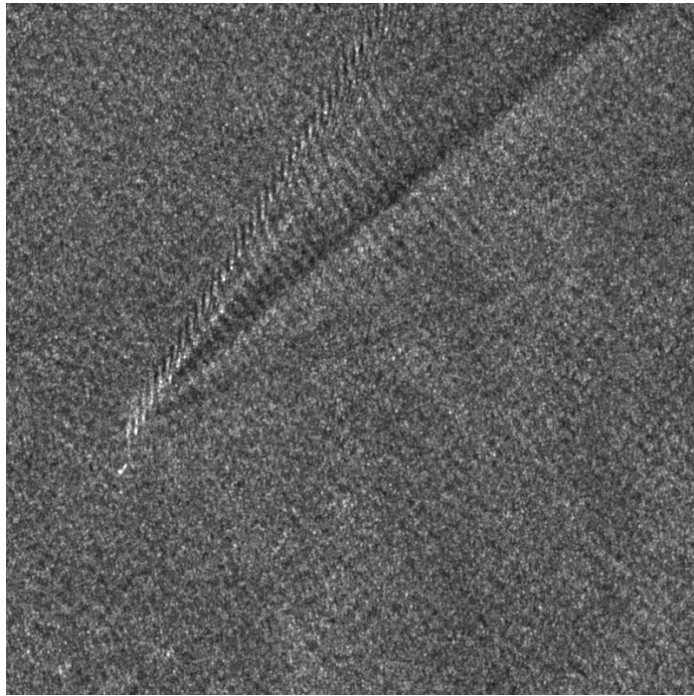


Fig. 40 USA Gulf of Mexico - Kelvin wake pattern behind a moving ship

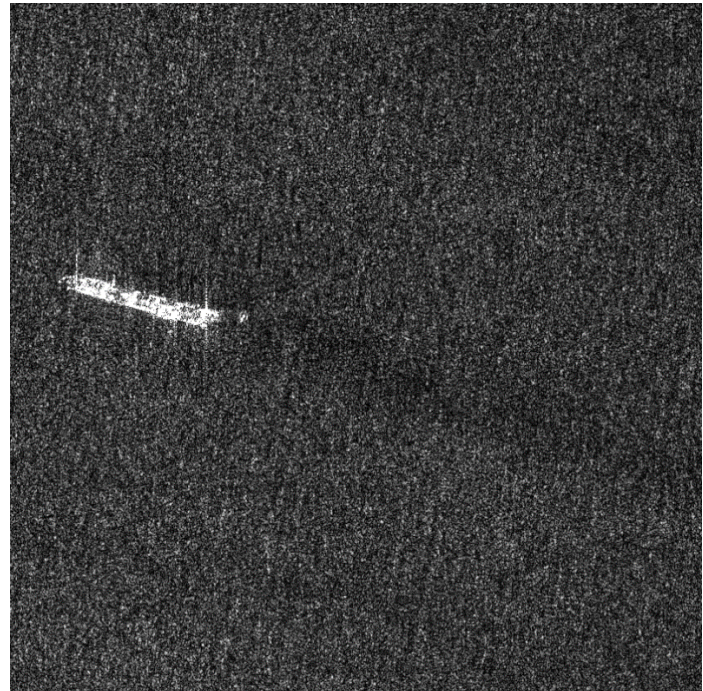


Fig.41 Barcelona dataset 1 - freighter moving slowly

3. Dataset Statistical Analysis

3.1. Usage of statistical models

With all the data denoised, each subset was then statistically analysed.

For each dataset, the data of each of the subsets were normalized between 0 – 1. This process was taken to standardise the end results as best as possible, even with the clear visual differences of each of the subsets. The analysis was conducted within MATLAB, as a continuation of the file structure used by the denoiser.

```
16      %% Normalisation of data between 0-1  
17 - Data = rescale(Data, 0.0000000000000001,1);
```

Fig. 42 code extract rescaling function sets values equally between the points specified

The normalisation function can be seen in figure 42. The reason 0 is not used as the initialisation point is due to errors that develop if the data itself is 0 when it passes through the statistical model. This staggered initialisation point does not affect the distribution of the numbers, it just ensures the starting value is not 0 to resolve any potential errors, as displayed in figure 43.

```
A =
1     2     3     4     5     6
>> Data = rescale(A, 0.000000000000001,1)
Data =
0.0000    0.2000    0.4000    0.6000    0.8000    1.0000
```

Fig. 43 code example showing the rescale function in action

Before running through the statistical models, the data needs to be casted and changed to the Double data type. This change is necessary for usage in histograms and statistical models. The data will also need to be converted into a single column vector instead of the 800×800 matrix initially input, as shown in figure 44.

```
%% loading data to colom vector to be implemented
for section_config=
% convert matrix to colom vector p extention here meaning pre cast
DataC = reshape(Data,[],1);
%probability functions needed the double data type
DataC = cast(DataC,'double');
end
```

Fig. 44 code extract reshaping and casting data

Once the data has been reshaped and casted, the parameters for different statistical models are obtained and stored with the information regarding the whole data set in their own function per distribution, such as this sample Gamma distribution shown below in figure 45.

1x1 GammaDistribution	
Property	Value
a	8.6634
b	0.0258
DistributionName	'Gamma'
NumParameters	2
ParameterNames	1x2 cell
ParameterDescriptions	1x2 cell
ParameterValues	[8.6634,0.0258]
Truncation	[]
IsTruncated	0
ParameterCovariance	[2.2531e-04,-6.7167e-07;-6.7167e-07,2.1223e-09]
ParameterIsFixed	1x2 logical
InputData	1x1 struct

Fig. 45 code extract, Gamma distribution parameters of for Gulf of Mexico, USA

This process is repeated until all the parameters are obtained for each of the six statistical models, being: K (Kernel), Gamma, Rayleigh, Weibull, Nakagami and Lognormal distribution. Many methods were utilised in obtaining the parameters for each of the statistical distributions, such as maximum likelihood estimation [21]. Though for this project the Statistical toolbox of MATLAB was utilised as this toolbox is often used for understanding of SAR image products.

```
%> Gamma Distribution <https://uk.mathworks.com/help/stats/gamma-distribution.htmls>
pd_gamma = fitdist(DataC, 'gamma');

%probability function pdf gamma distribution
% gama has two paramitors a Scale => a > 0 and b > 0
% pdf y = f(x|a,b) = $1/(b^a*\Gamma(a))x^(a-1)*e^(-x/b)$
% where \Gamma( · ) is the Gamma function
% pd_gamma_u = fitdist(Cu,'gamma')
% testing weather data needed to be sorted pre addition to finding paramitors
```

Fig. 46 code extract of the statistical toolbox, for full equation see (1) in section 1.6.1

The method of each distribution can be found below each of the distribution functions within the code for statistically analysing the SAR images. The code extract displayed in figure 46. is a test function. Initially, there was an assumption that an $m \times n$ matrix could be used with the distribution function, where $m \times n$ could be same value. However, this assumption proved to be mistaken. Accordingly, the code in figure 44 was necessary for the transformation of the data into a column vector.

At this point, the histogram of the data is constructed for each dataset at a bin size of 200. For the sake of analysis, a line of approximation will be used to enable the use of Kullback-Leibler divergence and Euclidean distance models. The constructed histogram for the Gulf of Mexico dataset can be seen below in figure 47.

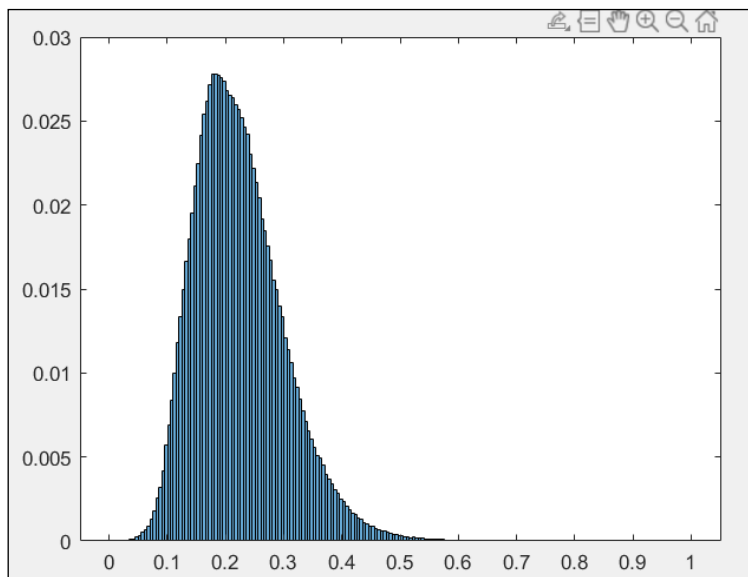


Fig.47 Histogram of the data constructed using 200 bins

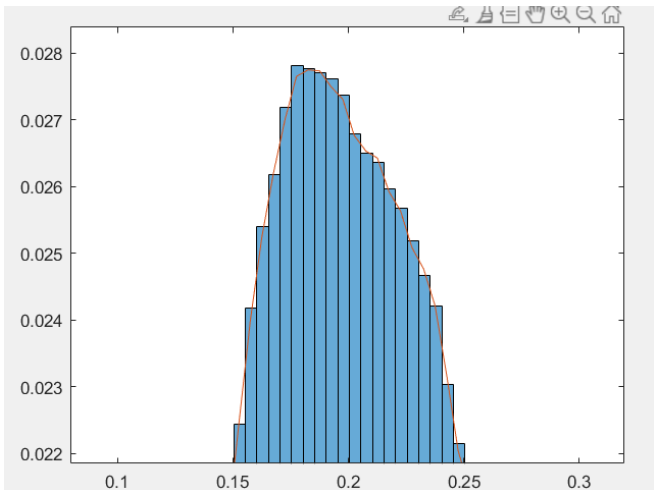


Fig. 48 use of approximation of Y values of the histogram bin data

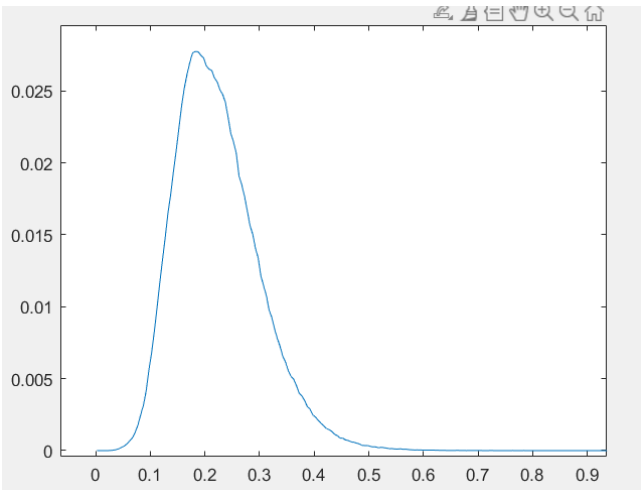


Fig. 49 the approximation of the histogram line

In figure 48, a line of approximation of the Y coordinates of the histogram are taken resulting in the PDF distribution that can be seen in figure 49.

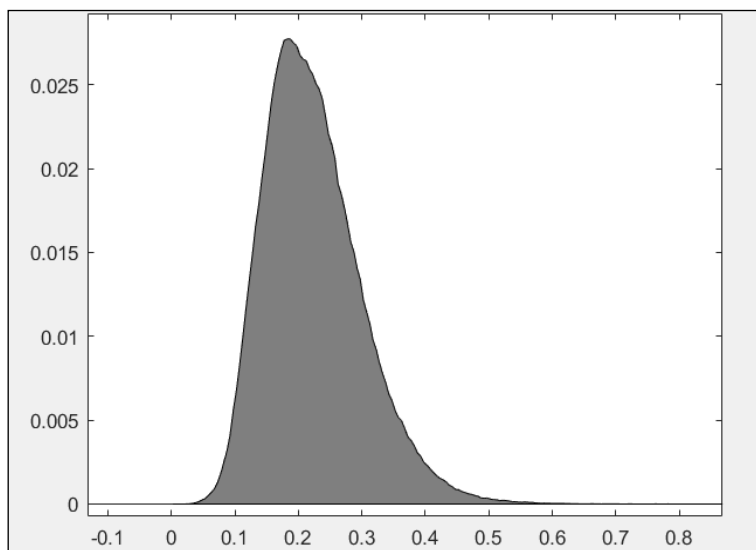


Fig. 50 final histogram with the area filled in

After approximating values for the bin data, the histogram is generated with area shaded as in figure 50. The formula to draw and shade in the histogram is shown in figure 51. Line 107 shows the Y values are divided element wise so that the probability of each bin will sum to a total value of 1.

```

106 - [y, x] = hist(DataC, n);
107 - y = y./sum(y);
108 - plot(x,y);
109 - hold on;
110 - grey = [127 127 127]./255;
111 - area(x,y,'basevalue',0,'FaceColor',grey);

```

Fig. 51 generation of the histogram line and shaded area of the graph

The true reason of the element wise division was to prepare the data for later tests. The utilised data is currently normalised between 0 to 1 because where the sum of bin values exceed 1, the analysis will register as invalid. As such, element wise division is essential, especially in the case of the simulated data.

The Kullback-Leibler divergence and Euclidean distance models are used for identifying the quantitative difference between histogram data and the statistical.

The Kullback-Leibler divergence [33][34], also known as the *relative entropy* between two probability density functions $f(x)$ and $g(x)$ is represented in the following equation.

$$D(f||g) = \int f(x) \log \frac{f(x)}{g(x)} dx \quad (8)$$

The Kullback-Leibler divergence, presented in code format, can be seen below in figure 52.

```
temp = P.*log(P./repmat(Q,[size(P,1) 1]));
```

Fig. 52 code extract of Kullback-Leibler divergence

In the case of the code, $P = f(x)$ and $Q = g(x)$ from the equation above, the divergence is often used for the comparison of histogram formation and other data models.

The other method of testing the difference in distance between the models and the histogram data is Euclidean distance [35]. This model measures the distance between two points in *Euclidean space*, which is effectively the Pythagorean distance between two points. This measurement is conducted element wise for each data point in comparison to the histogram. The equation for Euclidean distance is:

$$d(f,g) = \sum \sqrt{(f-g)^2} \quad (9)$$

Once the histogram information and the distance models have determined the accuracy of each of the statistical model, the analysis may be performed on the SAR images.

The tables and figures detailed within section 3.2 display the results of the analysis of each of the data subsets.

3.2. Statistical modelling of real images

3.2.1. Strait of Gibraltar – GEC SE subset 1

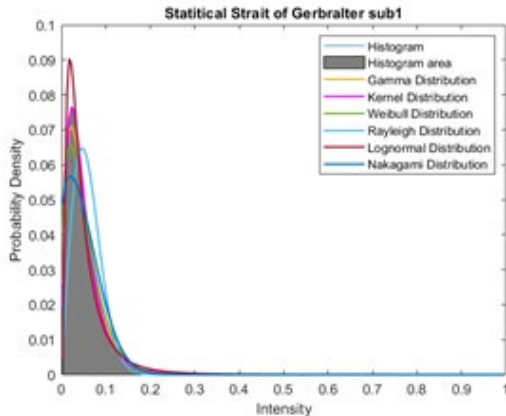


Fig. 53

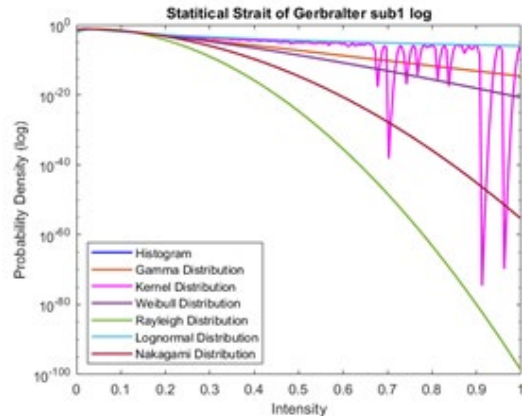


Fig. 54

	K (kernel)	Gamma	Weibull	Rayleigh	Lognormal	Nakagami
Kullback–Leibler divergence	5.7072e-05	0.010454	0.028494	0.23331	0.024184	0.076192
Euclidean distance	0.0013017	0.015709	0.036416	0.095838	0.033918	0.056739

Table 2

3.2.2. Strait of Gibraltar – GEC SE subset 2

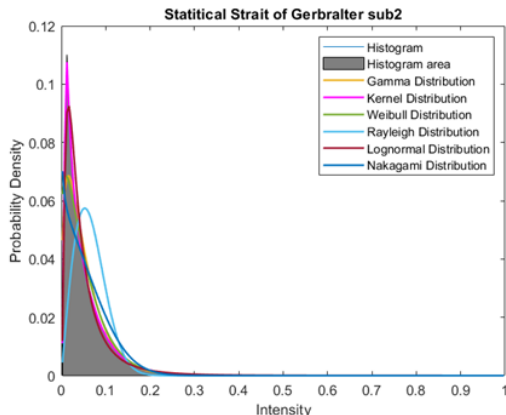


Fig. 55

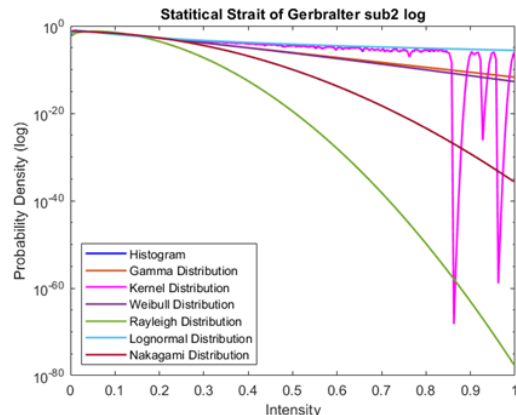


Fig. 56

	K (kernel)	Gamma	Weibull	Rayleigh	Lognormal	Nakagami
Kullback–Leibler divergence	0.0026462	0.060488	0.073697	0.47638	0.014965	0.14362
Euclidean distance	0.008822	0.068713	0.078765	0.15793	0.035978	0.10218

Table 3

3.2.3. Gulf of Mexico, USA – subset 1

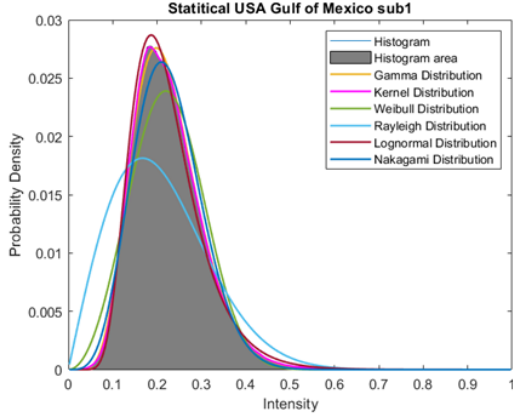


Fig. 57

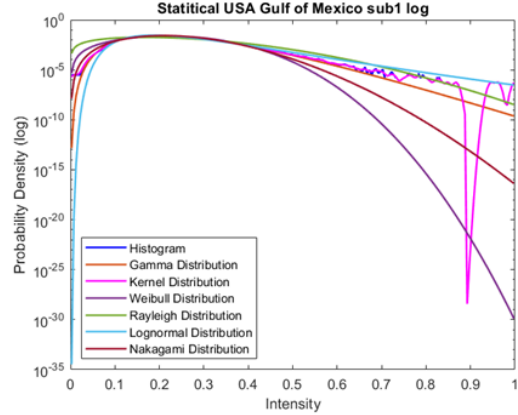


Fig. 58

	K (kernel)	Gamma	Weibull	Rayleigh	Lognormal	Nakagami
Kullback–Leibler divergence	9.446e-05	0.0010724	0.044496	0.17798	0.0075747	0.01349
Euclidean distance	0.00087713	0.0039352	0.02489	0.057003	0.0086132	0.01373

Table 4

3.2.4. Gulf of Mexico, USA – subset 2

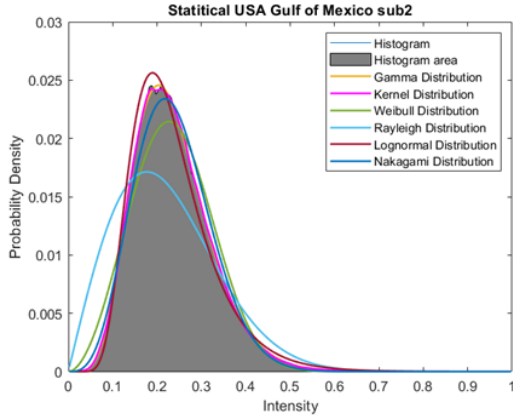


Fig. 59

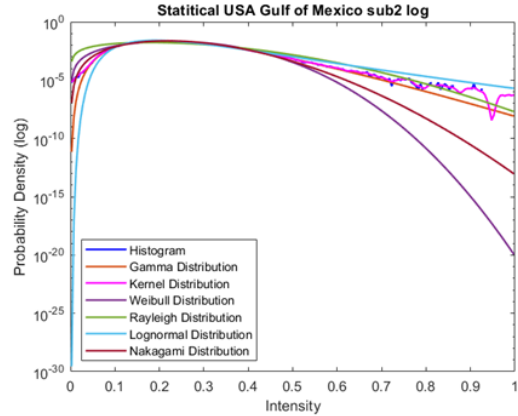


Fig. 60

	K (kernel)	Gamma	Weibull	Rayleigh	Lognormal	Nakagami
Kullback–Leibler divergence	0.00012371	0.00082633	0.035041	0.1336	0.013561	0.010915
Euclidean distance	0.0010941	0.0021804	0.020518	0.047145	0.011626	0.011039

Table 5

3.2.5. Bay of Plenty, New Zealand – subset 1

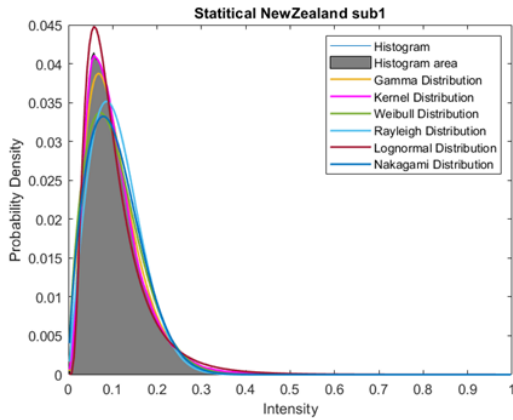


Fig. 61

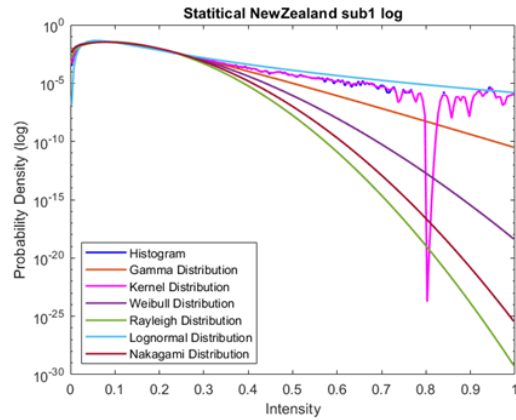


Fig. 62

	K (kernel)	Gamma	Weibull	Rayleigh	Lognormal	Nakagami
Kullback–Leibler divergence	0.00024511	0.0054961	0.036238	0.056705	0.013981	0.04856
Euclidean distance	0.0013351	0.010148	0.028919	0.03478	0.014903	0.032319

Table 6

3.2.6. Bay of Plenty, New Zealand – subset 2

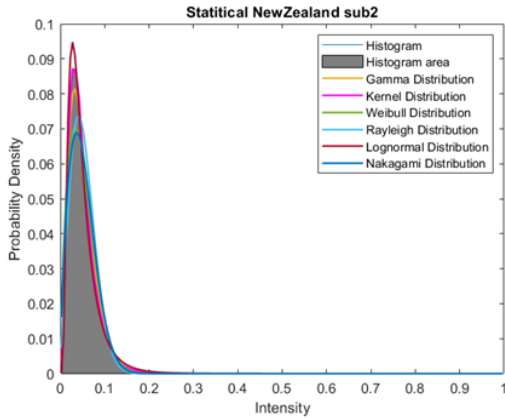


Fig. 63

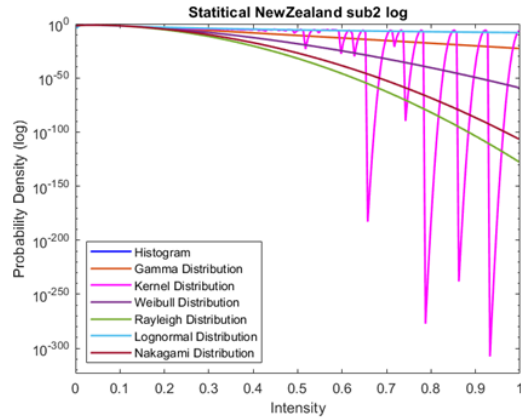


Fig. 64

	K (kernel)	Gamma	Weibull	Rayleigh	Lognormal	Nakagami
Kullback–Leibler divergence	7.818e-05	0.0078621	0.043166	0.071768	0.01321	0.060097
Euclidean distance	0.00085686	0.015456	0.044345	0.053655	0.023201	0.049818

Table 7

3.2.7. *Barcelona, Spain – dataset 1 subset 1*

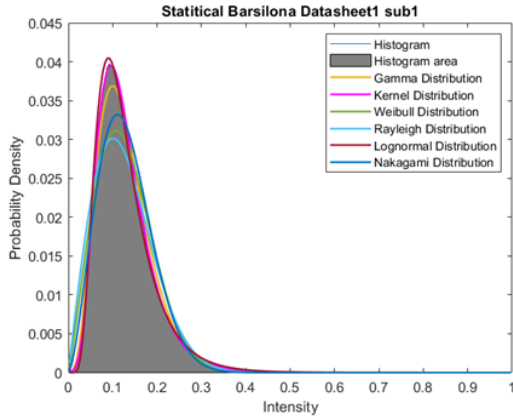


Fig. 65

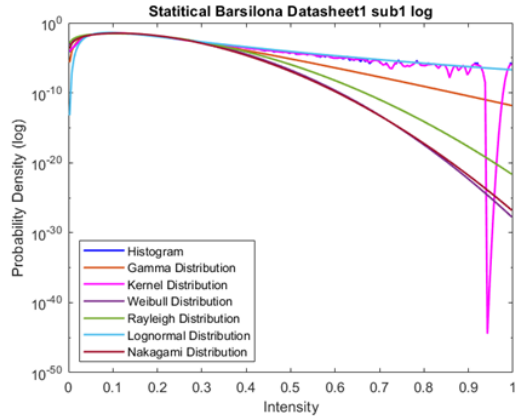


Fig. 66

	K (kernel)	Gamma	Weibull	Rayleigh	Lognormal	Nakagami
Kullback–Leibler divergence	9.2953e-05	0.0079654	0.057378	0.062268	0.0078827	0.045574
Euclidean distance	0.00095079	0.011342	0.034622	0.038491	0.0091119	0.029362

Table 8

3.2.8. *Barcelona, Spain – dataset 1 subset 2*

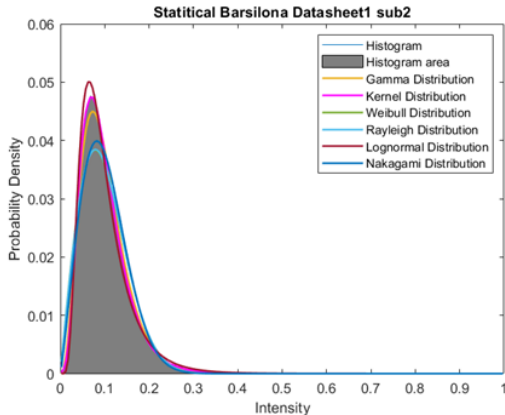


Fig. 67

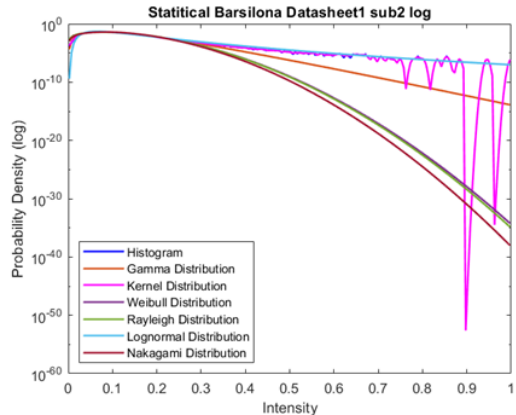


Fig. 68

	K (kernel)	Gamma	Weibull	Rayleigh	Lognormal	Nakagami
Kullback–Leibler divergence	0.0001002	0.0060829	0.047577	0.047596	0.0098516	0.044835
Euclidean distance	0.00088034	0.010195	0.034021	0.033874	0.01269	0.031543

Table 9

3.2.9. *Barcelona, Spain – dataset 5 subset 1*

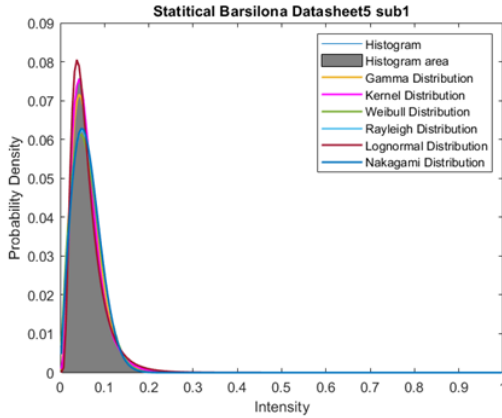


Fig. 69

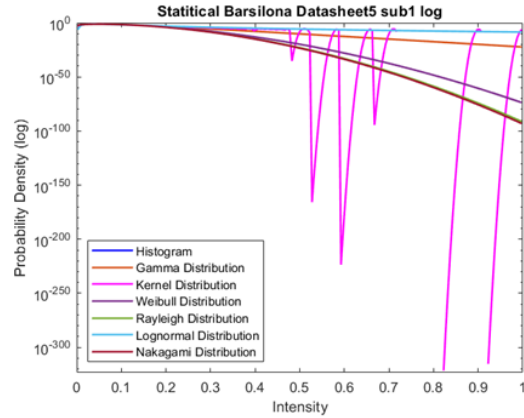


Fig. 70

	K (kernel)	Gamma	Weibull	Rayleigh	Lognormal	Nakagami
Kullback–Leibler divergence	3.2008e-05	0.0061062	0.044594	0.046562	0.013028	0.046417
Euclidean distance	0.00062756	0.012613	0.042007	0.041127	0.018772	0.040711

Table 10

3.2.10. *Barcelona, Spain – dataset 5 subset 2*

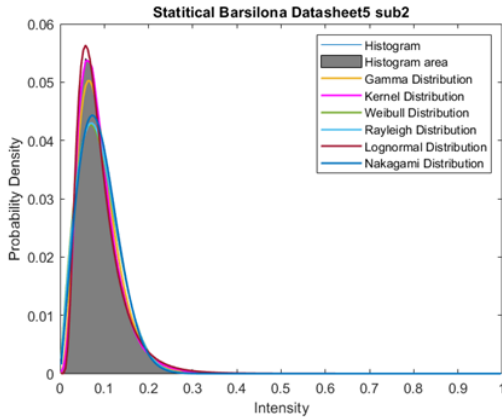


Fig. 71

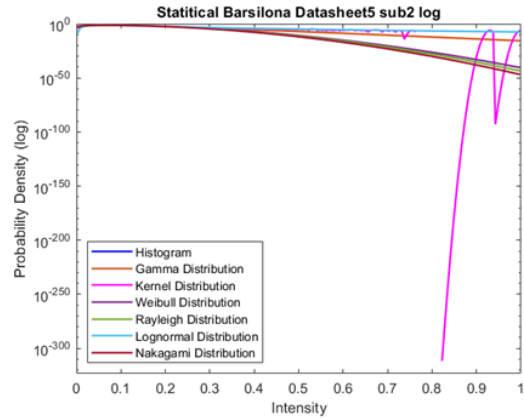


Fig. 72

	K (kernel)	Gamma	Weibull	Rayleigh	Lognormal	Nakagami
Kullback–Leibler divergence	8.7794e-05	0.0090041	0.054723	0.055035	0.0083825	0.053138
Euclidean distance	0.0011431	0.014406	0.040001	0.039453	0.011545	0.037498

Table 11

3.2.11. *Barcelona, Spain – dataset 8 subset 1*

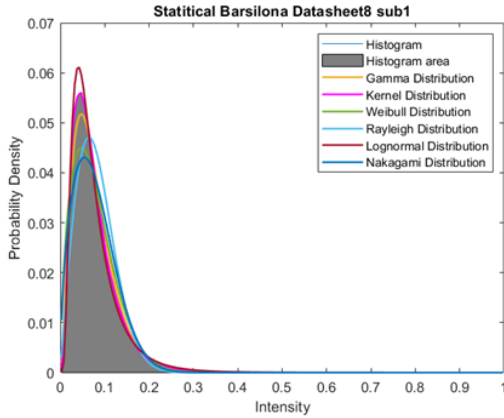


Fig. 73

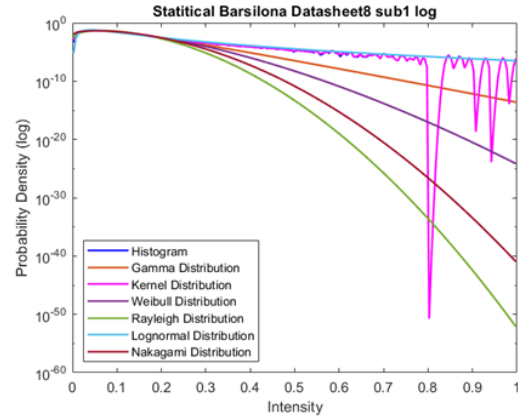


Fig. 74

	K (kernel)	Gamma	Weibull	Rayleigh	Lognormal	Nakagami
Kullback–Leibler divergence	0.0002558	0.012633	0.04951	0.096756	0.0069882	0.073308
Euclidean distance	0.0013697	0.016648	0.038436	0.05212	0.013727	0.045148

Table 12

3.2.12. *Barcelona, Spain – dataset 8 subset 2*

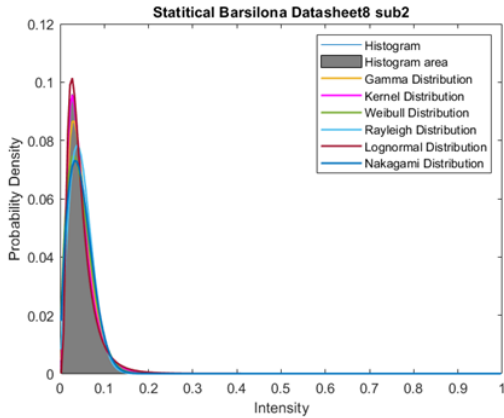


Fig. 75

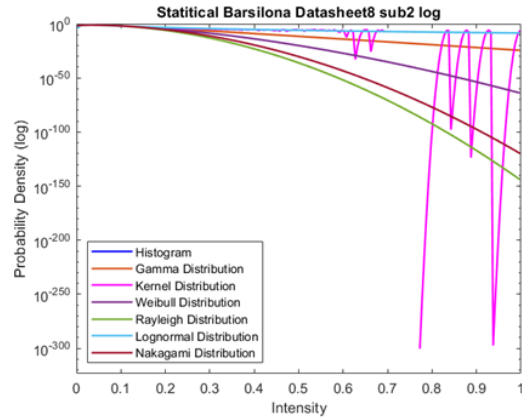


Fig. 76

	K (kernel)	Gamma	Weibull	Rayleigh	Lognormal	Nakagami
Kullback–Leibler divergence	4.1601e-05	0.011689	0.051856	0.08285	0.0066382	0.070705
Euclidean distance	0.00058655	0.02161	0.051037	0.061983	0.015311	0.057326

Table 13

3.2.13. Barcelona, Spain – dataset 12 subset 1

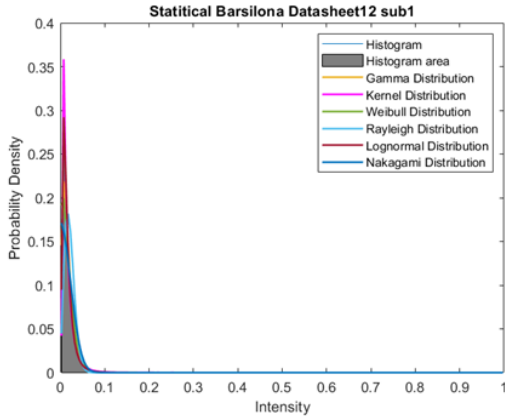


Fig. 77

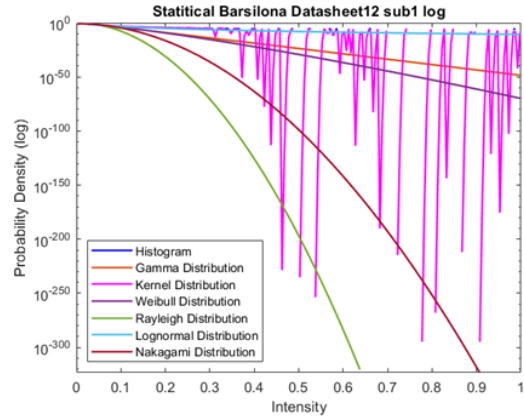


Fig. 78

	K (kernel)	Gamma	Weibull	Rayleigh	Lognormal	Nakagami
Kullback–Leibler divergence	0.022016	0.083947	0.11768	Inf	0.0089077	Inf
Euclidean distance	0.05484	0.13491	0.17626	0.26016	0.049575	0.20867

Table 14

3.2.14. Barcelona, Spain – dataset 12 subset 2

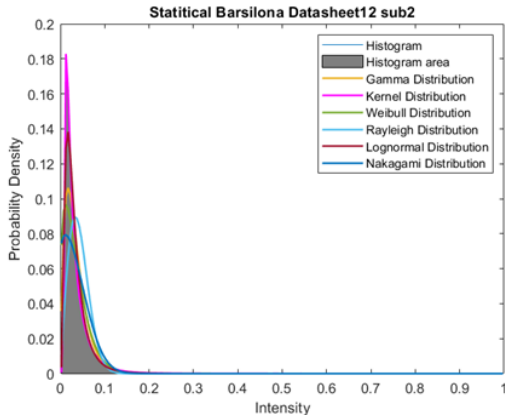


Fig. 79

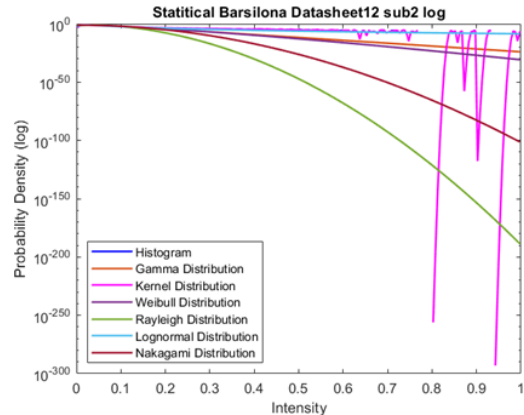


Fig. 80

	K (kernel)	Gamma	Weibull	Rayleigh	Lognormal	Nakagami
Kullback–Leibler divergence	0.00022517	0.12862	0.18387	0.46878	0.026479	0.29035
Euclidean distance	0.0050905	0.11441	0.14466	0.19295	0.065429	0.16797

Table 15

3.2.15. Barcelona, Spain – dataset 17 subset 1

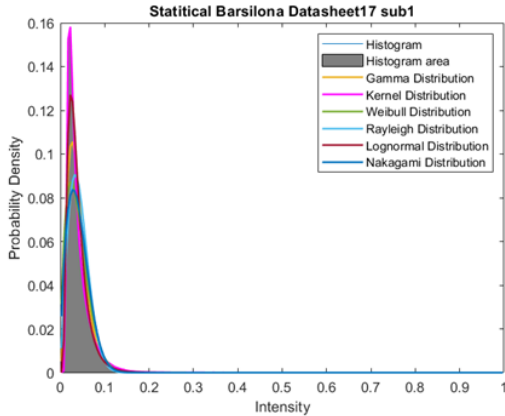


Fig. 81

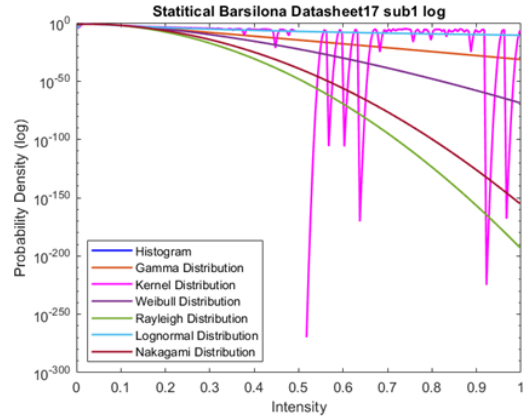


Fig. 82

	K (kernel)	Gamma	Weibull	Rayleigh	Lognormal	Nakagami
Kullback–Leibler divergence	6.4554e-05	0.10589	0.18675	0.24443	0.03441	0.2276
Euclidean distance	0.0022287	0.10006	0.13246	0.14189	0.062426	0.13968

Table 16

3.2.16. Barcelona, Spain – dataset 17 subset 2

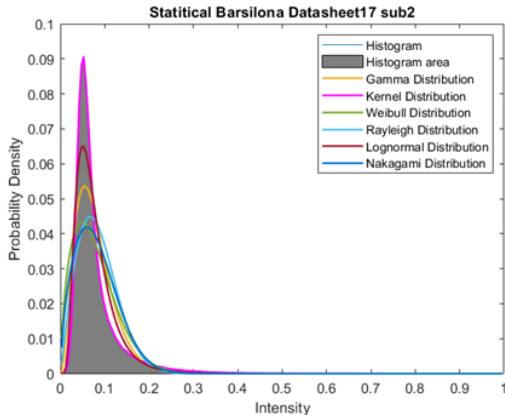


Fig. 83

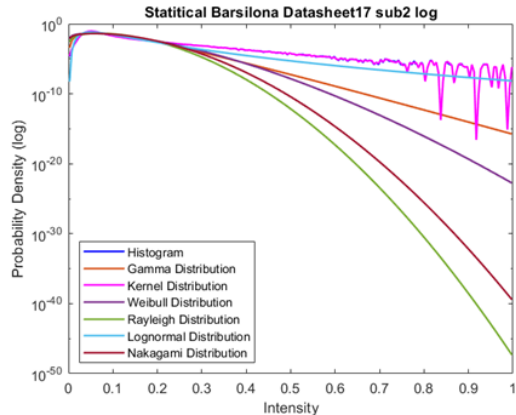


Fig. 84

	K (kernel)	Gamma	Weibull	Rayleigh	Lognormal	Nakagami
Kullback–Leibler divergence	2.8148e-05	0.14597	0.2456	0.30216	0.054069	0.28903
Euclidean distance	0.00063478	0.08498	0.11401	0.11505	0.056039	0.11686

Table 17

3.2.17. Barcelona, Spain – dataset 20 subset 1

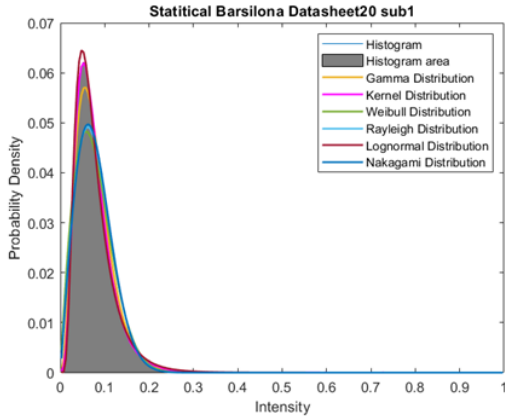


Fig. 85

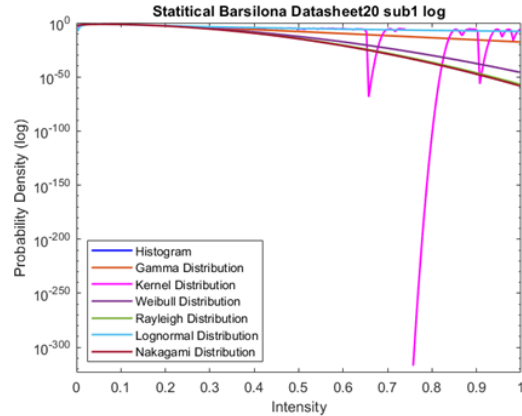


Fig. 86

	K (kernel)	Gamma	Weibull	Rayleigh	Lognormal	Nakagami
Kullback–Leibler divergence	7.3558e-05	0.01203	0.061585	0.064288	0.0057842	0.064041
Euclidean distance	0.00090844	0.016575	0.044082	0.043073	0.010479	0.042566

Table 18

3.2.18. Barcelona, Spain – dataset 20 subset 2

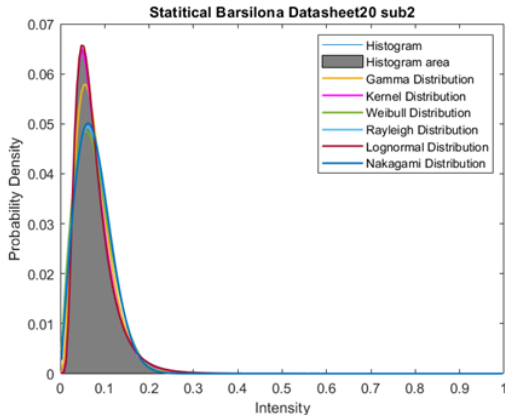


Fig. 87

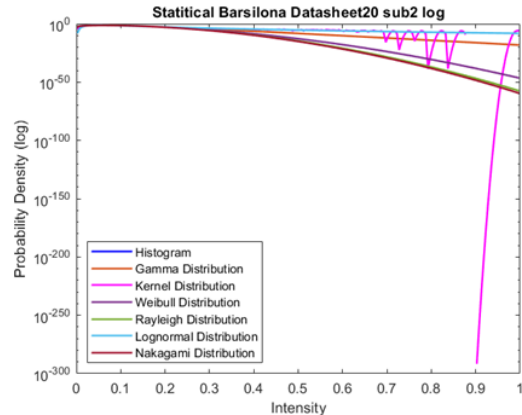


Fig. 88

	K (kernel)	Gamma	Weibull	Rayleigh	Lognormal	Nakagami
Kullback–Leibler divergence	9.8877e-05	0.019958	0.07662	0.079195	0.00093873	0.078741
Euclidean distance	0.0011354	0.024636	0.051143	0.050592	0.0042803	0.050079

Table 19

3.2.19. Barcelona, Spain – dataset 21 subset 1

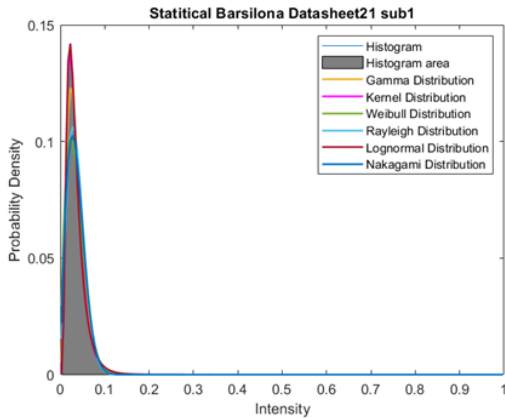


Fig. 89

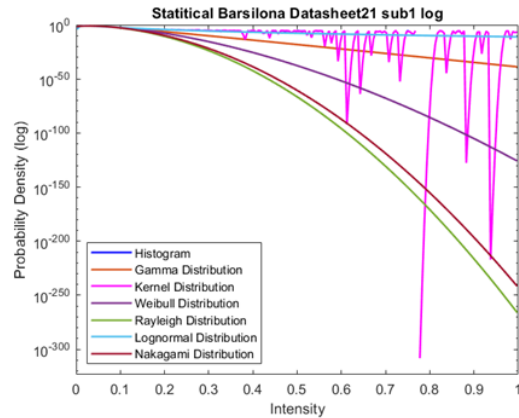


Fig. 90

	K (kernel)	Gamma	Weibull	Rayleigh	Lognormal	Nakagami
Kullback–Leibler divergence	5.7032e-05	0.022043	0.086271	0.11005	0.0042758	0.10703
Euclidean distance	0.0011217	0.033093	0.07565	0.076219	0.0085406	0.077028

Table 20

3.2.20. Barcelona, Spain – dataset 21 subset 2

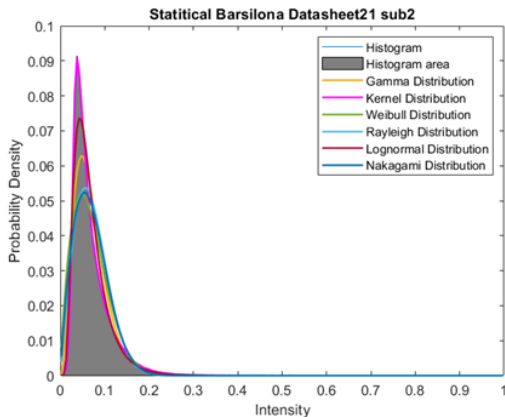


Fig. 91

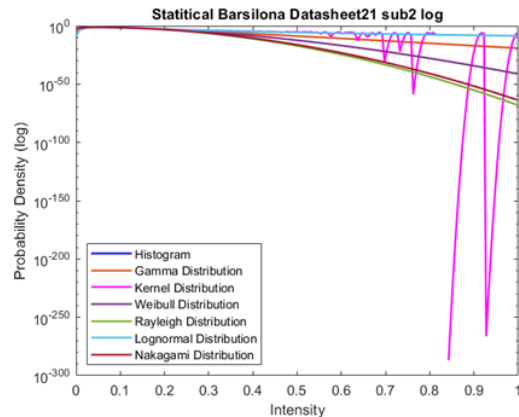


Fig. 92

	K (kernel)	Gamma	Weibull	Rayleigh	Lognormal	Nakagami
Kullback–Leibler divergence	6.3645e-05	0.069458	0.14137	0.15713	0.018968	0.15568
Euclidean distance	0.001371	0.064946	0.089084	0.091176	0.038959	0.091169

Table 21

3.2.21. *Barcelona, Spain – dataset 24 subset 1*

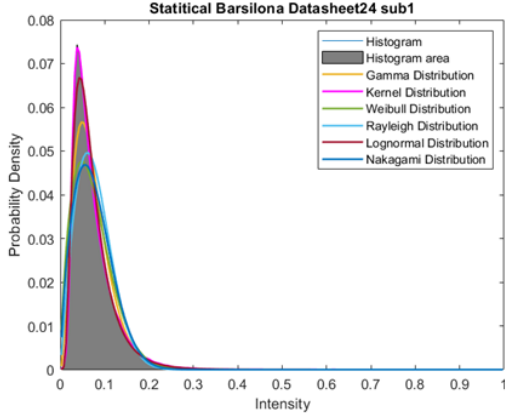


Fig. 93

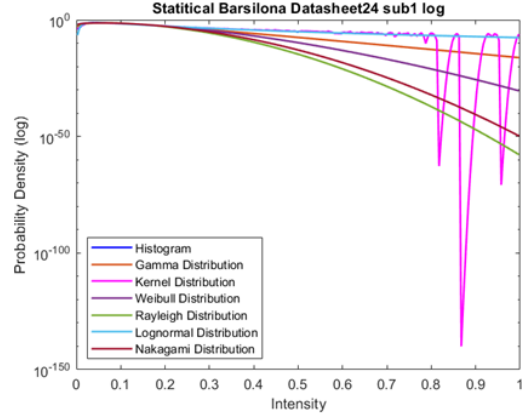


Fig. 94

	K (kernel)	Gamma	Weibull	Rayleigh	Lognormal	Nakagami
Kullback–Leibler divergence	0.00012568	0.046493	0.10756	0.13802	0.0058334	0.12971
Euclidean distance	0.0016145	0.046195	0.069011	0.074612	0.020281	0.073129

Table 22

3.2.22. *Barcelona, Spain – dataset 24 subset 2*

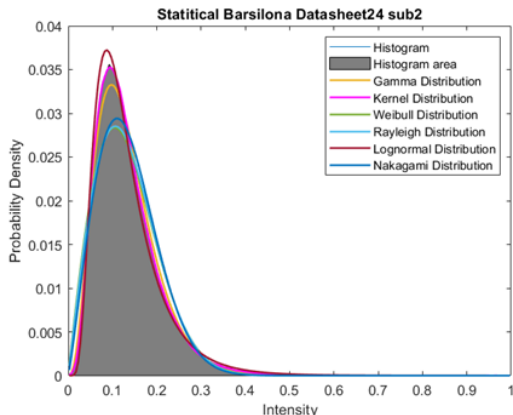


Fig. 95

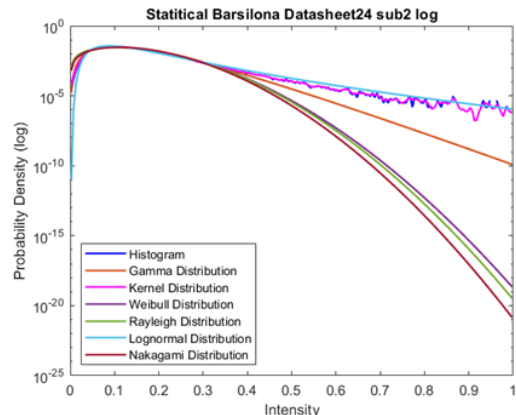


Fig. 96

	K (kernel)	Gamma	Weibull	Rayleigh	Lognormal	Nakagami
Kullback–Leibler divergence	0.00017231	0.0069195	0.049454	0.04963	0.0069446	0.047678
Euclidean distance	0.0010276	0.0095716	0.029968	0.029675	0.01034	0.028232

Table 23

3.3. Analysis of results from normal images

The statistical models of the 22 images can be seen above in figures 53 to 96, with the odd numbered figures being the normal subset PDF and the even numbers being the logarithmic representation of the data. The results of the Kullback-Leibler divergence and Euclidean distance are found in tables 2 to 23 for each subset of data.

The ranking of which distribution was closest to fitting the histogram data for each of the 22 images is presented in table 24 below, with 1st implying best fit and 6th being the worse fit.

Rank	1 st	2 nd	3 rd	4 th	5 th	6 th
K (kernel)	21	1	0	0	0	0
Lognormal	1	13	7	0	0	0
Gamma	0	8	14	0	0	0
Nakagami	0	0	1	8	11	2
Weibull	0	0	0	13	3	6
Rayleigh	0	0	0	0	8	14

Table 24 tallied results of best fit for the real images

From the results tallied, as presented in table 24, the K distribution was the best fit in all but one case. The lone image where the K distribution did not produce the best fit was Barcelona dataset 12 subset 1, see figure 30. For this image, the Lognormal distribution was the closest fit as the image itself is dark and potentially hard to distinguish, which may account for the difference in results. For images other than the Barcelona data sets, the Gamma distribution produced the 2nd best fit in 5 of the 6 images. Lognormal distribution was the second best in over half of the cases for the total data set. The K, Lognormal and Gamma distribution models were the clear winners. The Weibull, Rayleigh and Nakagami distributions proved to be ineffective with Rayleigh being the worst for representing the wind generated waves.

Across all but one of the images, the K distribution was able to accurately represent the peak of the PDF. However, when inspecting the log graphs, after 0.5 intensity, there are extreme variations in the tail data in most cases. These variations are most evident in the Barcelona dataset 12 subset 1, figure 78, which is marked by extreme variation. Overall, the K distribution accurately depicts the peak of the data, however, if the tail of the data is of interest, the K distribution should not be used as it produces high variations.

Lognormal distribution tends to overshoot the estimate at the peak of the histogram data, see figure 91 on the previous page, unless the data has a sharp peak. In this case, the distribution will undershoot the peak result as shown in figure 89. The tail end of the data for the PDF is closely followed, particularly between 0.4 intensity to 1, where it is the closest to the histogram data, and much more consistent than K distribution data.

Gamma distribution will generally under shoot the peak portion of the histogram data, though it does represent the mid to beginning of tail information to an adequate level. The model does deviate more than lognormal for tail data and therefore it represents this data adequately but not nearly as well as the K and Lognormal distributions.

The remaining three models are not nearly as close to the first three mentioned with Rayleigh being the worst for the representation of the data. When inspecting the tail end of the data, all three wildly deviate from the histogram values making them poor candidates for any part in representing sea surface wind waves.

It should be noted that the Rayleigh distribution does much better at representing surfaces that are not water.

For normal data related to wind generated waves, the K distribution was the best at representing the peak of the data sets, while the Lognormal distribution was the best for the tail end of the data. The use of both tools in tandem will produce the best results when developing complex models of this data.

4. Simulations

4.1. *Data models for simulation*

With the constructed histogram data recorded and documented, all the data was shared with the AssenSAR Research Group. From the data and selected subsets, 5 of the 22 images were chosen to be simulated.

In order for the simulator to perform well, it needs to start with an image which shows a clearly defined wind generated wave with a distinction between subsequent waves. One image which clearly met this criterion is figure 23 from the Strait of Gibraltar subset 2. This image was selected for use in the initial testing and tuning of the simulator in correspondence between AssenSAR and the author.

The main methods used for the simulation involved Normalized Radar Cross Section (NRCS), mean reflections and velocity bunching. In the documentation, NRCS will be labelled as **S**, and the iteration of the same method will be **SX** where x is a separate letter or number. Velocity bunching will be denoted as an **I**, with same sub notation as **S**.

This thesis focuses on the statistical difference and closeness of the generated modules and will unfortunately not have room to comment on the creation process for the simulated images. For reference, other papers have explored and elaborated in detail on each of the methods used in the creation of these images, being NRCS, mean reflections [36] and velocity bunching [37].

The initial images were tested at a 400 x 400 pixel scale, as at that point, the optimizations were not in place to be able to simulate a larger image in a reasonable time. The Initial tests for the four smaller images generated box plots and normalised histograms which were compared to the original

image. After improvements, tests were conducted on the larger 800 x 800 pixel images with better results.

The initial image, after denoising, was taken at coordinates = [25 25 400 400] and can be seen in figure 97 below. The next four figures contain the simulated images.

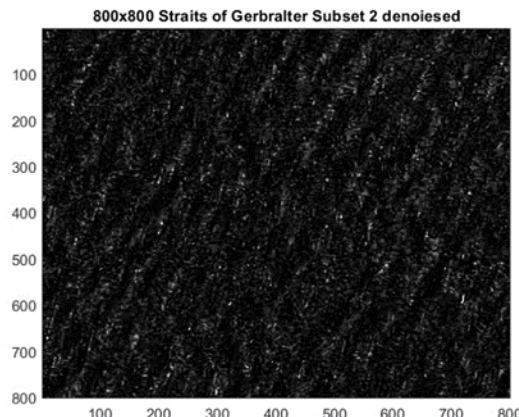


Fig. 97 Strait of Gibraltar - GEC, SE subset 2 denoised

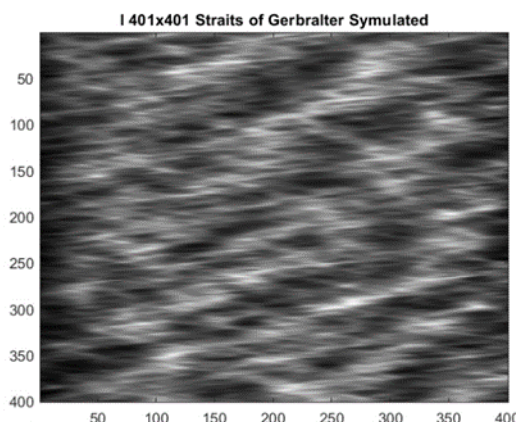


Fig. 98 Strait of Gibraltar - GEC, SE subset 2 I simulated

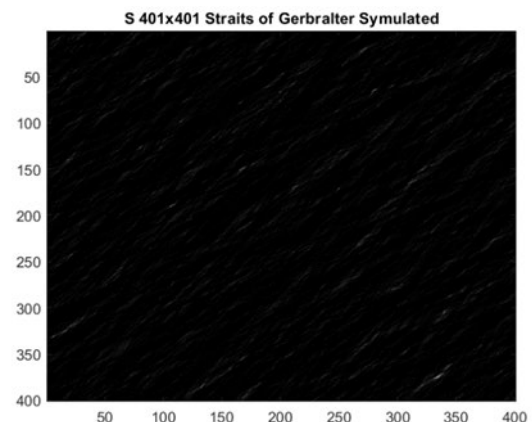


Fig. 99 Strait of Gibraltar - GEC, SE subset 2 S simulated

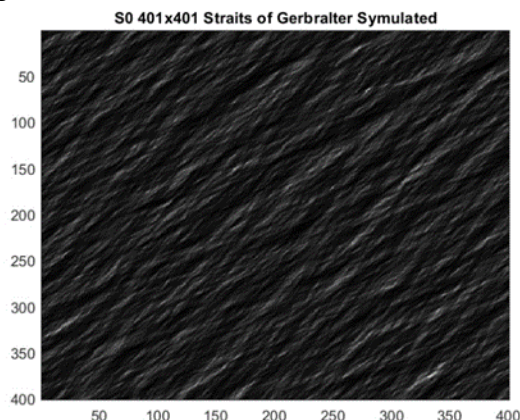


Fig. 100 Strait of Gibraltar - GEC, SE subset 2
SO simulated

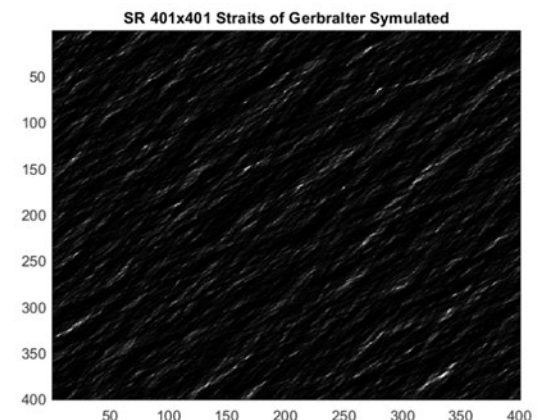


Fig. 101 Strait of Gibraltar - GEC, SE subset 2
SR simulated

4.2. 1st iteration test results for simulated 400 x 400 images

To better understand the simulated data, the following simulated images box plots and comparisons to the original histogram data are presented below for both the normalised and un-normalised versions of the data. The reason for presenting both the normalised and un-normalised versions of the data is due to the method of simulation. From the testing conducted, the two metrics for distance were the same for both the normalised and unnormalised data, therefore the distance values will only be displayed once after both sets of figures. The unnormalised will be followed by normalised sets of data.

4.2.1. Simulated I image

a) Unnormalised

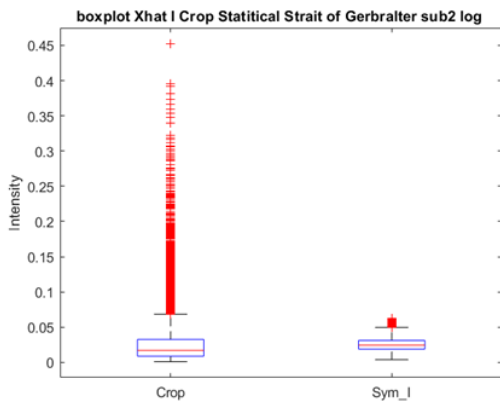


Fig. 102

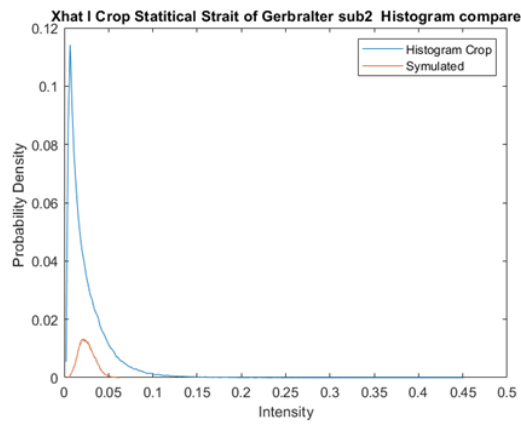


Fig. 103

b) Normalised

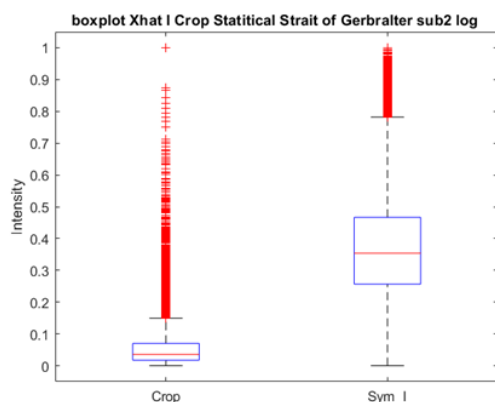


Fig. 104

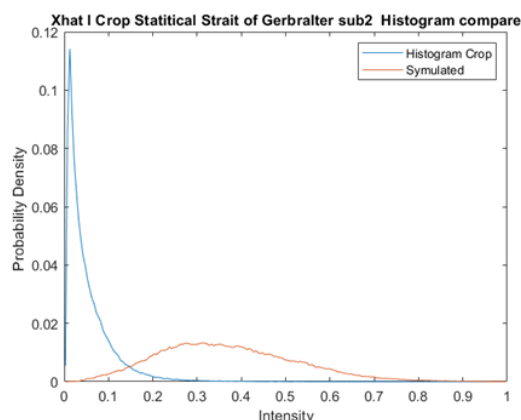


Fig. 105

Kullback–Leibler divergence	4.8796	Euclidean distance	0.24873
-----------------------------	--------	--------------------	---------

Table. 25 Simulated I divergence values

4.2.2. Simulated S image

a) Unnormalised

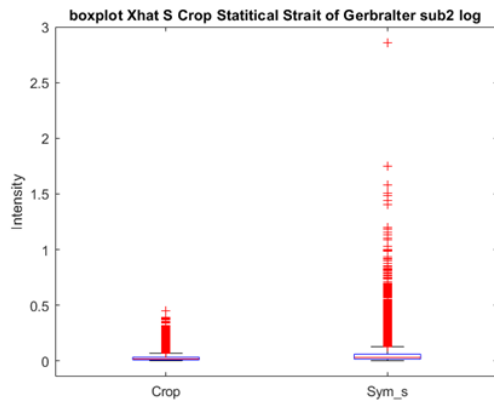


Fig. 106

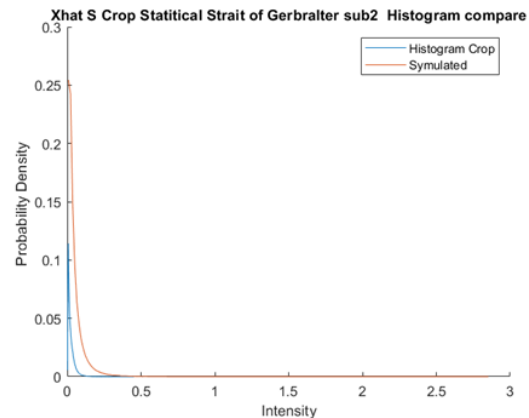


Fig. 107

b) Normalised

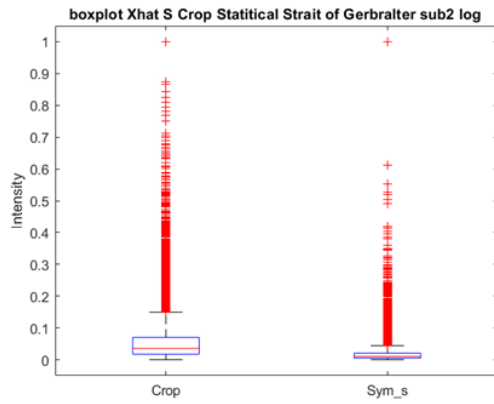


Fig. 108

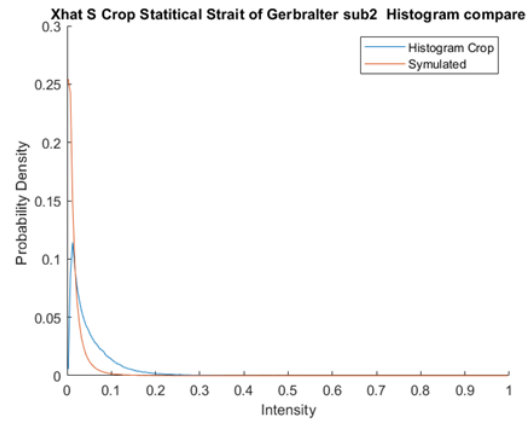


Fig. 109

Kullback–Leibler divergence	INF	Euclidean distance	0.30802
-----------------------------	-----	--------------------	---------

Table. 26 Simulated S divergence values

4.2.3. Simulated SR image

a) Unnormalised

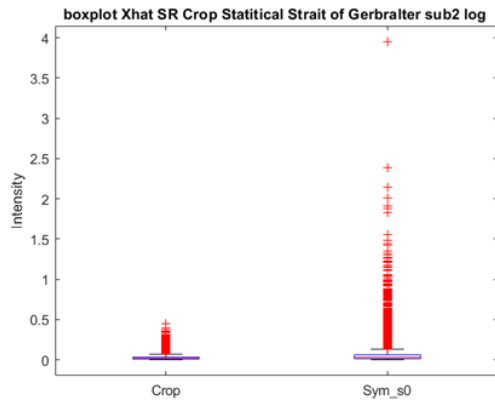


Fig. 110

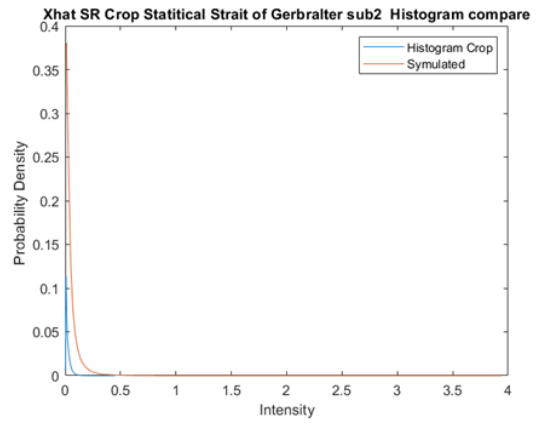


Fig. 111

b) Normalised

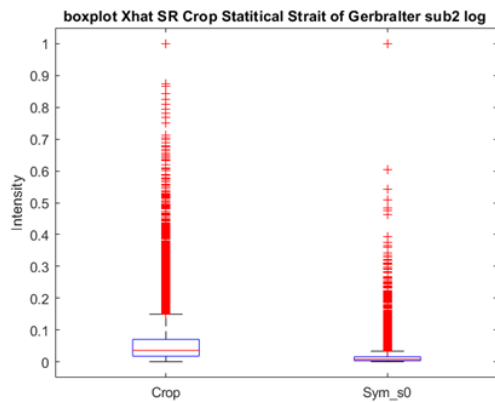


Fig. 112

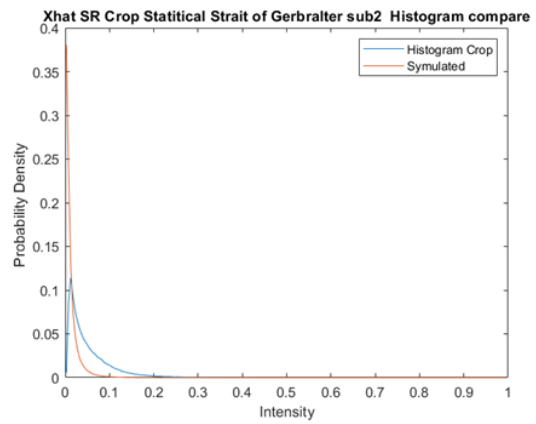


Fig. 113

Kullback–Leibler divergence	INF	Euclidean distance	0.41956
-----------------------------	-----	--------------------	---------

Table. 27 Simulated SR divergence values

4.2.4. Simulated S0 image

a) Unnormalised

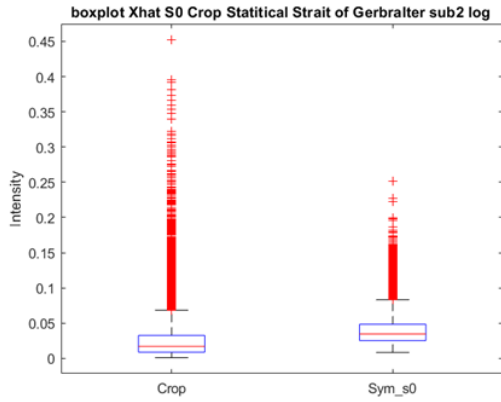


Fig. 114

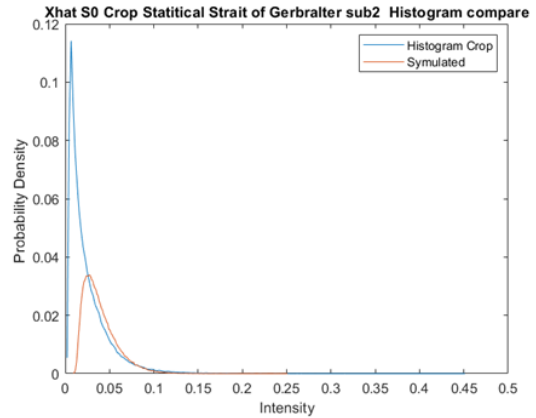


Fig. 115

b) Normalised

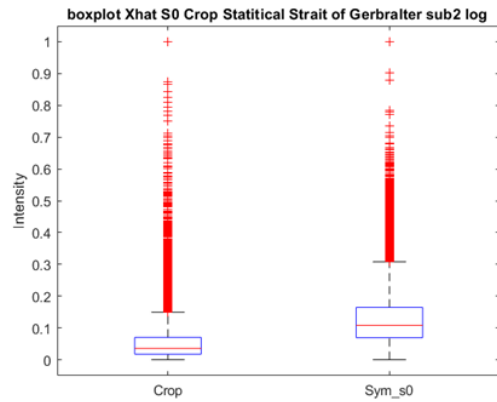


Fig. 116

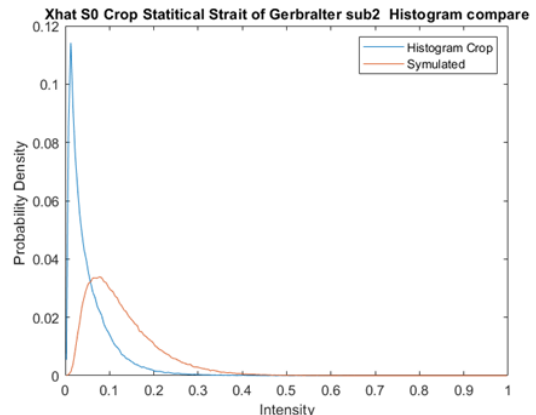


Fig. 117

Kullback–Leibler divergence	INF	Euclidean distance	0.2084
-----------------------------	-----	--------------------	--------

Table. 28 Simulated S0 divergence values

4.3. Review of results of 1st iteration simulated images

The original SAR images are predominantly dark with lighter specks or streaks indicating wind generated sea waves. In this subset, the original image can be seen in figure 97 with small white specks signifying the crest of sea waves.

Looking at the Euclidean distance alone, the simulated S0 image provides the best result. The S0 image also has the closest similarity to the normal histogram data, though the best result comes from the unnormalised version where the data from the peak to the tail closely follows the histogram data with the peak being fractionally off the real histogram data as seen in figure 115. When normalised, the data spread is much greater which is clearly seen in the box plot and histogram of figures 116 and 117.

The simulated I images involving velocity bunching had the worst of the outcomes, especially when observing the normalised version with the peak of the histogram data is closer to the midpoint of the graph creating an image, figure 98, that was much brighter than expected.

The simulated SR image has become very dark as seen in the box plot, figure 112, where the median of the data is less than 0.05, indicating little to no discernible wave data in the normalised case. While the unnormalized SR image is also very dark, the maximum value is 4, indicating that there is at least some minor wave data being captured that is being washed out in the normalized view. In the case of the S image, the initial box plot spreads for the unnormalized versions present similar mean values, though this case also shows an outlier return with a value near 3. When normalised, S shows a very tight median with a value less than 0.05 and below that of the mean histogram data.

The results of this test enabled the tuning of the coefficients for better results in follow-on simulations.

4.4. 2nd iteration test results for simulated 800 x 800 images

Incorporating iterative changes from the previous 400 x 400 set, one 800 x 800 pixel subset was selected for further modelling related to the Strait of Gibraltar subset 2 image. Four simulations were run on this image with the first two using the velocity bunching technique, which will be denoted as I1 and I2. The second two simulations used the NRCS, mean reflections technique, which we denoted as S and S2.

4.4.1. Simulated I image

a) Unnormalised

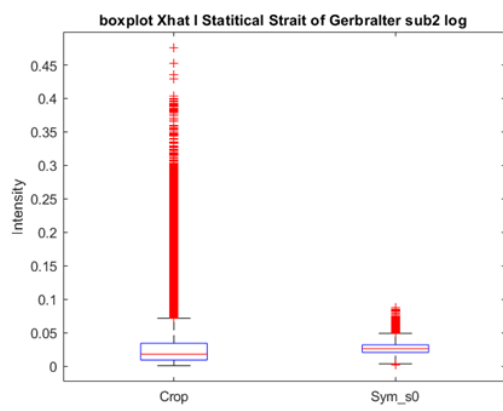


Fig. 118

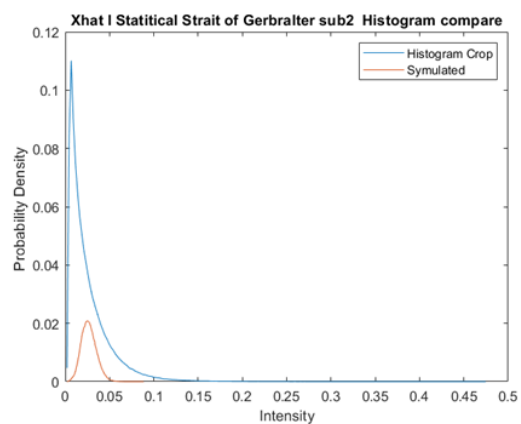


Fig. 119

b) Normalised

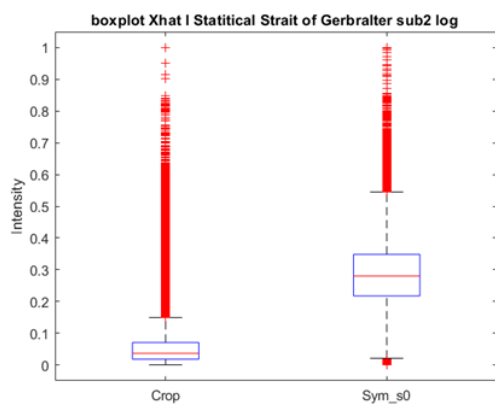


Fig. 120

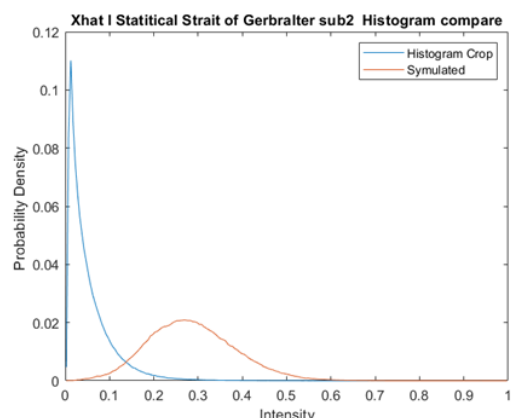


Fig. 121

Kullback–Leibler divergence	INF	Euclidean distance	0.25559
-----------------------------	-----	--------------------	---------

Table. 29 Simulated I divergence values

4.4.2. Simulated I2 image

a) Unnormalised

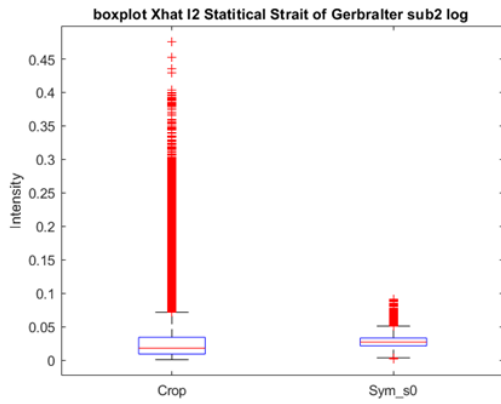


Fig. 122

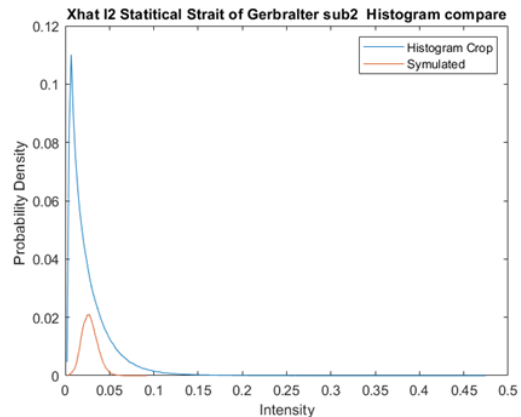


Fig. 123

b) Normalised

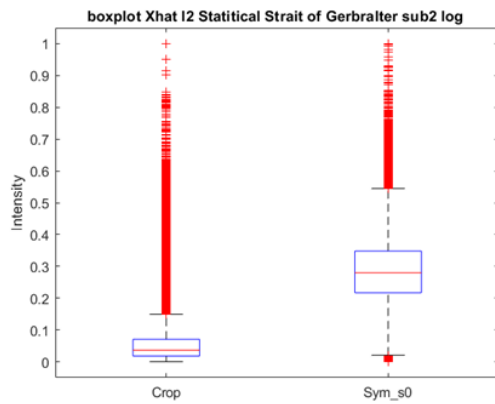


Fig. 124

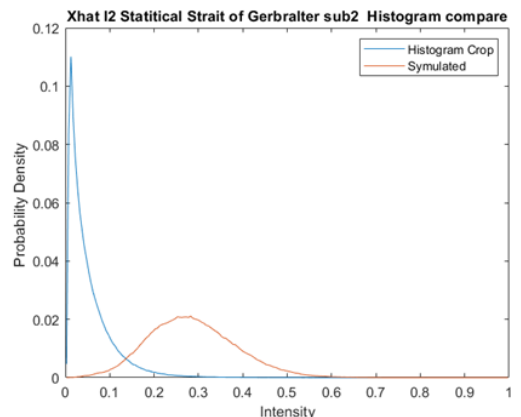


Fig. 125

Kullback–Leibler divergence	INF	Euclidean distance	0.25551
-----------------------------	-----	--------------------	---------

Table. 30 Simulated I2 divergence values

4.4.3. Simulated S image

a) Unnormalised

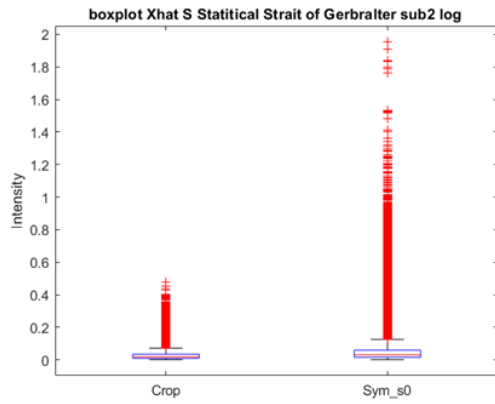


Fig. 126

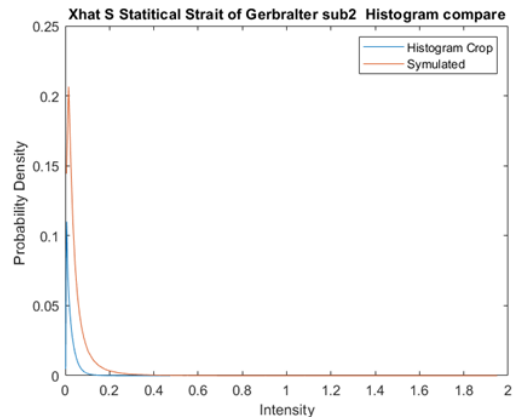


Fig. 127

b) Normalised

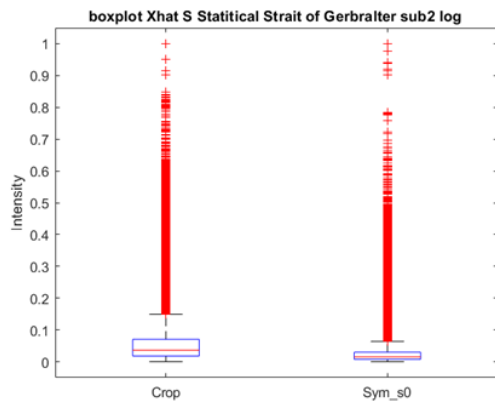


Fig. 128

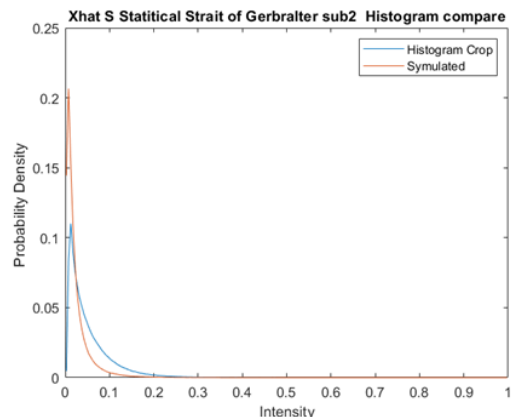


Fig. 129

Kullback–Leibler divergence	INF	Euclidean distance	0.2018
-----------------------------	-----	--------------------	--------

Table. 31 Simulated S divergence values

4.4.4. Simulated S2 image

a) Unnormalised

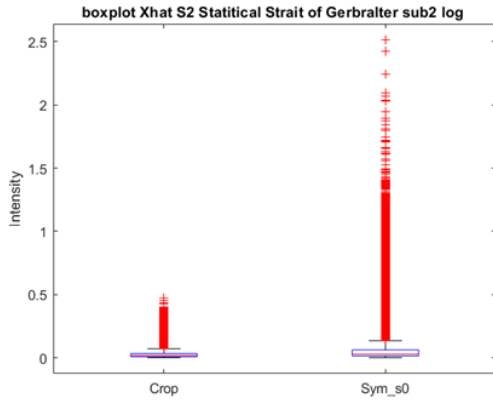


Fig. 130

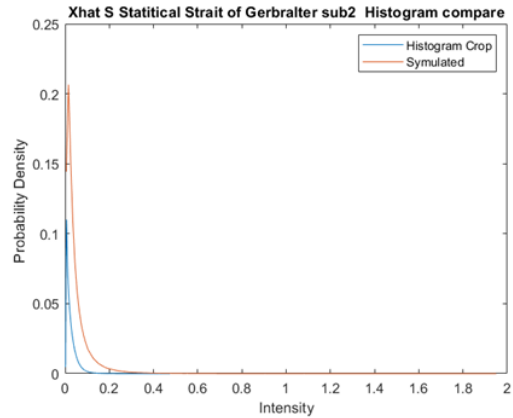


Fig. 131

b) Normalised

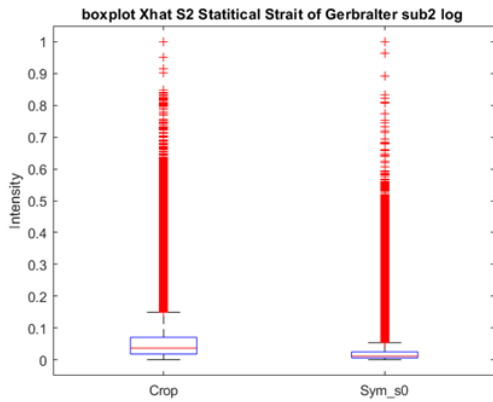


Fig. 132

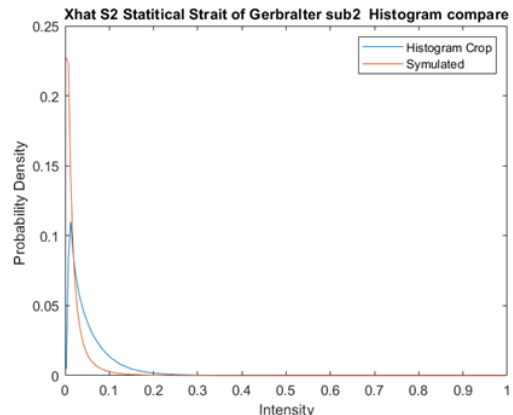


Fig. 133

Kullback–Leibler divergence	INF	Euclidean distance	0.2756
-----------------------------	-----	--------------------	--------

Table. 32 Simulated S2 divergence values

4.5. Review of results of 2nd iteration simulated images

The new simulations of the 800 x 800 image from the Strait of Gibraltar subset 2, figure 97, were expected to see improvement because the 400 x 400 batch were attempting to simulate the entire image while compressing it to one fourth the size to fit the format, generating statistical inaccuracies. Despite these issues, the S0 simulation, unnormalised, seen in figures 114 and 115, was more closely associated with the original image than three of the four new 800 x 800 simulations.

The new velocity bunching coefficients producing images I and I2 were disappointing, resulting in the worst outcomes of the new simulation batch. Talking to the researchers at AssenSAR, this result was to be expected as the velocity bunching simulation is not complete model for the representation of SAR images of sea surface waves. This is a slight improvement in the spread of the bell like curve, the velocity bunching simulation creates a normal gaussian distribution, though this curve does not accurately reflect the real histogram data, showing an initial peak which tapers off to near zero at 0.3 on the normalised scale.

As all the images covered in this investigation display non-Gaussian distributions with most of the data positioning near the initial point of origin, 0 with the data peak generally before 0.1. Images with this data profile indicate mostly smooth water which displays as large black sections in the SAR image. The one case in the dataset where the peak of the data is beyond 0.1 is in the Gulf of Mexico SAR images, figures 57 and 59.

Both new S-based images, S and S2 have the peak portion of the data at roughly the same point, although the data peak in the S2 simulation is earlier than the peak in the real data. Accordingly, the S and S2 images were very dark, even though the data indicates more wave action than is represented, as maximum intensity in the normalised version goes up to 2.5 for S2 and 2 for S.

Of all four data sets, the S simulation represents the best fit in both its normalized and unnormalized versions, even showing a smaller Euclidean distance than the S0 simulation in the first test batch. As with the S0 simulation, the unnormalised version shows the best alignment between the simulation and the real image, with similar curves in the trailing data. There are slight statistical difference in values here, though these slight inaccuracies could come from errors introduced in the denoising process. The normalized version does have the closest distance between the two distributions of simulated and real histogram data, although the peaks of the simulated data, while near the same level of intensity as the original values, the PDF value is nearly double, trailing off quickly to zero earlier than the original.

From the analysis of the data above, with the consensus of the AssenSAR Research Group, the S distribution model was selected for the final round of simulations.

5. 3rd iteration simulations

The five images selected for the final simulation by AssenSAR are the Strait of Gibraltar subset 2, New Zealand subset 2, Barcelona dataset 1 subset 2, dataset 12 subset 1, and dataset 20 subset 1. Two simulations were conducted on each image with one using NRCS, labelled as **S**, and the iteration of the same method will be **S0**.

5.1. 3rd iteration simulations datasets

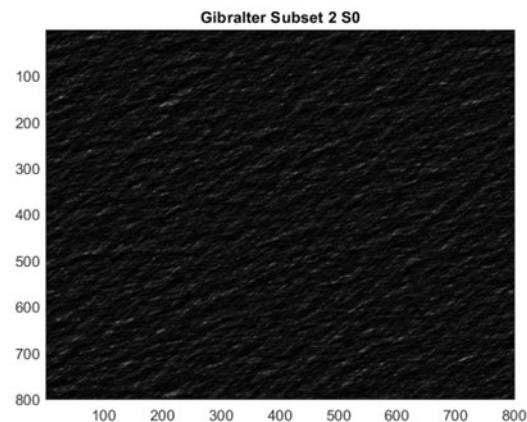
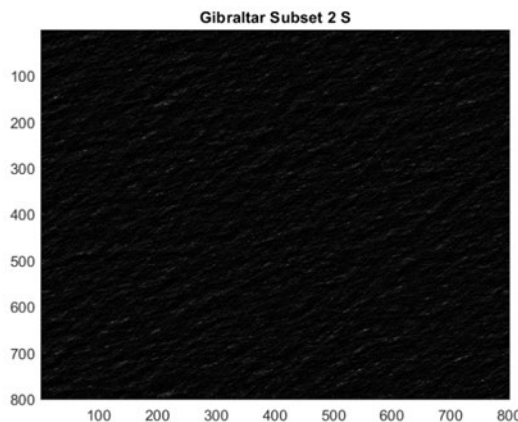


Fig. 134

Fig. 135

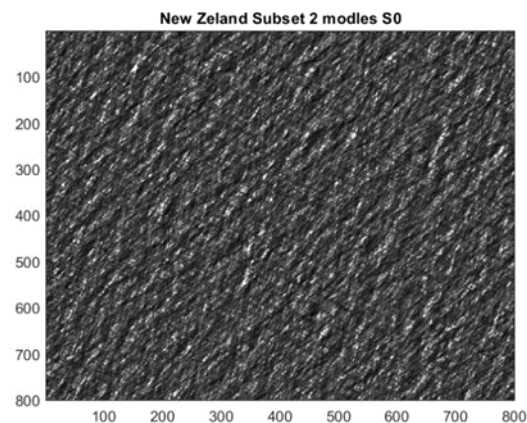
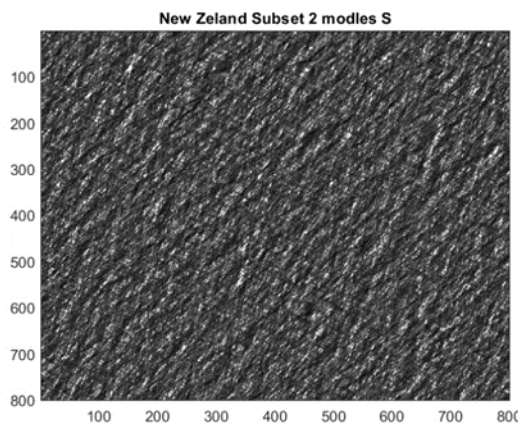


Fig. 136

Fig. 137

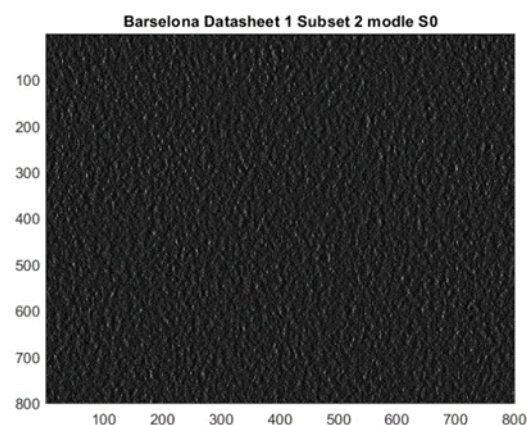
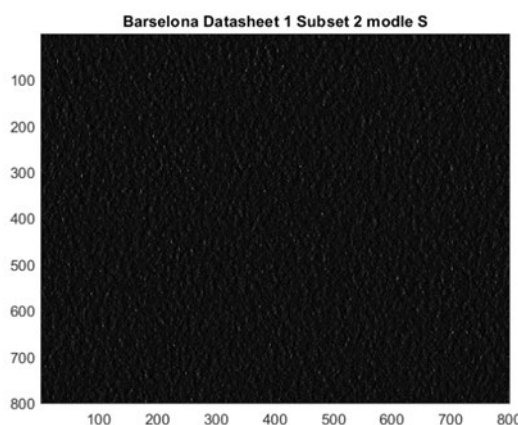


Fig. 138

Fig. 139

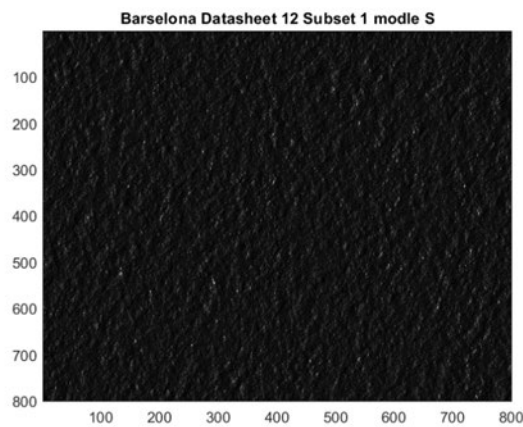


Fig. 140

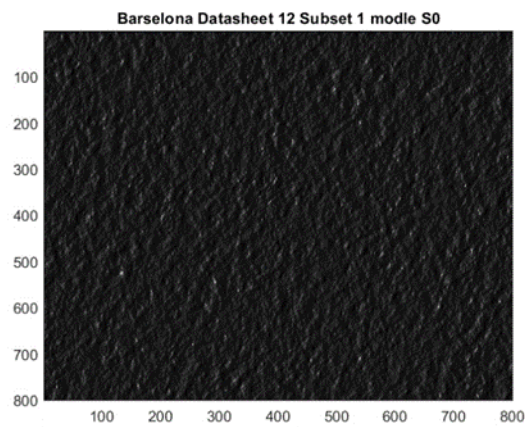


Fig. 141

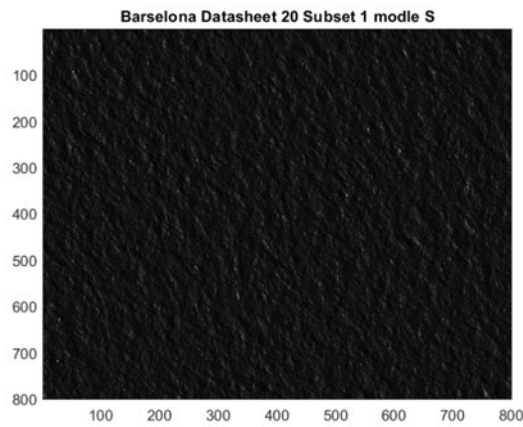


Fig. 142

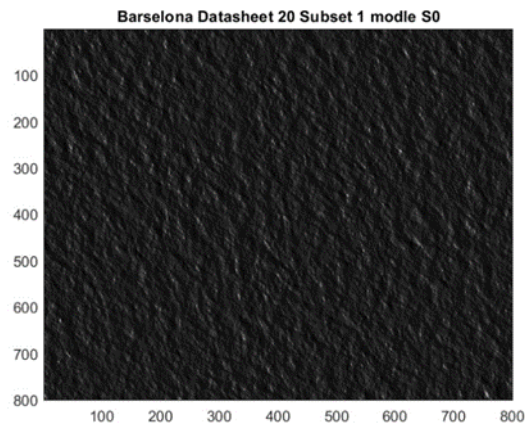


Fig. 143

5.2. 3rd iteration simulated image test results

5.2.1. Simulated S image –Strait of Gibraltar – subset 2

a) Unnormalised

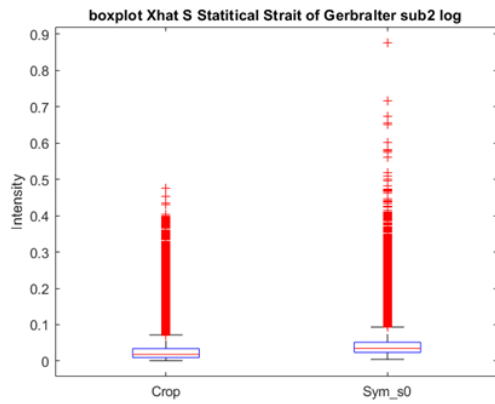


Fig. 144

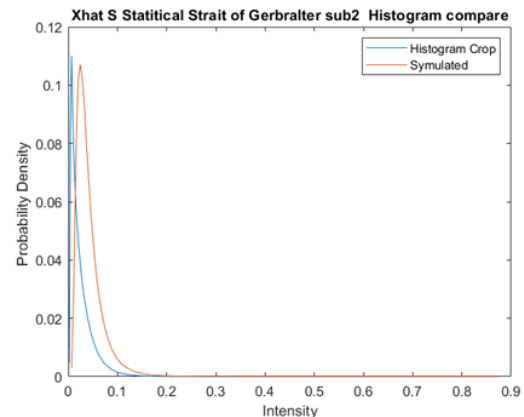


Fig. 145

b) Normalised

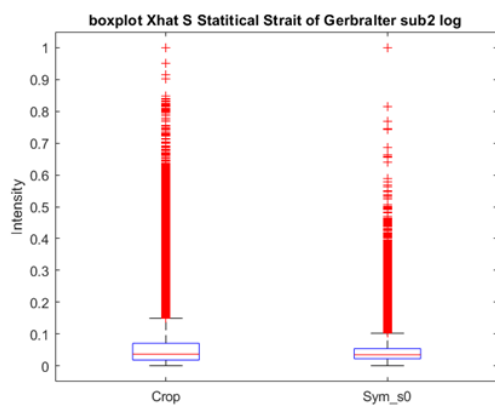


Fig. 146

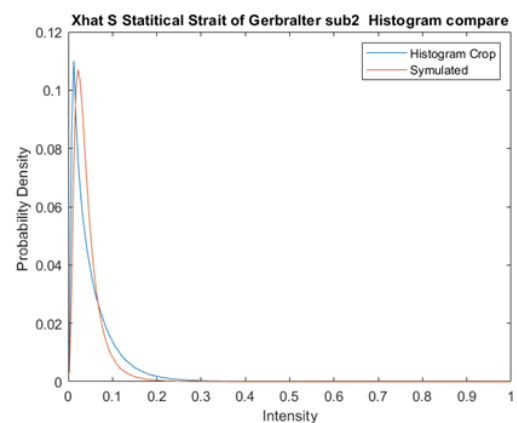


Fig. 147

Kullback–Leibler divergence	INF	Euclidean distance	0.099937
-----------------------------	-----	--------------------	----------

Table. 33 Simulated S divergence values - Strait of Gibraltar subset 2

5.2.2. Simulated S0 image –Strait of Gibraltar – subset 2

a) Unnormalised

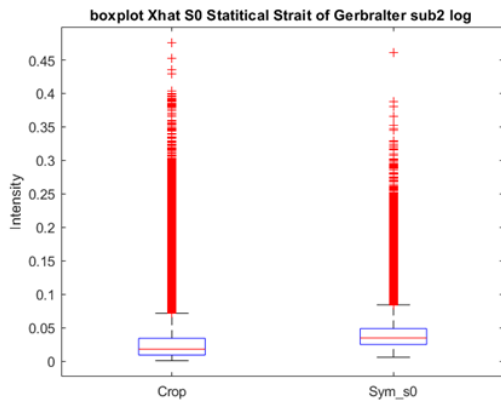


Fig. 148

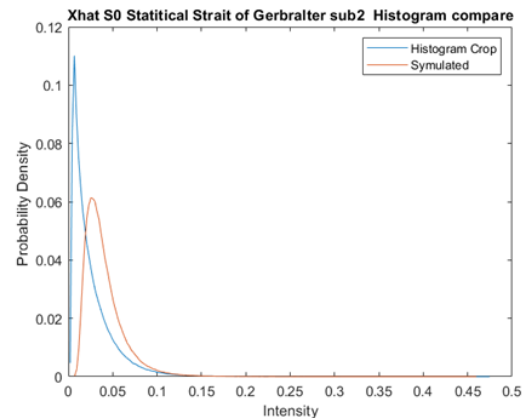


Fig. 149

b) Normalised

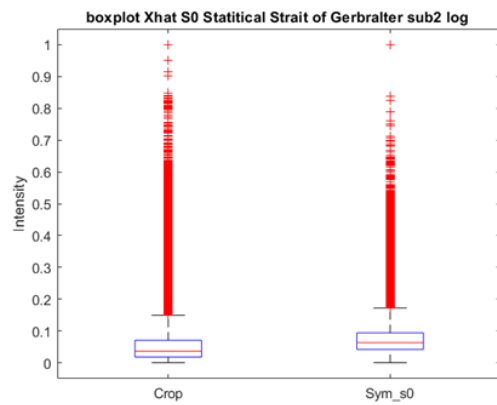


Fig. 150

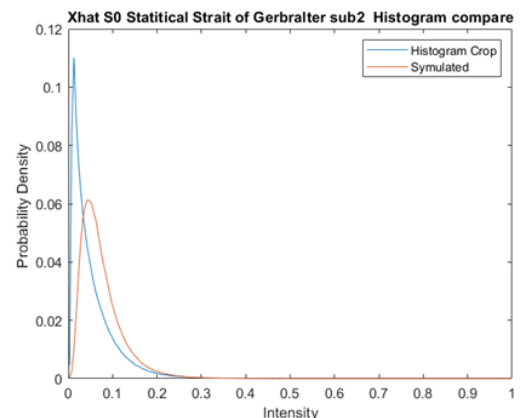


Fig. 151

Kullback–Leibler divergence	INF	Euclidean distance	0.16887
-----------------------------	-----	--------------------	---------

Table. 34 Simulated S0 divergence values Strait of Gibraltar subset 2

5.2.3. Simulated S image –New Zealand –subset 2

a) Unnormalised

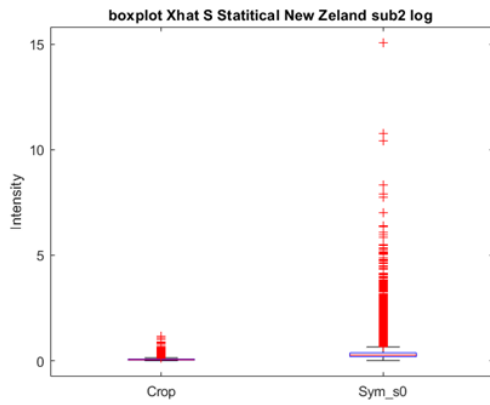


Fig. 152

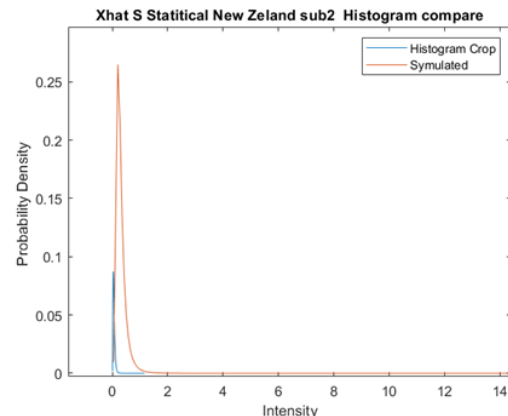


Fig. 153

b) Normalised

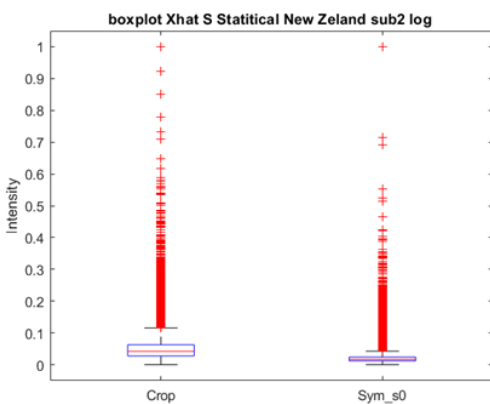


Fig. 154

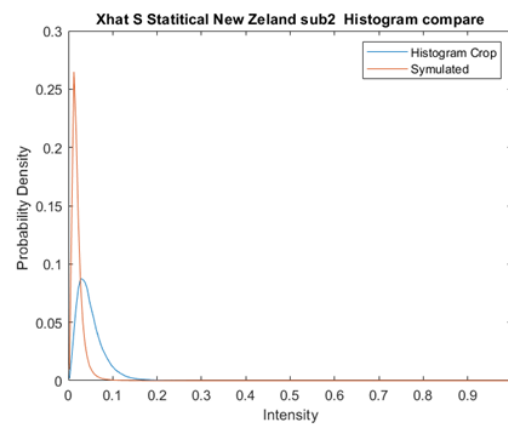


Fig. 155

Kullback–Leibler divergence	INF	Euclidean distance	0.33516
-----------------------------	-----	--------------------	---------

Table. 35 Simulated S divergence values New Zealand subset 2

5.2.4. Simulated S0 image –New Zealand – subset 2

a) Unnormalised

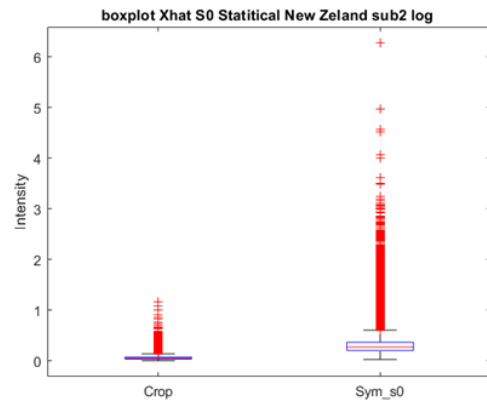


Fig. 156

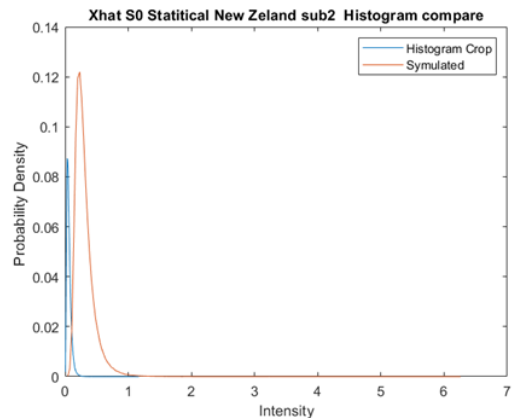


Fig. 157

b) Normalised

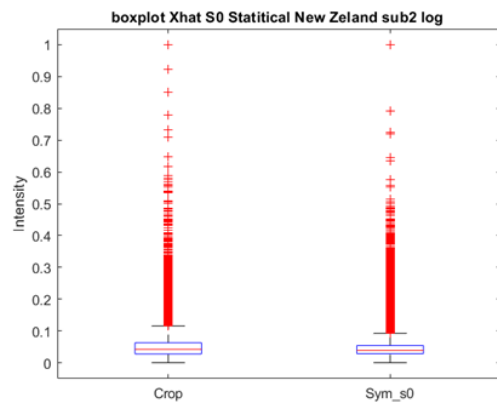


Fig. 158

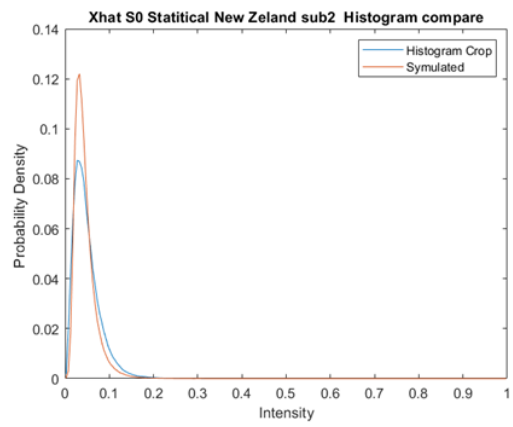


Fig. 159

Kullback–Leibler divergence	INF	Euclidean distance	0.071244
-----------------------------	-----	--------------------	----------

Table. 36 Simulated S0 divergence values New Zealand subset 2

5.2.5. Simulated S image – Barcelona – dataset 1 subset 2

a) Unnormalised

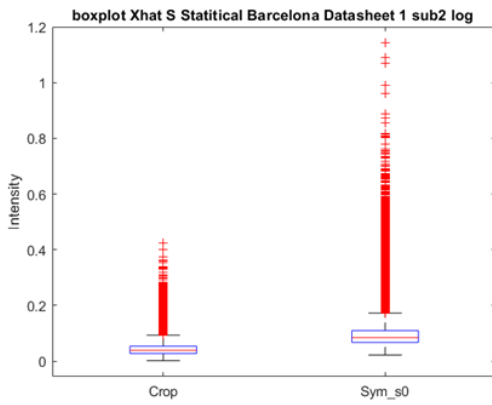


Fig. 160

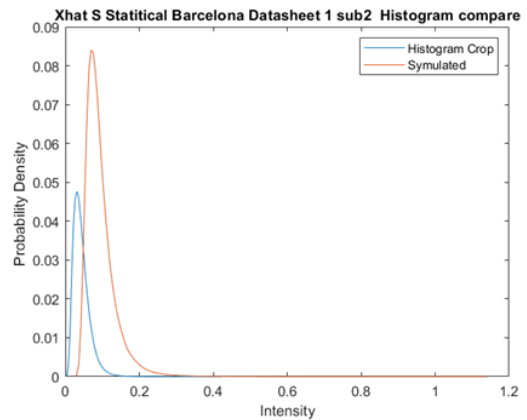


Fig. 161

b) Normalised

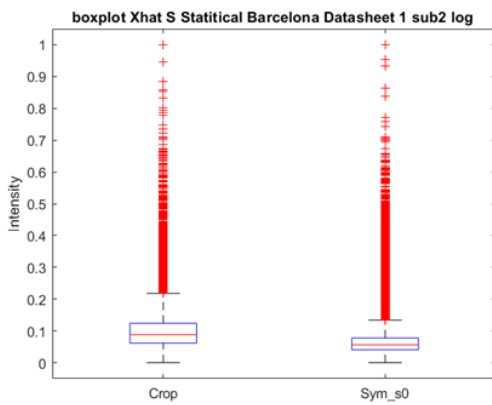


Fig. 162

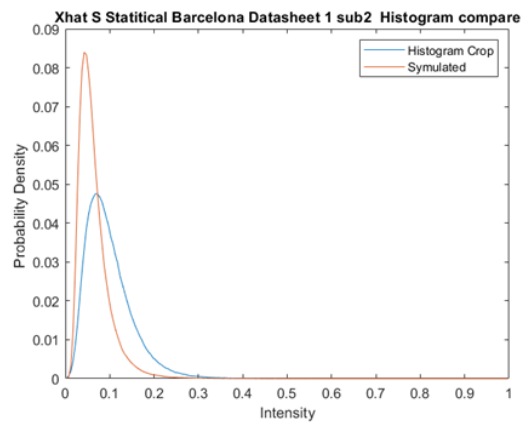


Fig. 163

Kullback–Leibler divergence	INF	Euclidean distance	0.13419
-----------------------------	-----	--------------------	---------

Table. 37 Simulated S divergence values Barcelona dataset 1 subset 2

5.2.6. Simulated S0 image – Barcelona – dataset 1 subset 2

a) Unnormalised

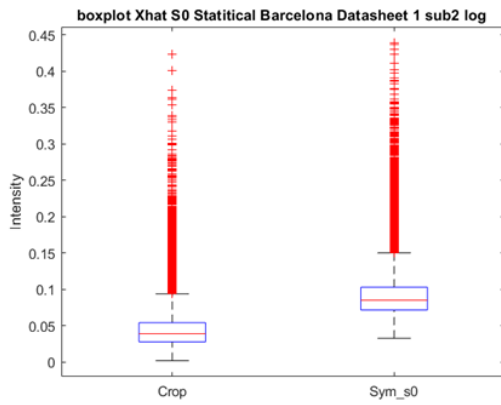


Fig. 164

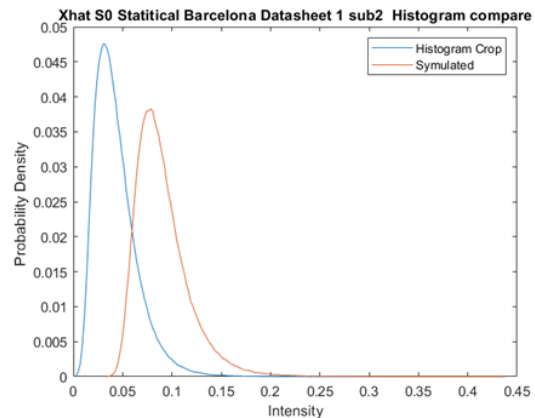


Fig. 165

b) Normalised

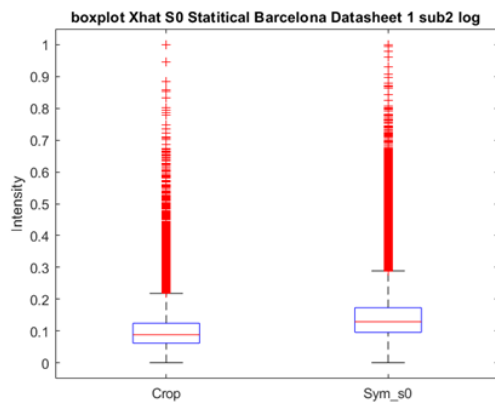


Fig. 166

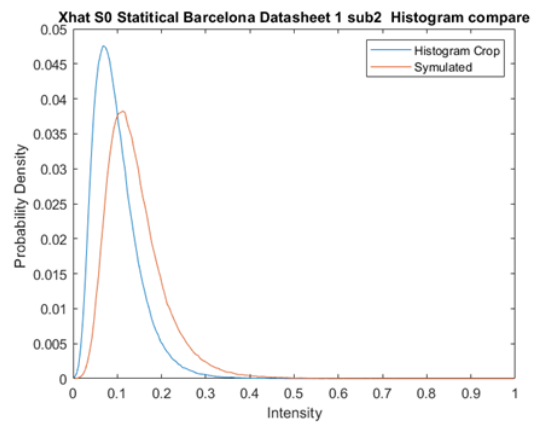


Fig. 167

Kullback–Leibler divergence	INF	Euclidean distance	0.099787
-----------------------------	-----	--------------------	----------

Table. 38 Simulated S0 divergence values Barcelona dataset 1 subset 2

5.2.7. Simulated S image – Barcelona – dataset 12 subset 1

a) Unnormalised

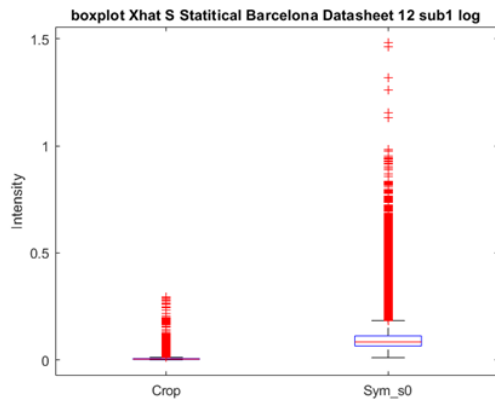


Fig. 168

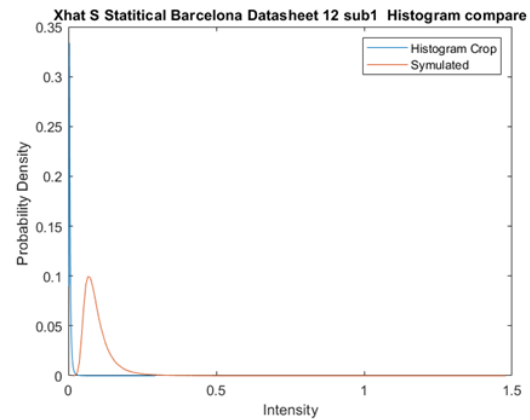


Fig. 169

b) Normalised

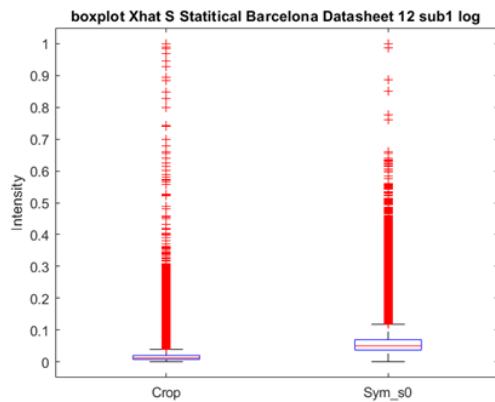


Fig. 170

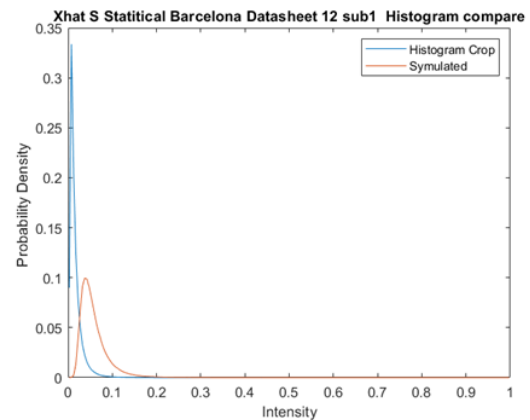


Fig. 171

Kullback–Leibler divergence	INF	Euclidean distance	0.46448
-----------------------------	-----	--------------------	---------

Table. 39 Simulated S divergence values Barcelona dataset 12 subset 1

5.2.8. Simulated S0 image – Barcelona – dataset 12 subset 1

a) Unnormalised

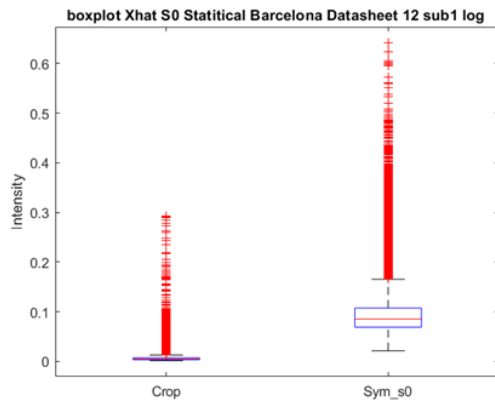


Fig. 172

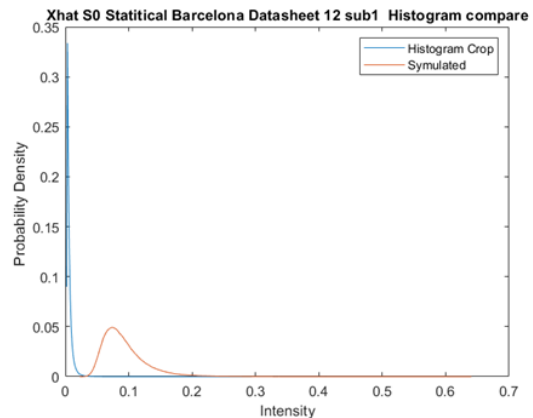


Fig. 173

b) Normalised

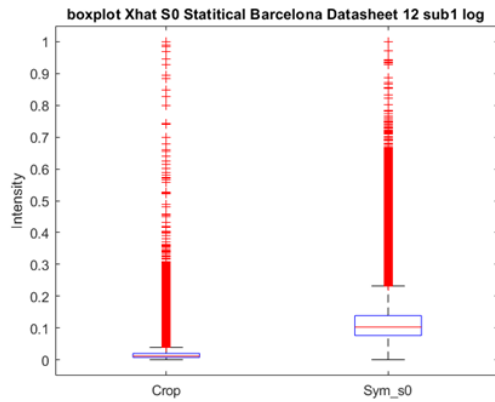


Fig. 174

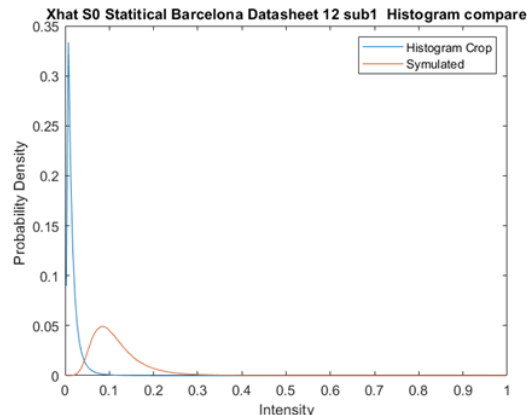


Fig. 175

Kullback–Leibler divergence	INF	Euclidean distance	0.46439
-----------------------------	-----	--------------------	---------

Table. 40 Simulated S0 divergence values Barcelona dataset 12 subset 1

5.2.9. Simulated S image – Barcelona – dataset 20 subset 1

a) Unnormalised

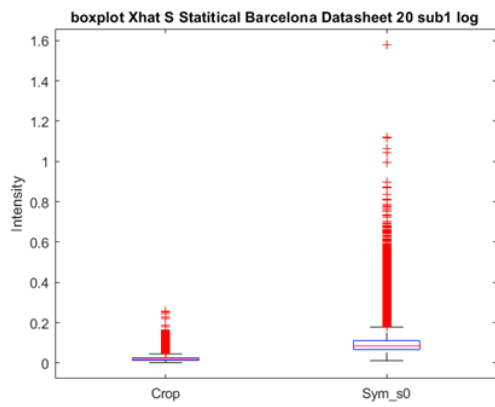


Fig. 176

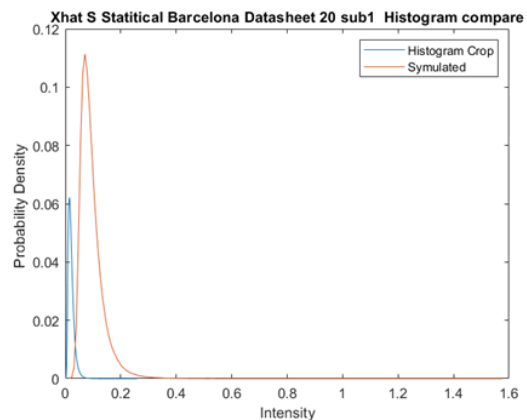


Fig. 177

b) Normalised

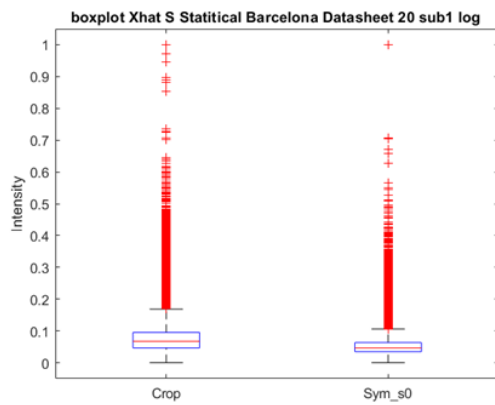


Fig. 178

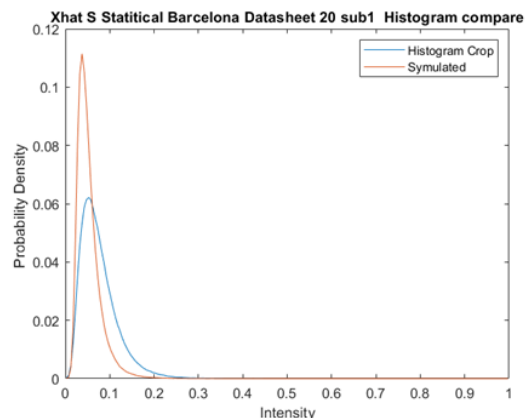


Fig. 179

Kullback–Leibler divergence	INF	Euclidean distance	0.13122
-----------------------------	-----	--------------------	---------

Table. 41 Simulated S divergence values Barcelona dataset 20 subset 1

5.2.10. Simulated S0 image – Barcelona – dataset 20 subset 1

a) Unnormalised

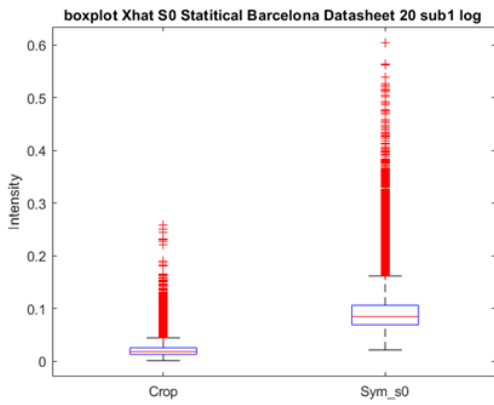


Fig. 180

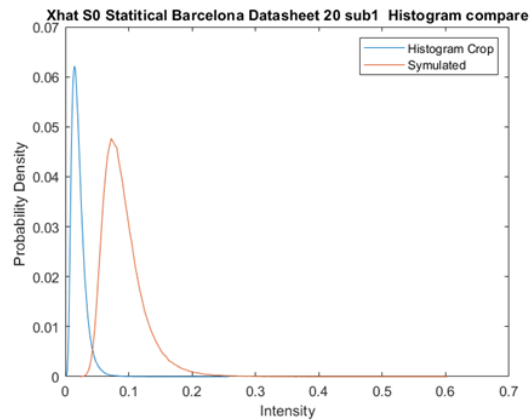


Fig. 181

b) Normalised

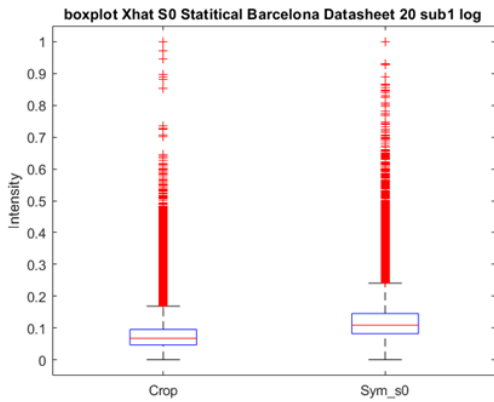


Fig. 182

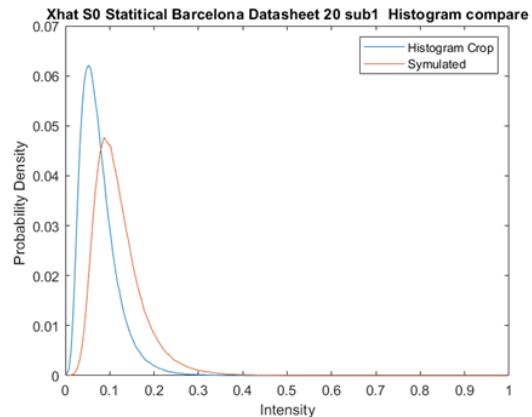


Fig. 183

Kullback–Leibler divergence	INF	Euclidean distance	0.14153
-----------------------------	-----	--------------------	---------

Table. 42 Simulated S0 divergence values Barcelona dataset 20 subset 1

5.3. Review of results of 3rd iteration simulated images

The results of the analysis of the third iteration of simulated images are contained in figures 144 to 183. These figures show both the box plot comparison to real histogram data, as well as the histogram comparison of normal data for two simulations, S and S0, presented as both unnormalised and normalised, for each of five real images from the original dataset.

Before reviewing the results, it is important to note an issue with the dataset which could potentially create errors. The Barcelona dataset, unlike the others, has oddly proportioned dimensions. The pixel resolution for the Barcelona datasets are ~ 0.91 meters by 1.89 meters. In contrast, all the other datasets are squares, with New Zealand being 3 meters by 3 meters and the Strait of Gibraltar being 1.25 meters by 1.25 meters. The odd size of the Barcelona dataset could make the images harder for the simulator to replicate. However, as availability of usable data is limited, the Barcelona datasets needed to be used in this investigation. Contributing to this issue was the fact that the images from the Gulf of Mexico dataset did not show sufficiently discernible wind generated sea waves to be useful in this investigation.

The third iteration of simulations began with the Strait of Gibraltar subset, which was the sole dataset used in the initial calibration of the simulator, see figures 102 to 117, along with the second iteration after certain refinements were made, see figures 118 to 133. When inspecting the differences between the latest two sets of simulated images, figures 144 to 151, and the first two iterations, there is a significant improvement in the closeness of accuracy of the histogram data, especially when looking at the normalized data of S in figure 147. When inspecting the box plot of S normalised, it has a statistically similar midpoint with a small margin of error to the real histogram data. When comparing S to S₀, the S simulation is closer in following both the histogram peak and its overall curve. Likewise, the Euclidean distance of S is less than that of S₀. S₀ is unable to achieve a similar peak to the histogram data in both in both normalised and unnormalised cases. It should be noted that the simulated images generate smoother curves as they follow mathematical formulae. As expected, the real images have more abrupt and stark changes, with more complexity in the curves which makes them difficult to accurately simulate. These simulated images of the Strait of Gibraltar set have shown a significant improvement from their earlier iterations, where the simulated data midpoints were often 0.2 value points away from the real data. With specific reference to the S normalised simulation, these differences may now be attributed to potential errors in the denoising process as opposed to simulation error.

New Zealand subset was chosen for the final simulations as it has recognisable wind generated sea waves therefore with easily extractable parameters for the simulator for wind direction and wind speed. These parameters can be derived from the spacing between waves and their direction relative to the geographical position. The results of the simulation for the New Zealand data set are displayed in figures 152 to 155. Unlike the simulation for the Strait of Gibraltar dataset where the S simulation proved the best, the S₀ version of the simulation provides the closest approximation of the real data from the New Zealand images. In the case of the S simulation, it seems that there was an error in the tuning of intensity resulting in a max intensity of 15 in the unnormalised results. As a result, the simulated data peak in the histogram in both the normalised and unnormalised cases is significantly higher than that of the original data. Even when normalised, the simulator data peaks earlier than the actual data with a PDF value above 0.25 relative to the actual value which was less than 0.1. When normalized the S₀ distribution follows the incline and decline of the histogram data extremely well as

well as the tail end of the data. While the S0 simulation peak is higher than the histogram data, both datasets are close and the midpoints of each datasets are nearly identical, as can be seen in the box plot of figure 158. The S0 simulated image for the New Zealand dataset, in terms of overall spread of the data, achieves a better accuracy than the simulated image for the Strait of Gibraltar this can as evidenced by Euclidean distance of 0.071244 versus 0.099937. The initial incline of the histogram curve and the intensity value of the peak for the S0 simulation for New Zealand is closer to the actual image data than it is for the S simulation for the Strait of Gibraltar. One likely reason for this improvement with the New Zealand data is the greater level of accuracy in identifying the wind speed and direction parameters from the images for New Zealand versus the Strait of Gibraltar. As such, the simulation is more accurate.

The original image from Barcelona dataset 1 subset 2, figure 25, has reasonably well-defined waves, increasing the potential that the simulation results will be accurate. The simulation for this dataset is presented in figures 160 to 167. As expected, the normalised versions the data achieved the best correlations. The S0 version of the simulated image provided the closest distribution to the histogram data, and though the curves had very similar gradients, the simulated curve was displaced to the right. This error may be related to the distortion of the image proportions discussed earlier. This data shift is present in all the attempted simulations of the Barcelona data. The Euclidean distance of 0.099787 is almost equivalent to that of the S simulation for the Strait of Gibraltar dataset, affirming that this S0 simulation is largely accurate.

For the Barcelona dataset 12 subset 1, the results of the simulation, figures 168 to 175, are very disappointing. This negative result was expected, however, as this is the one image where the K distribution was not the most appropriate, see table 14. The main issue with this image is its extreme darkness, which is observable in the nearly vertical histogram curve. With very little outlying data, this image is not well suited for simulation. Both the S and S0 simulations are incapable of achieving a close value, with Euclidean distances over 0.4 in contrast to the others above which were all less than 0.1.

The final image simulated was Barcelona dataset 20 subset 1, the results of which are presented in figures 176 to 183. The original image, figure 34, has some clearly defined wind generated sea waves, therefore it should be capable of simulation with minimal inaccuracy, other than potentially the image proportion issue. However, when inspecting the results, while better than the results of Barcelona dataset 12 subset 1, and reasonably close in approximation, this simulation was still the second worse of the batch. Between the two simulations, S normalised, figure 179, is more accurate than S0 normalised, figure 183, with the histogram peaks more closely aligned, the initial curves are similar though the simulation overshoots the PDF at the peak and trails to zero earlier than the histogram. Interestingly, figure 179 is the only simulation of all performed on the Barcelona datasets where the peak has shifted to the left instead of to the right. While the Euclidean distance of 0.13122 for S is respectable for a simulation, it is not nearly as good as the results below 0.1 for the Strait of Gibraltar and New Zealand datasets.

5.4. Items out of scope

There were potential extensions of this project that were excluded due to the official constraints on the length of this thesis. For example, work performed by the author to extract and model noise within each of the original SAR images has been delivered to the AssenSAR Research Group for further analysis. The current iteration of the AssenSAR simulator does not support the generation of noise in the simulated images. As such, this additional work was done to support future improvements to the simulator. A discussion of the results of this investigation of the noise within the original images would have required at least an additional 12 pages of text and figures. Additional work included a statistical distribution run against each of the simulated images. Other unsuccessful early tests were excluded from the discussion. If the reader desires more information on this additional work, links to all the files are accessible in Appendix 2. It should be noted that access to the simulator and the number of simulated images produced throughout this investigation was limited by COVID-19 restrictions.

6. Conclusion

The goal of this thesis was to investigate the statistical models which best represent wind generated sea waves within SAR images and to perform iterative testing with the AssenSAR Research Group to assess and improve the accuracy of their simulator's ability to generate realistic wave patterns. The AssenSAR simulator's ultimate goal is to be able to detect ship generated Kelvin wake patterns within SAR images but without an effective model of the wind generated sea waves and how these waves interact with ship wakes, the ship wake detection algorithms will not be statistically accurate.

From the initial investigation, K distribution was found to be the best statistical model for representing the peak portion of the data, up to the tail portion of the data. Beyond this point K distribution was prone to errors. Across the tail of the data, lognormal distribution consistently achieved the best results. These results suggest that a combination of the K and Lognormal distributions will achieve the best outcomes when generating simulations.

Over the course of this investigation, significant improvement was made through three iterations of simulations as lessons learned were applied and adjustments were made to parameters of the simulator. The data model that produced the best results consistently throughout the tests utilized Normalized Radar Cross Section (NRCS), which was clearly better than velocity bunching model. These improvements can easily be seen through the decrease in the values of Euclidean distance of the best case of each of the iterative steps. In the first round, simulate S0 image had a Euclidean distance of 0.2084, which was marginally reduced in the second iteration where the simulated S image achieved a Euclidean distance of 0.2018. The final round had the largest increase in performance as improvements made in both of the first two iterations had a cumulative effect, achieving a significant reduction to a Euclidean distance of 0.0712 in the S0 simulation of New Zealand subset 2.

Throughout these tests, it became clear that datasets with clearly discernible waves with clear difference in intensity values between peaks and troughs were important for modelling accuracy. Additionally, where accurate weather data with wind speed and direction is available, the results of the simulation will be improved. Where such data is not readily perceptible, the model is likely to present errors.

From the initial simulations through multiple iterations performed throughout this research the AssenSAR simulator is improving the quality of its results, producing simulations with increasing levels of accuracy. Though some further testing will be needed before the final release, the testing performed in support of this project has been useful in the further development of the software which is expected to be ready and available from the AssenSAR Research Group by 2022.

Appendix 1 - Bibliography

- [1] M. S. Moran, "Principles and Applications of Imaging Radar, Manual of Remote Sensing, 3rd Edition, Volume 2," *Eos, Transactions American Geophysical Union*, vol. 80, no. 6, 1999, doi: 10.1029/99eo00047.
- [2] R. Bamler, "Principles of synthetic aperture radar," *Surveys in Geophysics*, vol. 21, no. 2–3, 2000, doi: 10.1023/A:1006790026612.
- [3] J. R. Apel and F. I. Gonzalez, "Nonlinear features of internal waves off Baja California as observed from the Seasat imaging radar.,," *Journal of Geophysical Research*, vol. 88, no. C7, 1983, doi: 10.1029/JC088iC07p04459.
- [4] W. G. Rees, "Physical principles of remote sensing," *Physical principles of remote sensing*, 1990, doi: 10.1016/0031-9201(91)90165-e.
- [5] J. C. Curlander and R. N. McDonough, *Synthetic Aperture Radar: Systems & Signal Processing*. New York: John Wiley and Sons, 1991.
- [6] C. C. Wackerman, K. S. Friedman, W. G. Pichel, P. Clemente-Colon, and X. Li, "Automatic detection of ships in RADARSAT-1 SAR imagery," *Canadian Journal of Remote Sensing*, vol. 27, no. 5, 2001, doi: 10.1080/07038992.2001.10854896.
- [7] G. W. Stimson, *Introduction to Airborne Radar*. 1998.
- [8] ESA, "Earthdata Nasa information on SAR background," *ESA*, Mar. 10, 2021, [Online]. Available: <https://earthdata.nasa.gov/learn/backgrounder/what-is-sar>.
- [9] G. Zilman, A. Zapolski, and M. Marom, "On detectability of a ship's Kelvin wake in simulated SAR images of rough sea surface," *IEEE Transactions on Geoscience and Remote Sensing*, vol. 53, no. 2, 2015, doi: 10.1109/TGRS.2014.2326519.
- [10] O. Karakuş, I. Rizaev, and A. Achim, "Ship Wake Detection in SAR Images via Sparse Regularization," *IEEE Transactions on Geoscience and Remote Sensing*, vol. 58, no. 3, 2020, doi: 10.1109/TGRS.2019.2947360.
- [11] S. K. Chaturvedi, "Study of synthetic aperture radar and automatic identification system for ship target detection," *Journal of Ocean Engineering and Science*, vol. 4, no. 2, pp. 173–182, 2019, doi: <https://doi.org/10.1016/j.joes.2019.04.002>.

- [12] A. Moreira, P. Prats-Iraola, M. Younis, G. Krieger, I. Hajnsek, and K. P. Papathanassiou, "A tutorial on synthetic aperture radar," *IEEE Geoscience and Remote Sensing Magazine*, vol. 1, no. 1, pp. 6–43, 2013, doi: 10.1109/MGRS.2013.2248301.
- [13] S. Martin, *An introduction to ocean remote sensing*, vol. 9781107019386. 2013.
- [14] J. F. Lawless, "Inference in the generalized gamma and log gamma distributions," *Technometrics*, vol. 22, no. 3, 1980, doi: 10.1080/00401706.1980.10486173.
- [15] H. Pham and C. D. Lai, "On recent generalizations of the Weibull distribution," *IEEE Transactions on Reliability*, vol. 56, no. 3, 2007, doi: 10.1109/TR.2007.903352.
- [16] P. Beckmann, "Rayleigh distribution and its generalizations," *Journal of Research of the National Bureau of Standards, Section D: Radio Science*, vol. 68D, no. 9, 1964, doi: 10.6028/jres.068d.092.
- [17] M. M. Siddiqui, "Statistical inference for Rayleigh distributions," *Journal of Research of the National Bureau of Standards, Section D: Radio Science*, vol. 68D, no. 9, 1964, doi: 10.6028/jres.068d.100.
- [18] D. Blacknell, "Comparison of parameter estimators for k-distribution," *IEE Proceedings: Radar, Sonar and Navigation*, vol. 141, no. 1, 1994, doi: 10.1049/ip-rsn:19949885.
- [19] L. H. Ahrens, "The lognormal distribution of the elements (2)," *Geochimica et Cosmochimica Acta*, vol. 6, no. 2–3, 1954, doi: 10.1016/0016-7037(54)90021-6.
- [20] M. D. Yacoub, J. E. V. Bautista, and L. Guerra de Rezende Guedes, "On higher order statistics of the Nakagami-m distribution," *IEEE Transactions on Vehicular Technology*, vol. 48, no. 3, 1999, doi: 10.1109/25.764995.
- [21] I. R. Joughin, D. B. Percival, and D. P. Winebrenner, "Maximum Likelihood Estimation of K Distribution Parameters for SAR Data," *IEEE Transactions on Geoscience and Remote Sensing*, vol. 31, no. 5, 1993, doi: 10.1109/36.263769.
- [22] B. Liu and Y. He, "SAR Raw Data Simulation for Ocean Scenes Using Inverse Omega-K Algorithm," *IEEE Transactions on Geoscience and Remote Sensing*, vol. 54, no. 10, 2016, doi: 10.1109/TGRS.2016.2582525.
- [23] O. Karakuş, I. Rizaev, and A. Achim, "Ship Wake Detection in SAR Images via Sparse Regularization," *IEEE Transactions on Geoscience and Remote Sensing*, vol. 58, no. 3, 2020, doi: 10.1109/TGRS.2019.2947360.
- [24] O. Karakus, E. E. Kuruoglu, and A. Achim, "A Generalized Gaussian Extension to the Rician Distribution for SAR Image Modeling," *IEEE Transactions on Geoscience and Remote Sensing*, 2021, doi: 10.1109/TGRS.2021.3069091.

- [25] ESA, “SAR image Straits of Gibraltar, USA, ESA,” *Airbus*, Dec. 05, 2008, [Online]. Available: <https://www.intelligence-airbusds.com/en/9317-sample-imagery-detail?product=5297&keyword=&type=364>
- [26] ESA, “TerraSAR-X StripMap - USA MGD RE VV,” *Airbus*, Oct. 07, 2010. [Online]. Available: <https://www.intelligence-airbusds.com/en/9317-sample-imagery-detail?product=37985&keyword=&type=364>
- [27] ESA, “SAR image of Barcelona, Spain, ESA,” *Airbus*, Apr. 07, 2008, [Online]. Available: <https://www.intelligence-airbusds.com/en/9317-sample-imagery-detail?product=37962&keyword=&type=364>
- [28] ESA, “SAR image of Bay of Plenty, New Zealand, ESA,” *Airbus*, Dec. 10, 2011, [Online]. Available: <https://www.intelligence-airbusds.com/en/9317-sample-imagery-detail?product=37983&keyword=&type=364>
- [29] Brockmann Consult, SkyWatch, and C-5, “Sentinel Application Platform (SNAP) ToolBox” ESA, [Online]. Available: <http://step.esa.int/main/toolboxes/snap/>
- [30] P. Singh and R. Shree, “Analysis and effects of speckle noise in SAR images,” 2016, doi: 10.1109/ICACCAF.2016.7748978.
- [31] C. Deledalle, “MuLoG: MUlti-channel LOgarithm with Gaussian denoising,” Jan. 29, 2020, [Online]. Available: <https://www.charles-deledalle.fr/pages/mulog.php>
- [32] “Gaussian Noise or Gaussian Probability Distribution image,” sonic studio webdav, [Online]. Available: https://www.sfu.ca/sonic-studio-webdav/handbook/Gaussian_Noise.html
- [33] J. R. Hershey and P. A. Olsen, “Approximating the Kullback Leibler divergence between Gaussian mixture models,” in *ICASSP, IEEE International Conference on Acoustics, Speech and Signal Processing - Proceedings*, 2007, vol. 4, doi: 10.1109/ICASSP.2007.366913.
- [34] J. Goldberger, S. Gordon, and H. Greenspan, “An efficient image similarity measure based on approximations of KL-divergence between two Gaussian mixtures,” in *Proceedings of the IEEE International Conference on Computer Vision*, 2003, vol. 1, doi: 10.1109/iccv.2003.1238387.
- [35] L. Wang, Y. Zhang, and J. Feng, “On the Euclidean distance of images,” *IEEE Transactions on Pattern Analysis and Machine Intelligence*, vol. 27, no. 8, 2005, doi: 10.1109/TPAMI.2005.165.
- [36] H. Meng, X. Wang, J. Chong, X. Wei, and W. Kong, “Doppler spectrum-based NRCS estimation method for low-scattering areas in ocean SAR images,” *Remote Sensing*, vol. 9, no. 3, 2017, doi: 10.3390/rs9030219.

Samuel James Taylor

Statistical Modelling of Sea Surface Wind Generated Waves

[37] M. Marghany, "Velocity bunching model for modelling wave spectra along east coast of Malaysia," *Journal of the Indian Society of Remote Sensing*, vol. 32, no. 2, 2004, doi: 10.1007/BF03030875.

[38] E. Jakeman and P. N. Pusey, "Significance of K distributions in scattering experiments," *Physical Review Letters*, vol. 40, no. 9, 1978, doi: 10.1103/PhysRevLett.40.546.

Samuel James Taylor

Statistical Modelling of Sea Surface Wind Generated Waves

Appendix 2 - Access to files utilised

Follow link below to access all the files used within this research project. The workspace includes approximately 140 Gigabits of information, as raw SAR images have inherently large file sizes.

https://uob-my.sharepoint.com/:f/g/personal/st17078_bristol_ac_uk/EhSQV7NaM6JMrluzv1u1_QgBIXiD8BTBoE7vU4Yh06wpMw?e=YWP1sp

GitHub was considered but it was not workable due the large file sizes of the raw SAR images.

Appendix 3 - Programs utilised

Filename /Algorithm / Package	Supplier / Source / Author / Website	Use / Modifications made / Student written
Snap	ESA – European Space Agency https://step.esa.int/main/toolboxes/snap/	For the decoding of SAR images and the calibration of the images
MuLoG Denoiser specal_denoising_Term2_data.m	MATLAB Dr. Charles Deledalle https://www.charles-deledalle.fr/pages/mulog.php	The code was modified for the specific value of L in denoising and processing the whole denoised images in one step. Creates matrix data for each subset and a matrix data of the multiplicative noise
testing_L_values.m	MATLAB – Dr. Charles Deledalle https://www.charles-deledalle.fr/pages/mulog.php	Edited for the to test differing values for the denoiser.
KLDiv.m	MATLAB	Student written, Kullback-Leibler divergence formula
Statitical_USA_GoM_sub1.m	MATLAB	Student written, runs statistical models against labelled subset
pure_noise_Statitical_USA_GoM_sub1.m	MATLAB	Student written, runs statistical models against labelled subset's noise extracted from the denoiser
Statitical_USA_GoM_sub2.m	MATLAB	Student written, runs statistical models against labelled subset
pure_noise_Statitical_USA_GoM_sub2.m	MATLAB	Student written, runs statistical models against labelled subset's noise extracted from the denoiser
Statitical_NewZeland_sub1.m	MATLAB	Student written, runs statistical models against labelled subset
pure_noise_Statitical_NewZeland_sub1.m	MATLAB	Student written, runs statistical models against labelled subset's noise extracted from the denoiser
Statitical_NewZeland_sub2.m	MATLAB	Student written, runs statistical models against labelled subset
pure_noise_Statitical_NewZeland_sub2.m	MATLAB	Student written, runs statistical models against labelled subset's noise extracted from the denoiser
Statitical_Strait_of_Gibralter_sub1.m	MATLAB	Student written, runs statistical models against labelled subset
pure_noise_Statitical_Strait_of_Gibralter_sub1.m	MATLAB	Student written, runs statistical models against labelled subset's noise extracted from the denoiser

Statistical_Strait_of_Gibralter_sub2.m	MATLAB	Student written, runs statistical models against labelled subset
pure_noise_Statitical_Strait_of_Gibralter_sub2.m	MATLAB	Student written, runs statistical models against labelled subset's noise extracted from the denoiser
Statitical_Barsilona_Datasheet1s ub1.m	MATLAB	Student written, runs statistical models against labelled subset
pure_noise_Statitical_Barsilona_Datasheet1_sub1.m	MATLAB	Student written, runs statistical models against labelled subset's noise extracted from the denoiser
Statitical_Barsilona_Datasheet1s ub2.m	MATLAB	Student written, runs statistical models against labelled subset
pure_noise_Statitical_Barsilona_Datasheet1_sub2.m	MATLAB	Student written, runs statistical models against labelled subset's noise extracted from the denoiser
Statitical_Barsilona_Datasheet5s ub1.m	MATLAB	Student written, runs statistical models against labelled subset
pure_noise_Statitical_Barsilona_Datasheet5_sub1.m	MATLAB	Student written, runs statistical models against labelled subset's noise extracted from the denoiser
Statitical_Barsilona_Datasheet5s ub2.m	MATLAB	Student written, runs statistical models against labelled subset
pure_noise_Statitical_Barsilona_Datasheet5_sub2.m	MATLAB	Student written, runs statistical models against labelled subset's noise extracted from the denoiser
Statitical_Barsilona_Datasheet8s ub1.m	MATLAB	Student written, runs statistical models against labelled subset
pure_noise_Statitical_Barsilona_Datasheet8_sub1.m	MATLAB	Student written, runs statistical models against labelled subset's noise extracted from the denoiser
Statitical_Barsilona_Datasheet8s ub2.m	MATLAB	Student written, runs statistical models against labelled subset
pure_noise_Statitical_Barsilona_Datasheet8_sub2.m	MATLAB	Student written, runs statistical models against labelled subset's noise extracted from the denoiser
Statitical_Barsilona_Datasheet12s ub1.m	MATLAB	Student written, runs statistical models against labelled subset
pure_noise_Statitical_Barsilona_Datasheet12_sub1.m	MATLAB	Student written, runs statistical models against labelled subset's noise extracted from the denoiser
Statitical_Barsilona_Datasheet12s ub2.m	MATLAB	Student written, runs statistical models against labelled subset
pure_noise_Statitical_Barsilona_Datasheet12_sub2.m	MATLAB	Student written, runs statistical models against labelled subset's noise extracted from the denoiser

Statitical_Barsilona_Datasheet17_sub1.m	MATLAB	Student written, runs statistical models against labelled subset
pure_noise_Statitical_Barsilona_Datasheet17_sub1.m	MATLAB	Student written, runs statistical models against labelled subset's noise extracted from the denoiser
Statitical_Barsilona_Datasheet17_sub2.m	MATLAB	Student written, runs statistical models against labelled subset
pure_noise_Statitical_Barsilona_Datasheet17_sub2.m	MATLAB	Student written, runs statistical models against labelled subset's noise extracted from the denoiser
Statitical_Barsilona_Datasheet20_sub1.m	MATLAB	Student written, runs statistical models against labelled subset
pure_noise_Statitical_Barsilona_Datasheet20_sub1.m	MATLAB	Student written, runs statistical models against labelled subset's noise extracted from the denoiser
Statitical_Barsilona_Datasheet20_sub2.m	MATLAB	Student written, runs statistical models against labelled subset
pure_noise_Statitical_Barsilona_Datasheet20_sub2.m	MATLAB	Student written, runs statistical models against labelled subset's noise extracted from the denoiser
Statitical_Barsilona_Datasheet21_sub1.m	MATLAB	Student written, runs statistical models against labelled subset
pure_noise_Statitical_Barsilona_Datasheet21_sub1.m	MATLAB	Student written, runs statistical models against labelled subset's noise extracted from the denoiser
Statitical_Barsilona_Datasheet21_sub2.m	MATLAB	Student written, runs statistical models against labelled subset
pure_noise_Statitical_Barsilona_Datasheet21_sub2.m	MATLAB	Student written, runs statistical models against labelled subset's noise extracted from the denoiser
Statitical_Barsilona_Datasheet24_sub1.m	MATLAB	Student written, runs statistical models against labelled subset
pure_noise_Statitical_Barsilona_Datasheet24_sub1.m	MATLAB	Student written, runs statistical models against labelled subset's noise extracted from the denoiser
Statitical_Barsilona_Datasheet24_sub2.m	MATLAB	Student written, runs statistical models against labelled subset
pure_noise_Statitical_Barsilona_Datasheet24_sub2.m	MATLAB	Student written, runs statistical models against labelled subset's noise extracted from the denoiser
I_Symulated_Statitical_Strait_of_Gibraltar_sub2.m	MATLAB	Student written, Simulator image compared to strait of Gibraltar subset 2 400 x 400 for simulated image in the X_... section of the function

S_Symulated_Statistical_Strait_of_Gibralter_sub2.m	MATLAB	Student written, Simulator image compared to strait of Gibraltar subset 2 400 x 400 for simulated image in the X_... section of the function
S0_Symulated_Statistical_Strait_of_Gibralter_sub2.m	MATLAB	Student written, Simulator image compared to strait of Gibraltar subset 2 400 x 400 for simulated image in the X_... section of the function
SR_Symulated_Statistical_Strait_of_Gibralter_sub2.m	MATLAB	Student written, Simulator image compared to strait of Gibraltar subset 2 400 x 400 for simulated image in the X_... section of the function
I_Symulated_Statistical_Strait_of_Gibralter_sub2.m	MATLAB	Student written, Simulator image compared to strait of Gibraltar subset 2 800 x 800 for simulated image in the X_... section of the function second Iteration
I2_Symulated_Statistical_Strait_of_Gibralter_sub2.m	MATLAB	Student written, Simulator image compared to strait of Gibraltar subset 2 800 x 800 for simulated image in the X_... section of the function second Iteration
S_Symulated_Statistical_Strait_of_Gibralter_sub2.m	MATLAB	Student written, Simulator image compared to strait of Gibraltar subset 2 800 x 800 for simulated image in the X_... section of the function second Iteration
S2_Symulated_Statistical_Strait_of_Gibralter_sub2	MATLAB	Student written, Simulator image compared to strait of Gibraltar subset 2 800 x 800 for simulated image in the X_... section of the function second Iteration
S_Symulated_Statistical_NewZeland_sub2.m	MATLAB	Student written, Final Simulated Image comparison 800 x 800 X_... comparing to New Zealand final simulation
S0_Symulated_Statistical_NewZeland_sub2.m	MATLAB	Student written, Final Simulated Image comparison 800 x 800 X_... comparing to New Zealand final simulation
S_Symulated_Statistical_Strait_of_Gibralter_sub2.m	MATLAB	Student written, Final Simulated Image comparison 800 x 800 X_... comparing to Strait of Gibraltar final simulation
S0_Symulated_Statistical_Strait_of_Gibralter_sub2.m	MATLAB	Student written, Final Simulated Image comparison 800 x 800 X_... comparing to Strait of Gibraltar final simulation
S_Symulated_Statistical_Barcelona_data1_sub2.m	MATLAB	Student written, Final Simulated Image comparison 800 x 800 X_... comparing to Dataset 1 subset 2 final simulation

S0_Symulated_Statitical_Barcelon a_data1_sub2.m	MATLAB	Student written, Final Simulated Image comparison 800 x 800 X... comparing to Dataset 1 subset 2 final simulation
S_Symulated_Statitical_Barcelona _data12_sub1.m	MATLAB	Student written, Final Simulated Image comparison 800 x 800 X... comparing to Dataset 12 subset 1 final simulation
S0_Symulated_Statitical_Barcelon a_data12_sub1.m	MATLAB	Student written, Final Simulated Image comparison 800 x 800 X... comparing to Dataset 12 subset 1 final simulation
S_Symulated_Statitical_Barcelona _data20_sub1.m	MATLAB	Student written, Final Simulated Image comparison 800 x 800 X... comparing to Dataset 20 subset 1 final simulation
S0_Symulated_Statitical_Barcelon a_data20_sub1.m	MATLAB	Student written, Final Simulated Image comparison 800 x 800 X... comparing to Dataset 20 subset 1 final simulation